공학박사학위논문

Feasibility Study on the Use of Gold Nanoparticles as a Dose Enhancement Agent for a Superficial X-ray Therapy Applied to Melanoma

흑색종의 표재 엑스선 치료 시 방사선 선량 증가제로서 금 나노입자 활용의 타당성 연구

2014년 8월

서울대학교 대학원

에너지시스템공학부

김 소 라

Feasibility Study on the Use of Gold Nanoparticles as a Dose Enhancement Agent for a Superficial X-ray Therapy Applied to Melanoma

지도 교수 김 은 희

이 논문을 공학박사 학위논문으로 제출함

2014년 4월

서울대학교 대학원

에너지시스템공학부

김 소 라

김소라의 박사학위 논문을 인준함

2014년 6월

위 원 장 김 곤 호 (인)

부위원장 김 은 희 (인)

위 원 이 재 기 (인)

위 원 심 형 진 (인)

위 원 배 상 우 (인)

ABSTRACT

Feasibility Study on the Use of Gold Nanoparticles as a Dose Enhancement Agent for a Superficial X-ray Therapy Applied to Melanoma

Kim, So Ra

Department of Nuclear Engineering

Seoul National University

The aim of radiation therapy is to kill tumor cells using ionizing radiation while sparing surrounding normal tissues. Recent advances in radiation therapy have resulted in the development of intensity modulated radiation therapy (IMRT) that allows the dose to conform more precisely to the three-dimensional shape of the tumor. However, the equipment-based beam delivery methods have a limitation of providing a curative radiation dose to the tumor volume without exceeding normal tissue tolerance because of the similar x-ray absorption characteristics of tumors and surrounding normal tissues. By loading high atomic number nanoparticles on tumor volume, it is possible to

deliver high radiation doses to tumor volume while sparing normal tissues in kilovoltage x-ray beams. The concept of using high atomic number nanoparticles as a dose enhancement agent is premised on the high photoelectric mass absorption coefficient of high atomic number materials in kilovoltage photon energy region, compared with soft tissues. Gold nanoparticles (AuNPs) have been of particular interest to researchers in recent years because of its high photoelectric mass absorption coefficient and biocompatibility.

The number of skin cancer patients has been increasing every year. AuNPs are expected to contribute to improving the efficiency of skin cancer radiation therapy as a dose enhancement agent. Prior to application of AuNPs as a dose enhancement agent in therapeutic purpose, more biological observations are required to clarify the physical predictions of the dose enhancement effect and to entirely understand the radiobiological responses of AuNPs. The ultimate goal of the present *in vitro* study was to investigate the potential of AuNPs as a dose enhancement agent in x-ray radiation therapy for skin cancer, especially melanoma.

Three types of cell lines, skin melanoma cells, gliosarcoma cells and normal dermal fibroblast cells, and two different sizes of the spherical AuNPs, 1.9 and 50 nm in diameter, were used in this study. Cells were irradiated at room temperature in the hard x-ray beam irradiation facility (YXLON model 450-D08) at Seoul National University, with 150 kVp (superficial) and 450

kVp (orthovoltage) x-rays. The clonogenic survival assay was conducted to investigate the dose enhancement effect as functions of AuNP size and concentration, photon energy, and cell-type. Also, the cytotoxicity assay, the observation of cellular localized AuNPs, the DNA double strand break (DSB) analysis, and the cell cycle analysis were performed to support the main results. MCNP-5 (Monte Carlo N-particle-5) calculations were performed to obtain the depth dose curves and the x-ray energy spectra in depth from the skin surface.

From the experiment, it was confirmed that the optimal combinations of AuNP size, concentration, and x-ray energy resulted in cells having high-linear energy transfer (LET) - like survival curve, leading to enhancing the cell radiosensitivity. The dose enhancement effect was also strongly dependent on cell-type and it was supposed to be partly contributed by the different efficiency of cellular uptake following cell type. AuNPs gave a significant dose enhancement effect on melanoma cells, which are well known as the most radioresistant cells in all types of skin cancers. The maximum dose enhancement factor was 2.29 for skin melanoma cells at 320 μM of 50 nm AuNPs with 150 kVp x-ray beams. To confirm the effect of those conditions on normal skin cells, the experiments were carried out on dermal fibroblast cells. 50 nm AuNPs had no remarkable toxicity on dermal fibroblast cells and provided lower dose enhancement effect to dermal fibroblast cells than skin melanoma cells. However, dose enhancement effect

on dermal fibroblast cells should not be overlooked and this result emphasizes the importance of the accurate AuNP delivery to melanoma.

By applying AuNPs to conventional fractionated radiation therapy of skin cancer, the major concerns of fractionation regimens are expected to be overcome. Although relatively high doses are deposited to tumor by applying AuNPs, the normal tissue damage would not be more significantly severe because radiation doses delivered from the equipment do not increase. Also by shortening the overall treatment time, AuNPs can contribute to resolving concern about tumor cell repopulation, which is a main cause of lowering the efficacy of the fractionated radiation therapy. In conclusion, the application of 50 nm AuNPs as a dose enhancement agent in superficial x-ray therapy could be a promising treatment method for T1 to T3 stages of melanoma. 50 nm AuNPs are preferably accumulated in melanoma by passive action. Modification of 50 nm AuNP with melanoma specific ligand would even further enhance the therapeutic effect.

Keywords: gold nanoparticle, AuNP, high atomic number nanoparticle, dose enhancement agent, superficial x-ray therapy, skin cancer, melanoma

Student Number: 2010-30253

CONTENTS

LIST OF TABLES

LIST OF FIGURES

CHAPTER 1

INTRODUCTION

The aim of radiation therapy is to kill tumor cells using ionizing radiation while sparing surrounding normal tissues. Recent advances in radiation therapy have resulted in the development of intensity modulated radiation therapy (IMRT) that is a type of three-dimensional conformal radiotherapy (3D-CRT) [1]. IMRT allows the dose to conform more precisely to the three-dimensional shape of the tumor by modulating the intensity of the radiation beam [2]. IMRT can deliver higher radiation doses to tumor volume while minimizing the dose to surrounding normal tissues. However, the equipment-based solution has a limitation of delivering a curative radiation dose to the tumor volume without exceeding normal tissue tolerance because of the similar x-ray absorption characteristics of tumors and surrounding normal tissues [3, 4]. While the equipment-based beam delivery methods are being continuously developed to better concentrate the dose within the shape of tumor volumes, alternate methods for improving the discrimination between tumors and surrounding normal tissues are also being investigated [3-5]. One of the alternate methods is the use of high atomic nanoparticles as a dose enhancement agent.

By loading high atomic number nanoparticles on tumor volume, it is possible to deliver high radiation doses to tumor volume while sparing normal tissues in kilovoltage x-ray beams. The concept of using high atomic number

nanoparticles as a dose enhancement agent is premised on the high photoelectric mass absorption coefficient of high atomic number materials in kilovoltage photon energy region, compared with soft tissues. Gold nanoparticles (AuNPs) have been of particular interest to researchers in recent years because of its high photoelectric mass absorption coefficient and biocompatibility [3].

Most cancer patients are treated with megavoltage photon produced by a clinical linear accelerator, while some cancer patients are treated with brachytherapy, and superficial (or orthovoltage) x-ray therapy [6]. The concept of using AuNPs as a dose enhancement agent is considered to be effective in treating superficial tumors, such as skin cancers, while not being suitable for external megavoltage x-ray therapy. The number of skin cancer patients has been increasing every year. AuNPs are expected to contribute to improving the efficiency of skin cancer radiation therapy as a dose enhancement agent. Prior to application of AuNPs as a dose enhancement agent in therapeutic purpose, more biological (*in vitro* and *in vivo*) observations are required to clarify the physical predictions of the dose enhancement effect and to entirely understand the radiobiological responses of AuNPs.

The ultimate goal of the present *in vitro* study was to investigate the potential of AuNPs as a dose enhancement agent in x-ray radiation therapy for skin cancers. The theoretical background and the previous researches have been reviewed first and the *in vitro* experiments have been performed as main works of the study.

CHAPTER 2

THEORETICAL BACKGROUND AND PREVIOUS RESEARCHES

2.1 The interaction of photons with high atomic number materials

The basic physics of the interaction of photons with high atomic number materials are presented in this chapter.

2.1.1 The interaction of photons with matter [5, 7-10]

Attenuation of photons by an absorbing material is caused by five types of interactions as represented in Figure 2.1. Photodisintegration can occur only at very high photon energies (>10 MeV) between a photon and an atomic nucleus. In the coherent scattering, a photon possesses its initial energy after interaction with absorber atoms and the only effect is the scattering of the photon at small angles. Therefore, only three major types of interactions play an important role in the field of radiation biology: the photoelectric absorption, the Compton scattering, and the pair production. Figure 2.2 illustrates the relative importance of the three major types of the photon interaction. Photon energy transfers to electron partially or entirely by these processes.

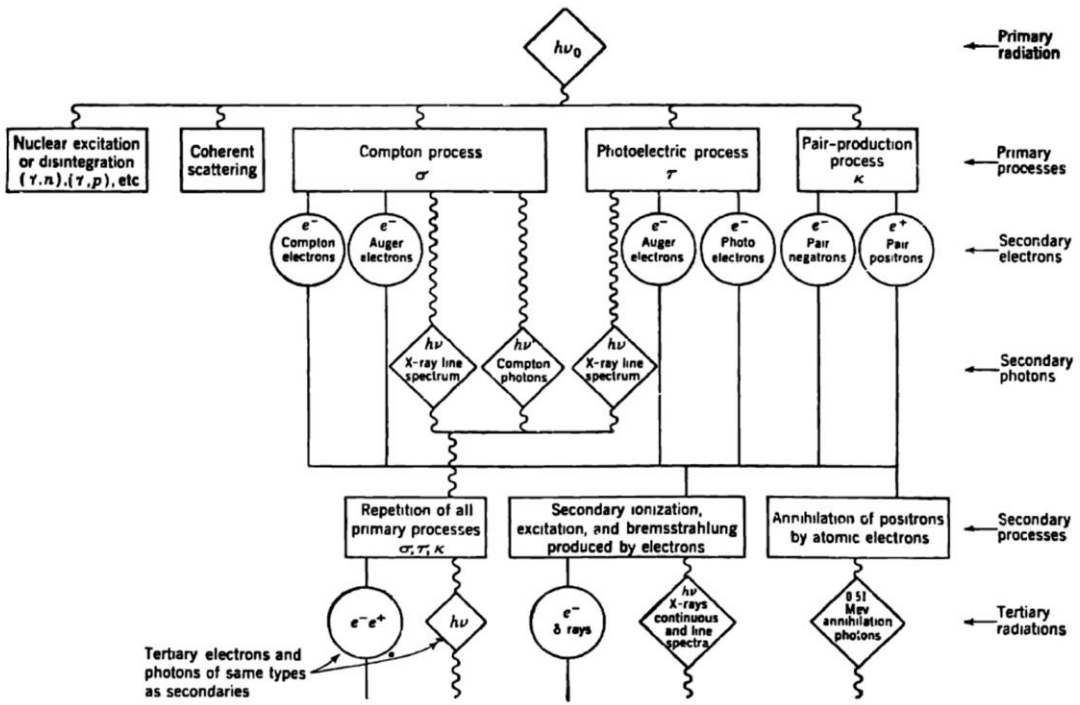

Figure 2.1. The diagram of the interaction of photons with an absorbing material. The types of interactions are in rectangles, photons of the various sorts are in diamonds, and electron radiations are in circles [10].

In the photoelectric absorption, an incident photon is completely absorbed in an absorber atom and a photoelectron is ejected from one of the bound shells. As a result of the emission of a photoelectron, the vacancy is generated in the bound shell and filled by the electron rearrangement from other shells of the atom or the capture of a free electron. In this process, the remainder of energy from filling the inner shell vacancy is liberated in the forms of characteristic x-rays or Auger electrons. This process can take place with the whole atom, not with a free electron. The probability of the photoelectric interaction severely depends on the atomic number of the absorbing material, because the whole atom participates in the process. The photoelectric interaction also depends on the incident photon energy. There is no single expression for the photoelectric attenuation coefficient (τ) over all ranges of the incident photon energy ($h\nu$) and the atomic number (Z) of an absorbing material. A rough but useful approximation is given by:

$$\tau \cong \text{constant} \times \frac{Z^n}{h\nu^{3.5}} \tag{2.1}$$

where the exponent n varies for the range of the incident photon energy [8]. The exponent n is about 4 at $h\nu$ = 0.1 MeV, and 4.0 to 4.6 as $h\nu$ increases from 0.1 to 3 MeV [10].

In the Compton scattering, the photon interacts with a free electron in an absorbing material. The free electron means that the binding energy of the electron is much less than the energy of the incident photon. The photon transfers a portion of its energy to the electron and is scattered with reduced

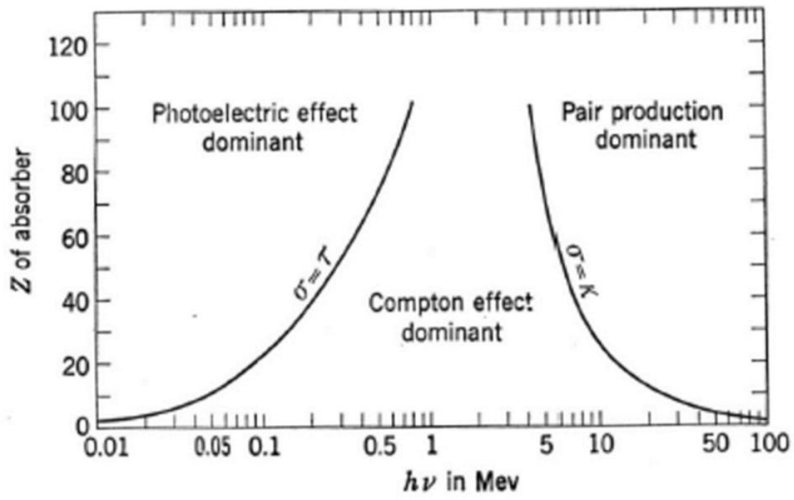

Figure 2.2. The relative importance of the three major types of the photon interaction. The lines show the values of Z and $h\nu$ for which the two neighboring effects are just equal [8].

energy. The energy of the incident photon needs to be large enough compared to the binding energy of the electron, because the Compton scattering is the interaction of an incident photon and a free electron. The photoelectric absorption becomes most probable when the incident photon energy is equal to or slightly higher than the electron binding energy. Therefore, as the photon energy increases above the binding energy of K-shell electron, the photoelectric effect decreases rapidly with energy and the Compton scattering becomes more important. However, the probability of the Compton scattering gradually decreases with increasing photon energy. The Compton scattering is independent of the atomic number of the absorbing material because the Compton scattering is occurred with free electrons in the absorbing material. The probability of the Compton scattering depends on the number of electrons per gram (electron density). Most materials are considered to have approximately the same number of electrons per gram, except hydrogen. For that reason, the Compton mass attenuation coefficient is nearly the same for all absorbing materials [5, 7].

The pair production can be occurred when the incident photon energy is higher than 1.02 MeV (twice the rest mass energy of an electron). The probability of the pair production increases with the atomic number of the absorbing material because the pair production takes place in the coulomb field of a nucleus. The photon disappears and an electron-positron pair is created as a result of the pair production. The excess energy of the photon (above 1.02 MeV) is shared by the electron and the positron as kinetic energy.

2.1.2 The interaction of low energy x-rays with high atomic number materials [8-14]

The photoelectric absorption is a predominant mode of photon interaction in high atomic number absorbing materials for low energy photons, up to hundreds of keV (Figure 2.2). The probability of the photoelectric interaction strongly depends on the atomic number of the absorbing material and the energy of the incident photon (Eq. 2.1). When the photon energy is just above the binding energy of an atomic electron, the probability of photoelectric interaction shows a sudden increase and decreases sharply as increasing energy. Therefore, as the photon energy increases above the binding energy of K- shell electron, the photoelectric effect decreases rapidly with energy and the Compton scattering becomes more important.

The absorption edges appear at the binding energies of atomic electrons in the various shells in low photon energy region. The photoelectric interaction preferentially takes place in K-shell when the incident photon energy exceeds the K-shell binding energy. Figure 2.3 - 2.6 represent the mass attenuation coefficient and the mass energy-absorption coefficient of soft tissue (Z_{eff}=7.22) and high atomic number materials, such as iodine (Z=53), barium (Z=56), gadolinium (Z=64), tungsten (Z=74), gold (Z=79), and bismuth (Z=83), as a function of photon energy [12, 14].

Based on these properties, high atomic number materials can be used as radiosensitizers in kilovoltage x-ray beams. Tumors can absorb much more radiation doses by loading high atomic number nanoparticles on the tumor volume. The energy deposited by the photoelectric interaction products, Auger

electrons and photoelectrons, escaping from high atomic number materials mainly contributes to the dose enhancement effect. These photoelectric interaction products have very short ranges and the high relative biological effectiveness (RBE) as much as high linear energy transfer (LET) radiations [8, 11, 13].

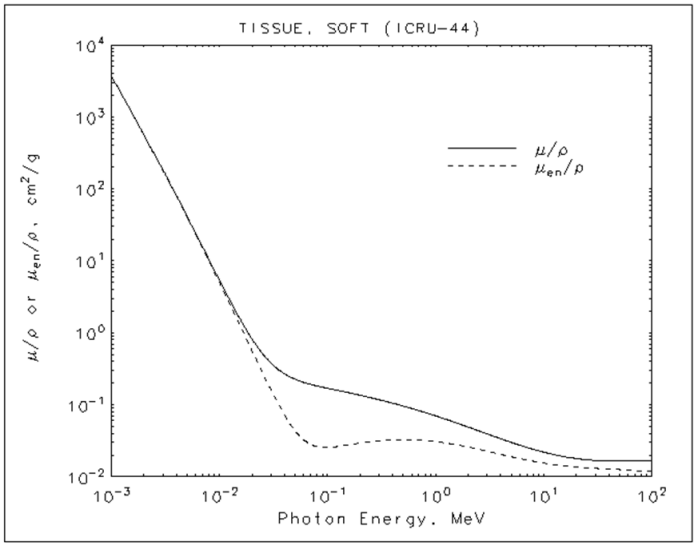

Figure 2.3. The mass attenuation coefficient, μ/ρ, and the mass energy-absorption coefficient, μ_{en}/ρ, as a function of photon energy, for soft tissue (Z_{eff}=7.22). Atomic absorption edges are indicated by the shell designation [14].

(A)

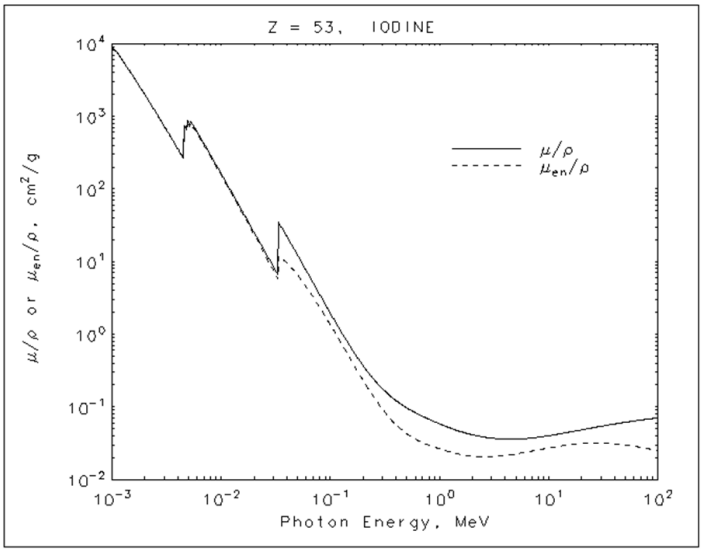

(B)

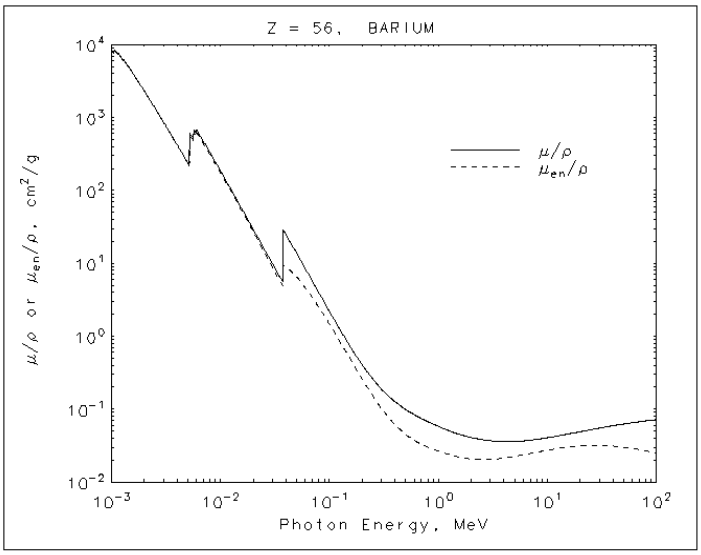

Figure 2.4. The mass attenuation coefficient, μ/ρ, and the mass energy-absorption coefficient, μ_{en}/ρ, as a function of photon energy, for (A) iodine (Z=53) and (B) barium (Z=56). Atomic absorption edges are indicated by the shell designation [14].

(A)

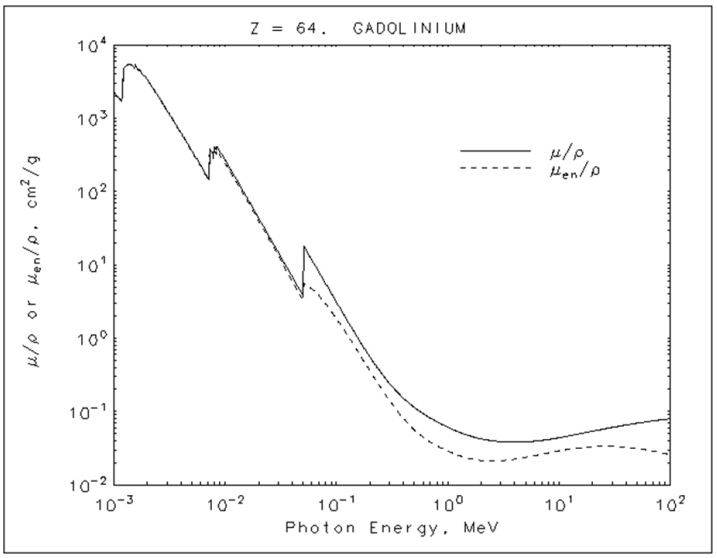

(B)

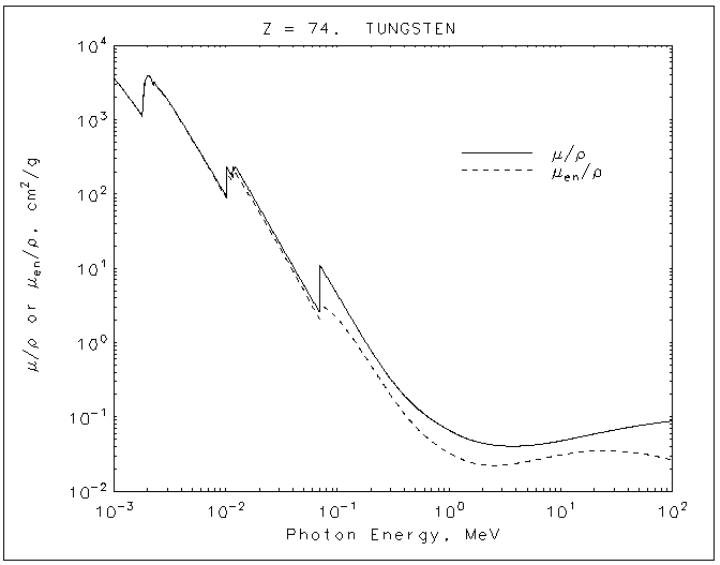

Figure 2.5. The mass attenuation coefficient, μ/ρ, and the mass energy-absorption coefficient, μ_{en}/ρ, as a function of photon energy, for (A) gadolinium (Z=64) and (B) tungsten (Z=74). Atomic absorption edges are indicated by the shell designation [14].

(A)

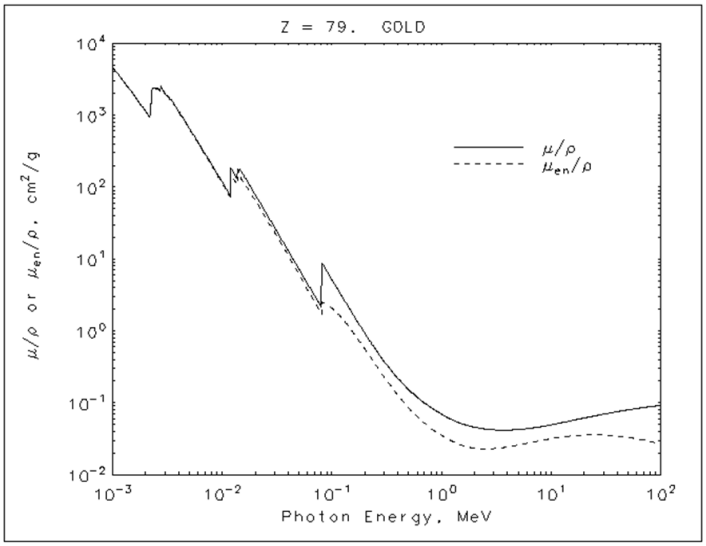

(B)

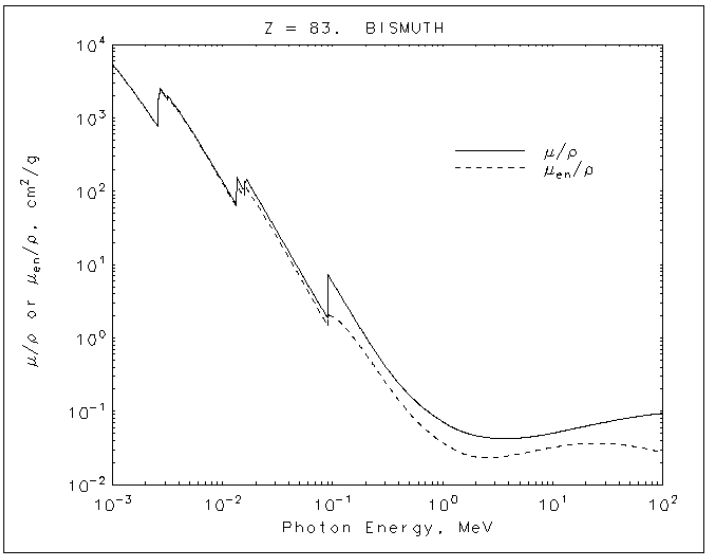

Figure 2.6. The mass attenuation coefficient, μ/ρ, and the mass energy-absorption coefficient, μ_{en}/ρ, as a function of photon energy, for (A) gold (Z=79) and (B) bismuth (Z=83). Atomic absorption edges are indicated by the shell designation [14].

2.1.3 Low energy electrons produced by the photoelectric interactions [5, 8, 9, 12, 15-18]

In photoelectric process (Figure 2.7), the ejected electron (called photoelectron) energy is equal to $h\nu - E_b$, where E_b is the binding energy of an electron in its original shell. Thus, more energetic incident photons produce higher energy of the photoelectron. As a result of the emission of the photoelectron, the vacancy is generated in the inner shell and filled by the outer shell electron. The excess energy is released by the atom through electron transition from an outer shell to an inner shell gives rise to the characteristic x-rays or low-energy monoenergetic electrons (known as Auger electrons).

The emission of an Auger electron is illustrated in Figure 2.8. The downward arrow stands for the electron transition from the L_{I} into K-shell vacancy, lead to releasing an energy equal to the difference of binding energies (E_k-$E_{L\,I}$). As the substitute for photon emission, this energy can transferred to an L_{III} electron, ejecting it from the atom with a kinetic energy ($KE=E_k-E_{L\,I}-E_{L\,III}$). Auger electron can be produced by other combinations of the electron shell levels [9].

The energetic electrons (~ 1 MeV) have low LET (~ 0.2 keV/μm) in soft tissue. In contrast, the LET of Auger electrons increases rapidly up to 26 keV/μm at very low energies [16, 18]. The range of Auger electrons is approximately below a nanometer and up to a few micrometers [18]. Table 2.1 and Figure 2.9 show the LET in soft tissue for electron energies and the LET

of electrons as a function of distance, respectively.

The LET of radiation is directly related to the degree of radiation induced biological damages. Figure 2.10 shows the RBE as a function of LET. The RBE is defined as by the ratio D_{250}/D_r, where D_{250} and D_r are the dose of 250 kVp x-rays and the test radiation (*r*) required for equal biologic effect, respectively [12, 17].

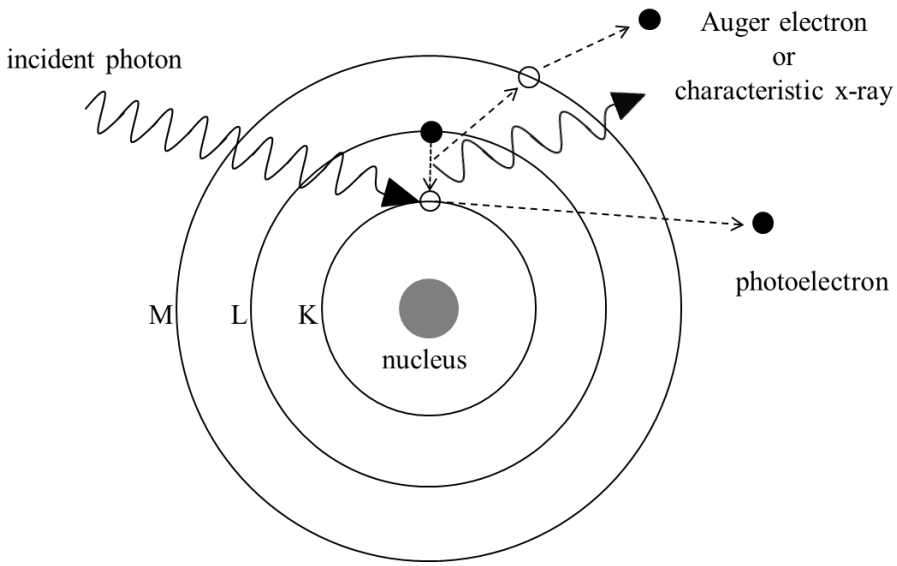

Figure 2.7. Schematic representation of the photoelectric process.

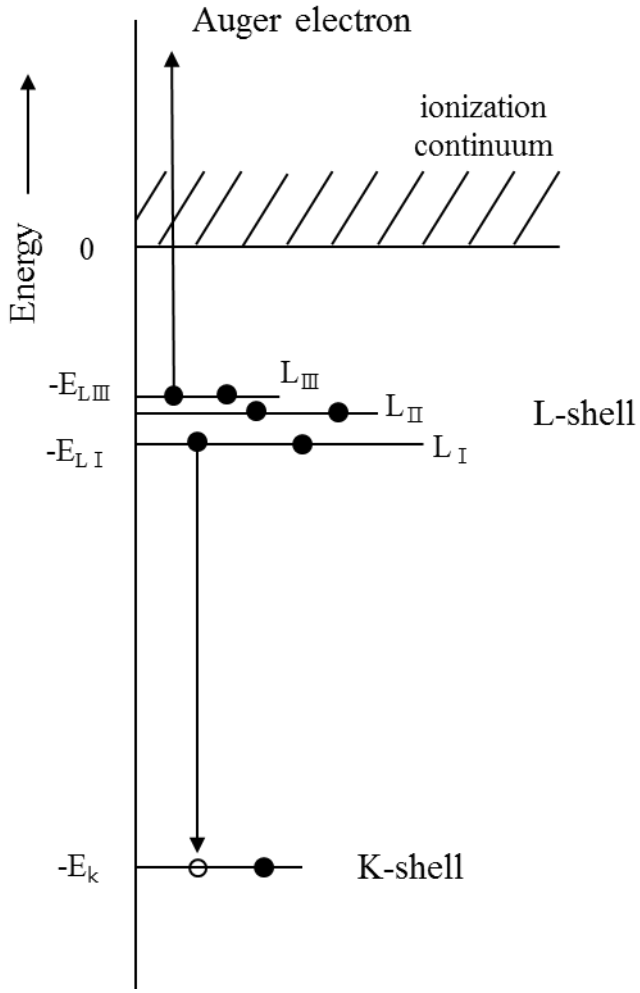

Figure 2.8. Schematic illustration of an atomic transition that results in the emission of Auger electron [9].

Table 2.1. The linear energy transfer (LET) values in soft tissue for electron energies [15].

Electron energy (keV)	LET (keV/μm)
1000	0.2
100	0.3
10	2.2
1	12.0

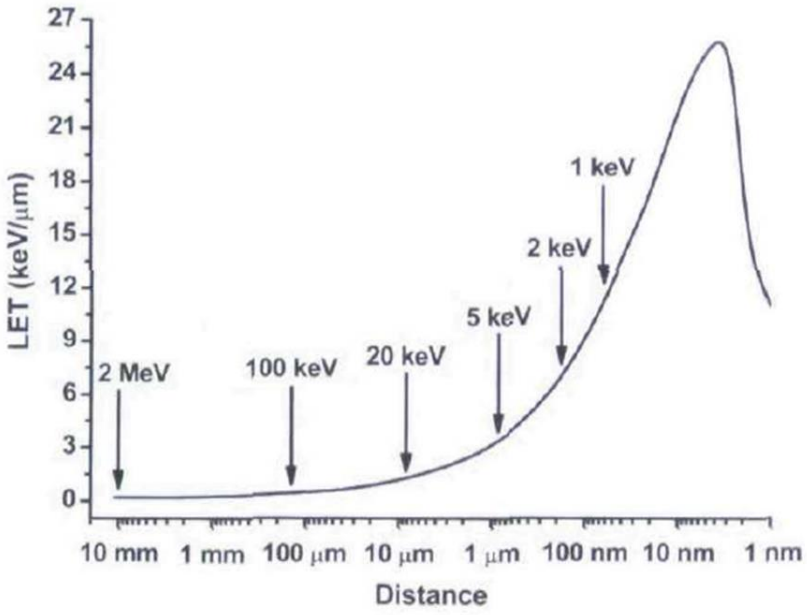

Figure 2.9. The LET of electrons as a function of distance. Electron energy values along the track are shown [16].

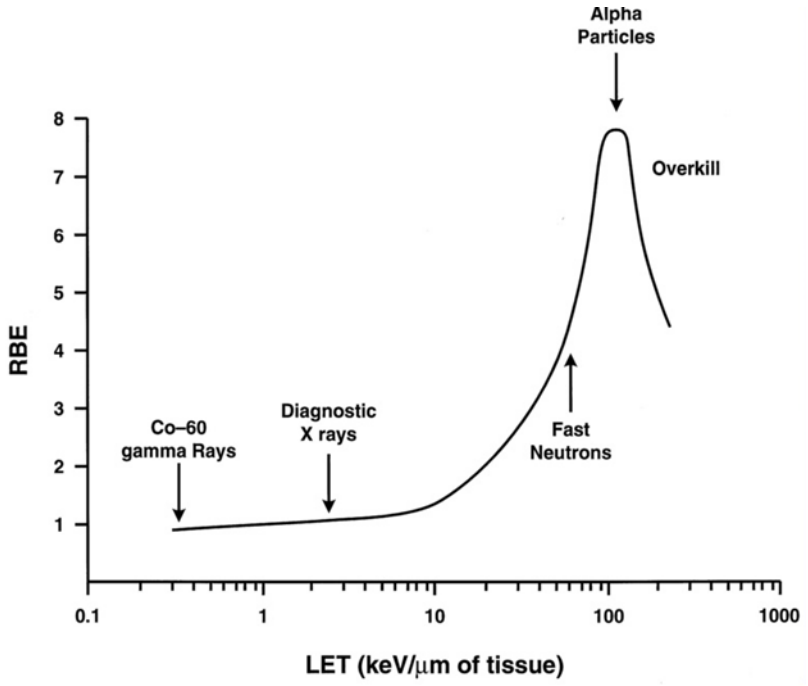

Figure 2.10. The relative biological effect (RBE) of a given radiation is an empirically derived term that, in general, all other factors being held constant, increases with the LET of the radiation. The RBE is defined as by the ratio D_{250}/D_r, where D_{250} and D_r are, respectively, the dose of 250 kVp x-rays and the test radiation (*r*) required for equal biologic effect [17].

2.1.4 The application of high atomic number nanoparticles in medical diagnostics and therapeutics [4, 6, 19-32]

The development of nanotechnology over the last decade has encouraged the use of high atomic nanoparticles in medical diagnostics and therapeutics [6, 20, 21, 26-28, 32]. Figure 2.11 illustrates the potential applications of high atomic number nanoparticles in medical diagnostics and therapeutics. Iodine-based agents have been used as the x-ray contrast agents, but these current agents have several shortcomings, such as short imaging times, toxicity, poor contrast, etc. To overcome those disadvantages, other high atomic number materials such as gold and gadolinium have been investigated and have shown the potential for the replacement of the current agents [19].

There has been growing interest in the use of high atomic number nanoparticles in cancer treatments, such as radiation therapy (as a dose enhancement agent) [4, 6, 20, 25, 26], photo-thermal therapy (as a heat generator) [6, 20-26, 32], chemotherapy (as an anticancer drug carrier) [6, 20, 32], and gene therapy (as a gene regulation agent) [20, 29-31], to improve the efficiency of the treatment and to minimize the side effects.

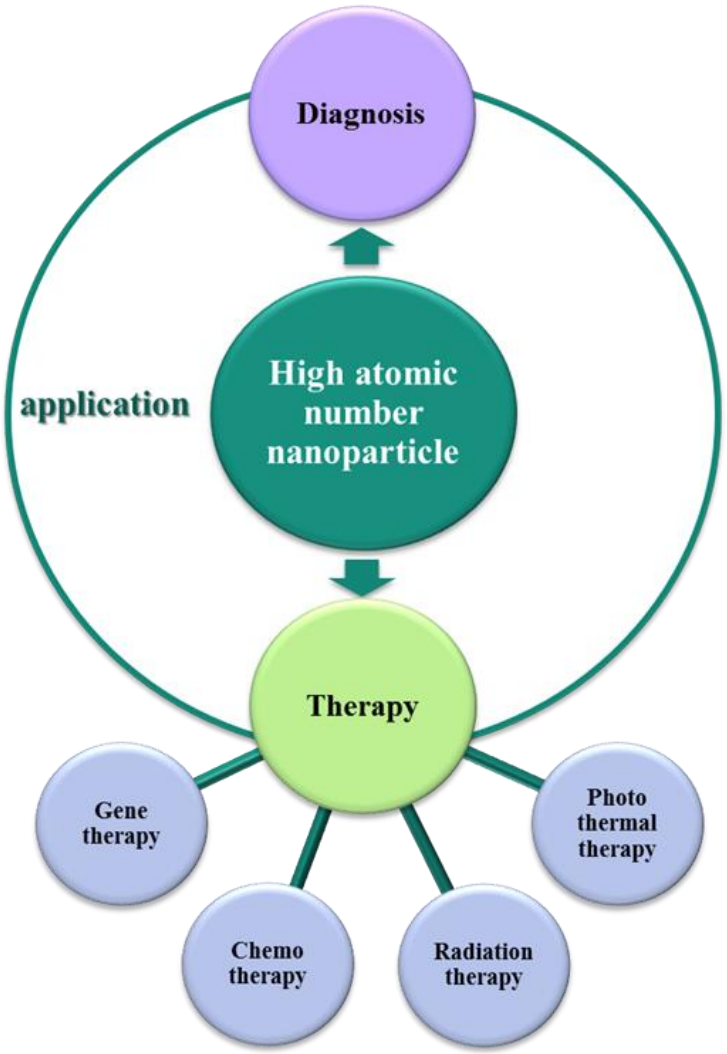

Figure 2.11. The potential applications of high atomic number nanoparticles in medical diagnostics and therapeutics.

2.2 AuNPs as a dose enhancement agent

The development of nanotechnology over the last decade has encouraged the use of high atomic nanoparticles for cancer treatment to overcome the limitation of conventional radiation therapy. High atomic number nanoparticles, such as iodine (Z=53), gadolinium (Z=64), and gold (Z=79), have been shown the potential to enhance the radiation effect in kilovoltage x-ray beams through *in vitro* [13, 33-40] and *in vivo* [41-43] experiments, and Monte Carlo simulations [3, 11, 44-48]. Among the various nanoparticles, AuNPs show a tremendous possibility as a dose enhancement agent in many aspects for radiation cancer therapy [4, 6, 32, 35].

2.2.1 The physical properties of AuNPs as a dose enhancement agent [4, 6, 14, 49, 50]

Figure 2.12 (A) shows the mass energy absorption coefficient of gold (Z=79) and soft tissue (Z_{eff}=7.22), as a function of the photon energy [14]. Table 2.2 represents the absorption edges for gold and the mass attenuation coefficient, μ/ρ, and the mass energy-absorption coefficient, μ_{en}/ρ, at each absorption edge. Based on these properties, AuNPs can be used as radiosensitizers in low photon energy region. The application of AuNPs as a dose enhancement agent is premised on the high photoelectric mass absorption coefficient of gold compared to soft tissue. Figure 2.12 (B) illustrates the ratio of gold mass energy absorption coefficient to soft tissue as a function of the incident photon energy. The photoelectric mass absorption

coefficient of tumor significantly increases by loading AuNPs on the tumor volume.

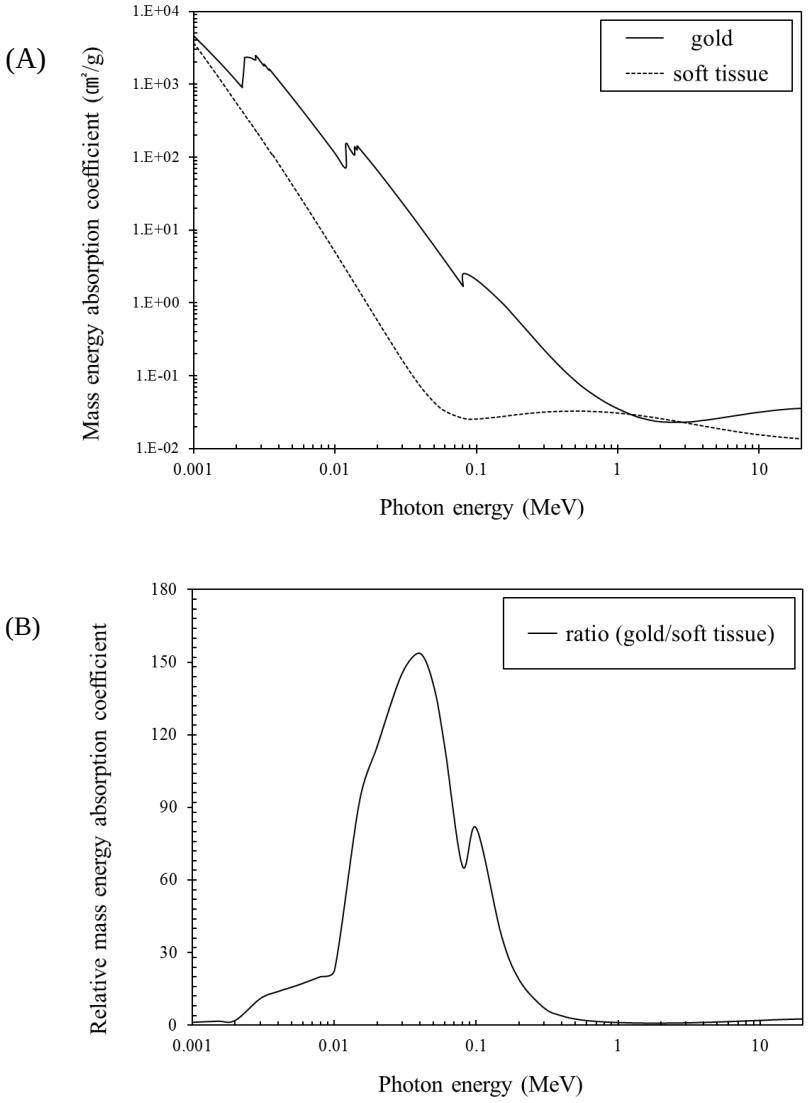

Figure 2.12. (A) Values of the mass energy-absorption coefficient, μ_{en}/ρ, as a function of photon energy, for gold (Z=79) and soft tissue (Z_{eff}=7.22). Data were taken from [14]. The composition of tissues was taken from ICRU Report 44 (1989). (B) Ratio of gold mass energy absorption coefficient to soft tissue [14, 49].

Table 2.2. The absorption edges for gold and the mass attenuation coefficient, μ/ρ, and the mass energy-absorption coefficient, μ_{en}/ρ, at each absorption edge [14].

Edge	Energy (keV)	μ/ρ (cm²/g)	μ_{en}/ρ (cm²/g)
M_5	2.206	9.971E+02	9.836E+02
M_4	2.291	2.389E+03	2.336E+03
M_3	2.743	2.541E+03	2.484E+03
M_2	3.148	1.933E+03	1.892E+03
M_1	3.425	1.652E+03	1.618E+03
L_3	11.919	1.870E+02	1.521E+02
L_2	13.734	1.764E+02	1.379E+02
L_1	14.353	1.830E+02	1.432E+02
K	80.725	8.904E+00	2.512E+00

2.2.2 Monte Carlo calculations of the dose enhancement effect [3, 11, 32, 44-48, 51]

Monte Carlo methods have been used to estimate the dose enhancement effect and dose distribution around AuNPs in the previous studies [3, 11, 32, 44-48, 51]. Table 2.3 shows the Monte Carlo simulation studies of radiation dose enhancement effect by AuNPs. There are common conclusions in the Monte Carlo studies. Firstly, smaller AuNPs can deposit more doses to surrounding materials than larger ones because of their greater surface to volume ratio. Secondly, the dose enhancement effect is proportional to the concentration of AuNPs. Thirdly, kilovoltage x-rays are more effective than megavoltage x-rays. Those three are general conclusions in the previous studies.

According to Lechtman et al. (2011) [11], a number of Auger electrons, photoelectrons, and characteristic x-rays are produced as a consequence of photoelectric effect and a portion of energy is internally absorbed, following the interaction of the incident photons with AuNPs. Energy distribution around AuNPs is divided into three regions. In the first region, Auger electrons escaping from AuNPs mainly deposit their energy. The range of Auger electrons is less than 2 μm from the surface of AuNP and 3-32 % of total escaping energy is deposited by Auger electrons. Auger electrons have relatively high LET, thus Auger electrons deposit their energy intensively within a few μm from the surface of AuNPs. In the second region, photoelectrons escaping from AuNPs deposit their energy. Photoelectrons

have much longer range up to hundreds of μm from the surface of AuNP and 42-69 % of total escaping energy is deposited by photoelectrons. The energy deposition by photoelectrons is high enough to cause a considerable number of DNA damages. In the third region, characteristic x-rays escaping from AuNPs deposit 11-42 % of total escaping energy. Characteristic x-rays can travel up to centimeters, but these will not cause the dose enhancement effect, because the LET of characteristic x-rays is not remarkably different from that of the incident photons.

Table 2.3. Simulation studies of radiation dose enhancement effect by gold nanoparticle (AuNP).

References	Monte Carlo code	AuNP		Radiation	Result
		Size	Concentration		
Cho et al. 2005 [44]	BEAMnrc/ DOSXYZnrc code (for external beam)	-	7, 18, 30 mg Au/g tumor	140 kVp x-ray	· DEF[a]: 2.11, 3.811. 5.061
				4, 6 MV	· Dose enhancing ranging from 1 to 7 %
	MCNP-5 (for brachytherapy)			^{192}Ir	· Dose enhancing ranging from 5 to 31 %
Cho et al. 2009 [47]	MCNP-5	-	7 mg Au/g tumor	^{125}I, 50 kVp, ^{169}Yb	· MDEF[b]: 68, 57, 44 % at 1.0 cm from the center of the source within a tumor
			18 mg Au/g tumor		116, 92, 108 %
			7, 18 mg Au/g tumor	^{192}Ir	30, 70 %

(Continued)

References	Monte Carlo code	AuNP		Radiation	Result
		Size	Concentration		
Zhang et al. 2009 [46]	Geant 4 Monte Carlo toolkit (version 4.8.1)	100 nm	10^{13} AuNPs/cm^3 water phantom	-	· Radiation dose enhancement around AuNPs up to 28 %.
Jones et al. 2010 [45]	EGSnrc and NOREC	-	-	^{169}Yb, ^{125}I, ^{103}Pd, 50 kVp x-ray	· Microscopic dose around AuNPs increased by factors ranging from: 10 to 1000 over 30 μm
				^{192}Ir, 6 MV x-ray	10 or less for distances greater than 1 μm
McMahon et al. 2010 [3]	Geant 4 Monte carlo toolkit (version 4.9.3)	2, 5, 10, 20, 30, 40, 50 nm	500 μg/ml	40 keV x-ray	· RBE_{LEM}^{c}: 2.07, 1.72, 1.45, 1.28, 1.2, 1.16, 1.13

(Continued)

References	Monte Carlo code	AuNP		Radiation	Result
		Size	Concentration		
		20 nm		20, 30, 40, 50, 60, 70, 80, 81, 85, 90, 100, 125, 150 keV x-ray	1.4, 1.33, 1.28, 1.22, 1.16, 1.11, 1.09, 1.35, 1.26, 1.19, 1.13, 1.06, 1.04
Lechtman et al. 2011 [11]	MCNP-5 and PENELOPE 2008	1.9, 5, 30, 100 nm	-	Photon source (average energy)[d] ^{103}Pd (20.6 keV), ^{125}I (27.0 keV), ^{169}Yb (100.7 keV), 300 kVp (127.1 keV), ^{192}Ir (324.3 keV), 6 MV (1861 keV)	· Examining the proportion of energy transferred to escaping particles or internally absorbed in the nanoparticle suggests two clinical strategies: · The first uses photon energies below the k-edge and takes advantage of the extremely localized Auger cascade.

(Continued)

References	Monte Carlo code	AuNP		Radiation	Result
		Size	Concentration		
					· The second, using photon sources above the k-edge, requires a higher gold concentration in the tumor region.
Berbeco et al. 2011 [48]	An analytic method incorporating the energy-loss formula of Cole	100 nm	7 to 140 mg/g	6 MV x-ray	· EDEF[e]: 1.2 to 4.4

DEF[a], dose enhancement factor which was defined as the ratio of the average dose in the tumor region (or voxel) with and without the presence of AuNPs; MDEF[b], macroscopic dose enhancement factor defined as the ratio of the average dose in the tumor region with and without the presence of AuNPs during the irradiation of the tumor; RBE_{LEM}[c], predicted relative biological effectiveness within the framework of the local effect model; Photon source (average energy)[d], average photon energy at tissue depth of 1 and 5 cm for brachytherapy sources and external beam sources, respectively; EDEF[e], endothelial dose enhancement factor is the ratio of the overall (externally plus internally generated) dose to endothelial cells in the presence of AuNPs to the dose without AuNPs (from the external beam only).

2.2.3 The biological application of AuNPs [4, 6, 28, 52-60]

AuNPs have been extensively investigated and used in biological applications due to their attractive properties as follows [6]. Firstly, AuNPs offer the advantage of greater biocompatibility [53, 57, 58] and low cytotoxicity [54, 55]. Secondly, the chemistry of AuNPs surface has been well known by a number of the previous researches [52]. Rich history of the surface chemistry can contribute to the design and the development of tumor-specific nanoparticles [52]. Thirdly, AuNPs can provide an excellent intracellular targeting vector for two reasons. AuNPs can be synthesized in the various sizes suitable for delivery to the specific target in the body and can be modified with the various small molecules, peptides, proteins, and DNA, etc [52, 56, 59].

In nanotechnology, nanoparticles are generally defined as having the size range of 1-100 nm [28]. The size of AuNPs can be synthesized from a few nanometers up to hundreds of nanometers, thereby placing them at the dimension of the cellular level. AuNPs are smaller than or comparable to those of animal cell (about 10-30 μm), cell nucleus (about 5 μm), chromosome (about 1-2 μm wide), mitochondria (about 0.4-1 μm), protein (about 3-10 nm), and DNA (2 nm wide and 10-100 nm long). Figure 2.13 illustrates the relative sizes of biological structures and nanoparticles in nano- and micro-scale. It implies that AuNPs can closely approach to the specific targets of the body. Table 2.4 and 2.5 represent the previous *in vitro* and *in vivo* studies of radiation dose enhancement effect by AuNP, respectively.

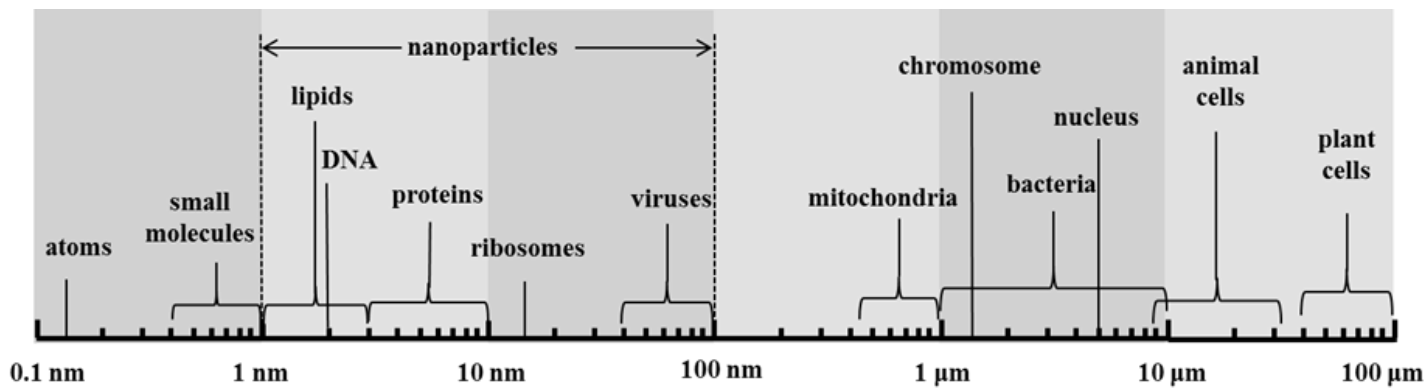

Figure 2.13. Relative sizes of biological structures and nanoparticles in nano- and micro-scale. Nanoparticles are generally defined as having the size range of 1-100 nm.

Table 2.4. *In vitro* studies of radiation dose enhancement effect by AuNP.

References	Cell line	AuNP			Radiation	Effect
		Size	Concentration	Incubation time		
Kong et al. 2008 [40]	MCF-7	10.8 nm	15 nM	48 h	200 kVp	· cytotoxicity increase by 35-40 %
					^{137}Cs (662 keV)	· No significant effect
					^{60}Co (average 1.25 MeV)	· No significant effect
Butterworth et al. 2008 [37]	TOP10	5 nm	50 μg/ml	-	160 kVp	· SSB and DSB enhancement factor[a, b]: 2.29, 1.25
		20 nm				2.21, 1.00
		1.5 μm				1.41, 1.12

(Continued)

References	Cell line	AuNP			Radiation	Effect
		Size	Concentration	Incubation time		
Rahman et al. 2009 [13]	BAECs	1.9 nm	0.25 mM	24 h	80 kVp x-ray 6 MeV electrons	· DEF[c]: 4 2.7
			0.5 mM		80, 150 kVp x-ray 6, 12 MeV electrons	20, 1.4 2.9, 3.7
			1 mM		80, 150 kVp x-ray 6, 12 MeV electrons	24.6, 2.2 4, 4.1
Roa et al. 2009 [39]	DU-145	10.8 nm	15 nM	24 h	^{137}Cs	· With 2 Gy, 1.5–2.0 fold enhancement in growth inhibition (compared to x-rays alone). · Accumulation of cells in the G_2/M phase at 29.8 % versus 18.4 % for controls.

(Continued)

References	Cell line	AuNP			Radiation	Effect
		Size	Concentration	Incubation time		
Zheng et al. 2009 [106]	Supercoiled plasmid DNA	5 nm	0.5 μM	-	60 keV electron	· Adding one AuNP to DNA enhances radiation-induced DSBs by a factor of 2.32. · Adding one AuNP to 10 DNA enhances radiation-induced DSBs by a factor of 1.44.
Butterworth et al. 2010 [35]	AGO-1522B	1.9 nm	10, 100 μg/ml	1 h	160 kVp x-ray	· DEF[d]: 1.16, 1.97
	Astro					1.04, 0.96
	DU-145					0.98, 0.81
	L132					0.86, 0.87

(Continued)

References	Cell line	AuNP			Radiation	Effect
		Size	Concentration	Incubation time		
	MCF-7					1.41, 1.09
	MDA-231-MB					1.67, 1.11
	PC-3					1.07, 1.02
	T98G					1.30, 1.91
Chithrani et al. 2010 [33]	HeLa	14 nm	7×10^9 NPs/ ml	24 h	220 kVp x-ray	· REF[e]: 1.20
		50 nm			105, 220 kVp, ^{137}Cs (660 keV), 6 MVp	1.66, 1.43, 1.18, 1.17
		74 nm			220 kVp	1.26
Liu et al. 2010 [36]	EMT-6	6.1 nm	0.4 mM	48 h	160 kVp x-ray	· DEF[d]: 1.24

(Continued)

References	Cell line	AuNP			Radiation	Effect
		Size	Concentration	Incubation time		
			0.5 mM		6.5 keV (Cu kα_1 x-ray), 8.048 keV (synchrotron x-ray)	1.35, 1.44
	CT26		0.5 mM		6 MV x-ray, 3 MV proton	1.32, 1.08
			1 mM		6 MV x-ray	2.10
Jain et al. 2011 [34]	MDA-MB-231	1.9 nm	12 μM	24 h	160 kVp, 6 MV, 15 MV x-ray 6, 16 MeV electrons	· SER[f]: 1.41, 1.29, 1.16 1.04, 1.35
	DU145				160 kVp, 6 MV x-ray 6 MeV electrons	0.92, 1.13 1.12

(Continued)

References	Cell line	AuNP			Radiation	Effect
		Size	Concentration	Incubation time		
	L132				160 kVp, 6 MV x-ray	1.05, 1.08
					6 MeV electrons	0.97
Geng et al. 2011 [38]	SK-OV-3 (HTB-77)	14.37 nm	5 nM	24 h	90 kVp x-ray	· Increased inhibition of cell proliferation: 30.48 %
					6 MV x-ray	26.88 %

SSB and DSB enhancement factor[a, b], DNA single strand break and double strand break enhancement factor, respectively; DEF[c], the ratio of the dose given to the control cell culture that produces 90 % survival divided by the dose given to cells treated with AuNPs that produces 90 % survival; DEF[d], the ratio of the dose required to give the same surviving fraction as that of the radiation only control cells at a dose of 2 Gy (SF_2); REF[e], the ratio of dose without AuNPs/ dose with AuNPs at 10 % survival; SER[f], sensitizer enhancement ratio.

Table 2.5. *In vivo* studies of radiation dose enhancement effect by AuNP.

References	Animal	Tumor cell line	AuNP			Radiation	Result
			Size	Concentration	Incubation time		
Herold et al. 2000 [41]	C.B17/ Icr scid mice	CHO-K1	1.5-3.0 μm	1 % Au solution		200 kVp x-ray	$DMF_{50\%}$, $DMF_{10\%}$, $DMF_{1\%}$ [a]: 1.36, 1.38, 1.38
		EMT-6					1.64, 1.54, 1.50
		DU-145					1.48, 1.43, 1.33
Hainfeld et al. 2004 [42]	Balb/C mice	EMT-6	1.9 nm	2.7 g Au/kg body weight	2 min	250 kVp x-ray	· Concentrations of gold up to 7 mg Au/g in tumors · Tumor-to-normal-tissue gold concentration ratios: approximately 8:1 · 1 year survival: 86 % with x-rays and AuNPs 20 % with x-rays alone

(Continued)

References	Animal	Tumor cell line	AuNP			Radiation	Result
			Size	Concentration	Incubation time		
Chang et al. 2008 [61]	C57BL/6 mice	B16F10	13 nm	10 nM	24 h	6 MeV electron	· Intravenous injection of AuNP combined with clinical electron beams significantly retards the tumor growth and prolongs survival of mice.
Hainfeld et al. 2010 [43]	C3H/HeJ mice	SCCVII	1.9 nm	1.9 g Au/ kg body weight		Median beam energy: 68 and 157 keV x-ray	· More effective at 42 Gy than at 30 Gy at 68 keV · More effective at 50.6 Gy than at 44 Gy at 157 keV · 68 keV was more effective than 157 keV

$DMF_{50\%}$, $DMF_{10\%}$, $DMF_{1\%}$ [a], dose modification factor obtained from the quotients of dose (without gold)/dose (with gold) for 50 %, 10 %, and 1 % cell survival.

2.3 Skin cancer therapy

2.3.1 Skin cancer [62, 63, 65-69, 157]

Skin cancer is the uncontrolled division and growth of abnormal skin cells. Unrepaired DNA damages cause mutations or genetic faults in skin cells, leading cells to form malignancy. There are three types of skin cancer, named for the type of cells that become malignant: basal cell skin cancer, squamous cell skin cancer, and melanoma.

Basal cell skin cancer is originated in the basal cell layer of the skin and the most common types of skin neoplasm [66, 68]. It is not fatal with disease and can be completely eliminated by the simple surgical excision [68]. Squamous cell skin cancer is originated in squamous cells and the second most common skin cancer. It is not easy to control, but not nearly as dangerous as melanoma [68]. These two types of skin cancer are grouped as non-melanoma skin cancer due to originating from skin cells other than melanocytes. They rarely spread to other parts of the body and the treatment methods are quite different from melanoma [67].

Melanoma begins in melanocytes, uncontrolled growth of pigment cells, and most melanocytes are in the skin [66, 67]. Melanoma accounts for less than 5 % of all skin cancer cases but it caused the majority of skin cancer deaths in the United States in 2013 [69]. Melanoma is intrinsically resistant to both radiation therapy and chemotherapy [64], thereby difficult to eliminate completely. Melanoma also tends to easily metastasize to other part of the

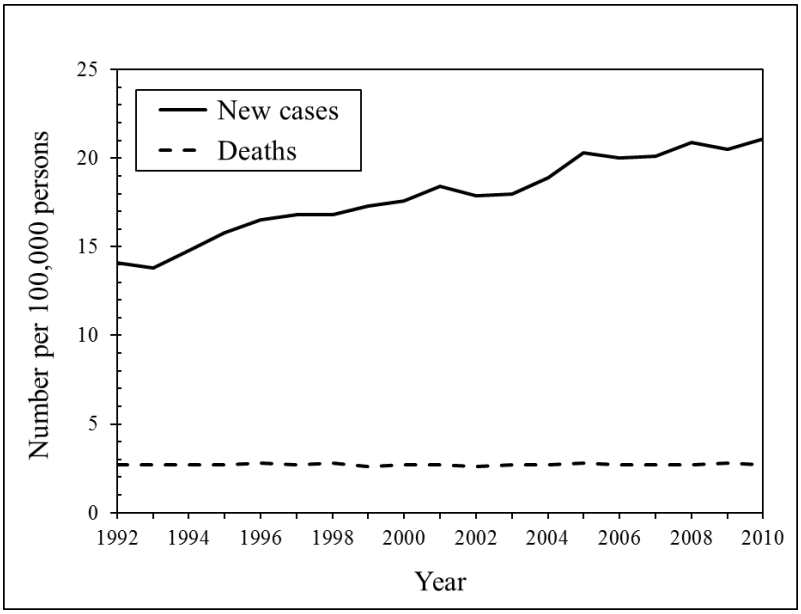

Figure 2.14. The number of new cases and deaths of skin melanoma per 100,000 people (all races, males and females) in the United States. These rates are age-adjusted and based on 1992 - 2010 cases and deaths. Age-adjusted rate, statistical method allowing comparisons of populations that takes into account age-distribution differences between populations [65].

body. The rates of melanoma have been increasing for at least 30 years [67] and melanoma causes more than 8000 deaths per year in the United States [65]. Figure 2.14 shows the number of new cases and deaths of skin melanoma per 100,000 people (all races, males and females). Those rates are age-adjusted and based on 1992 - 2010 cases and deaths [65].

The stage of melanoma is determined by how widespread it is. This includes its thickness in the skin, whether it has spread to other organs, and other factors. The stage of melanoma is important for planning the treatment. TNM system (American Joint Commission on Cancer (AJCC) guide line) is most widely used to stage melanoma. TNM stands for Tumor, Node, and Metastases. T describes the size (thickness) of the primary tumor (Table 2.6 and Figure 2.15). N describes whether lymph nodes contain cancer cells. M describes whether cancer has spread to another part of the body and whether it has invaded nearby tissue [111].

Table 2.6. T stages of melanoma. TNM (Tumor, Node, and Metastases) system (American Joint Commission on Cancer (AJCC) guide line) [111].

Stage	Tumor size	Approximate 5 year survival
Tis	the very top layer of the skin surface	100 %
T1	less than 1 mm thick	95 - 100 %
T2	1 ~ 2 mm thick	80 ~ 96 %
T3	2 ~ 4 mm thick	60 ~75 %
T4	more than 4 mm thick	50 %

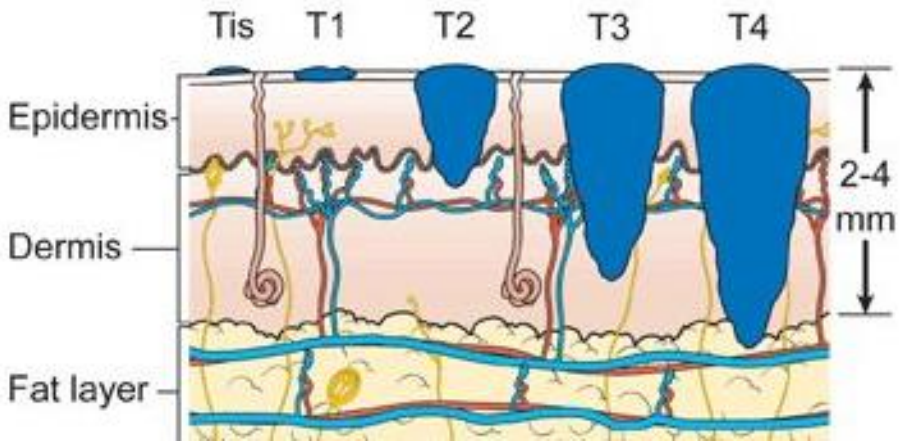

Figure 2.15. Illustration showing T stages of melanoma. TNM system (AJCC guideline) [111].

2.3.2 Radiation therapy for skin cancer [64, 70-74]

Radiation therapy for skin cancers requires the various considerations such as the dose per fraction, the total dose, the bolus use, the field size, the dose specification, the deep tissue dose, the differential bone absorption, and the ocular protection [70, 72]. These factors may have a significant impact on the treatment results. Therefore, it needs a careful consideration before and during proceeding of radiation therapy.

Radiation therapy is often applied for the skin lesions which are difficult or cosmetically sensitive to operate the surgical excision [71, 73]. Radiation therapy has advantages over functionally or cosmetically sensitive areas, especially the face, because the surgical excision may result in a serious deformity at the lesion [71]. Radiation therapy is also used for patients who have a large lesion or are not fit enough for a general anesthesia. In addition, radiation therapy can be used as an adjuvant therapy to try to prevent the recurrence of cancer [74].

According to Amdur et al. (1992) [70], kilovoltage x-ray and electron beam are generally used in radiation treatment of skin cancers. Electron beam has been commonly used for treating skin cancers to exploit the rapid fall-off the depth dose or because kilovoltage x-ray equipment is no longer widely used. However, the kilovoltage x-ray beams have more advantages than the electron beams for skin cancer therapy in many aspects, such as the easiness to shield eye, the simplicity of dose specification, and the ability to minimize field size, etc [70]. Table 2.7 shows the kilovoltage x-ray beam energy as a

function of the depth of target tumor from skin surface in skin cancer radiation therapy [75].

Table 2.7. Kilovoltage x-ray beam energy as a function of the depth of target tumor from skin surface in skin cancer radiation therapy [75].

	X-ray energy	**Depth of target tumor from skin surface**
Superficial therapy	50 ~ 200 kVp	~ 5 mm
Orthovoltage therapy	200 ~ 500 kVp	~ 2 cm

2.3.3 Fractionation in skin cancer x-ray therapy [12, 75]

Conventional fractionated radiation therapy is based on the consequence of radiobiological experiments performed in France in the 1920s and in the 1930s. In most cases, Fractionation in radiation therapy provides more efficient tumor control for a given level of surrounding normal tissue damage than a single high dose. The 'Four Rs' of radiobiology is a basic principal for the efficiency of fractionation in conventional radiation therapy. The 'Four Rs' are as follows: Repair of sublethal damage, Reassortment of cells in the cell cycle, Repopulation, and Reoxygenation. It has been well known that fractionated radiation therapy increases tumor cell death by reoxygenation and reassortment of cells into radiosensitive phases and spares normal tissues by repair of sublethal damage and repopulation of normal cells between dose fractions [12].

The commonly used fractionation schedule for skin cancer treatment is as follows [75].

- 2-4 Gy per fraction per day
- 3-4 days per week
- up to 60 Gy

CHAPTER 3

MATERIALS AND METHODS

3.1 Cell lines and cell culture

Human skin melanoma cells (HTB-72; ATCC, Manassas, VA, USA) were cultured in Eagle's Minimum Essential Medium (EMEM) (ATCC) supplemented with 10 % (volume/volume (v/v)) fetal bovin serum (FBS) (Gibco, Grand Island, NY, USA). Human dermal fibroblast cells (hDF) were provided by Lee E, Kyung Hee University [110] and cultured in Fibroblast Growth Media-2 (FGM-2) Bulletkit (Lonza, Walkersville, MD, USA). Melanoma and fibroblast cells were incubated at 37℃ in a humidified incubator (Sanyo, Wood Dale, IL, USA) with 5 % CO_2. Rat gliosarcoma cells (CRL-2200; ATCC) were cultured in Dulbecco's Modified Eagle's Medium (DMEM) (Gibco) supplemented with 10 % (v/v) FBS and incubated at 37℃ in a humidified incubator with 10 % CO_2.

3.2 Gold-nanoparticles

50 ± 3 nm (in diameter) AuNPs were purchased from Sigma Aldrich (MO, USA). 1.9 nm AuNPs (gold core diameter) were purchased from Nanoprobes

Inc. (Yaphank, NY). Nanoparticles were suspended in culture medium to achieve the required concentration.

3.3 The observation of cellular localized AuNPs

Cells were plated into 35 mm culture dish (Nunc, Roskilde, Denmark) at concentration of 2.816×10^4 cells per culture dish with 2 ml of culture medium, incubated 24 h, and then AuNP solution (AuNPs in 1 ml of culture medium) was added to each culture dish. After 48 h incubation with AuNPs, the cellular localization of AuNPs was observed using light microscope (IX 71W; Olympus, Shinjuku, Tokyo, Japan) and transmission electron microscope (TEM) (JEM1010; Jeol, Akishima, Tokyo, Japan).

Light microscope: Microscopic views were obtained using an inverted microscope) with 40× objective lenses and a microscope digital camera (DP71; Olympus).

TEM: Cells were fixed in karnovsky's fixative solution (primary fixation, 2% paraformaldehyde and 2% glutaraldehyde (Electron Microscopy Science (EMS), Hatfield, PA, USA) in 0.05 M sodium cacodylate buffer, pH 7.5) for 2 h and postfixed in 2 % osmium tetroxide in 0.1 M cacodylate buffer for 2 h. After fixation, cells were stained en bloc in 0.5 % uranyl acetate (EMS) for 30 min and dehydrated with 30, 50, 70, 80, 90, and 100 % ethanol. Samples were infiltrated with Spurr's resin (a mixture of 1 g ERL 4221 (EMS), 0.03 g DMAE (EMS), 0.6 g DER 736 (EMS), and 2.6 g NSA (EMS)). The specimen

was cut into sections and stained on the TEM grid (200 mesh). The samples were imaged by using TEM at voltage of 80 kV.

3.4 Cytotoxicity assay

Cells were plated into 35 mm culture dish at concentration of 2.816×10^4 cells per culture dish with 2 ml of culture medium, incubated 24 h, and then the various concentrations of AuNP solution were added to each culture dish. After 48 h incubation with AuNPs, cells were treated with TrypLE EXPRESS (Gibco) for 5 min at 37℃ to detach cells from the bottom of the culture dish and make single cell suspension. Equal volumes of cell suspension and 0.4 % trypan blue (Gibco) was mixed to stain cells. The stained cell suspensions were loaded on a hemocytometer to count stained (non-viable) and unstained (viable) cells under an inverted microscope with 10× objective lenses.

3.5 Clonogenic survival assay

Cells were incubated with the various concentrations of AuNPs in 35 mm culture dishes for 48 h and exposed to the various dose levels of x-rays. After irradiation, cells were washed twice with phosphate-buffered saline (PBS) (Invitrogen, Carlsbad, CA, USA) to completely remove AuNPs contained in culture medium. Cells were made into single cell suspensions with TrypLE

Express as described previously and the appropriate number of cells was seeded onto 60 mm culture dishes (Nunc) for the colony formation. After 14 day (gliosarcoma cells) or 19 day (melanoma cells) incubation, the colonies were fixed with ethanol and stained with 5 % Giemsa staining solution (Sigma-Aldrich). The number of colonies containing more than 50 cells was counted as survivors and the surviving fractions were determined.

3.6 DNA double strand break analysis

Cells were incubated with the various concentrations of AuNPs in 35 mm culture dishes for 48 h and exposed to 2 Gy of x-rays. After irradiation, cells were washed twice with PBS and made into single cell suspensions with TrypLE Express as described previously. Cells were gently centrifuged at 300 × g for 5 min and the supernatant was discarded. 2×10^5 cells were suspended in 100 μl 1× Assay buffer (5× Assay buffer (Millipore, Billerica, MA, USA) was diluted to 1× with deionized water) and 100 μl Fixation buffer (Millipore), and incubated for 5 min on ice. Cells were centrifuged at 300 × g for 5 min, and the supernatant was discarded. The cells were permeabilized by adding 200 μl ice-cold 1× Permeabilization buffer (Millipore), and incubated for 5 min on ice. Cells were centrifuged at 300 × g for 5 min and the supernatant was discarded. Cells were suspended in 90 μl 1× Assay buffer and 10 μl antibody cocktail solution, and incubated for 30 min in the dark at room temperature. The antibody cocktail solution was prepared by mixing of equal

volumes of 20× Anti-phospho-Histone H2A.X (Ser139), Alexa Fluor 555 (Millipore) and 20× Anti-Histone H2A.X, PECy5 (Millipore). After incubation, 100 μl 1× Assay buffer was added to cells. Cells were centrifuged at 300 × g for 5 min and the supernatant was discarded. Cells were suspended in a microtube (Millipore) with 200 μl of 1× Assay buffer. Cell samples were analyzed by using a Muse^{TM} Cell Analyzer (Millipore).

3.7 Cell cycle analysis

Cells were plated into 35 mm culture dish at concentration of 2.816×10^4 cells per culture dish with 2 ml of culture medium, incubated 24 h, and then AuNP solution was added to each culture dish. After 48 h incubation with AuNPs, cells were exposed to 4 Gy of 150 kVp x-rays or not. Cells cycle was measured at 0, 6, 12, 24, 36, 48, and 72 h after irradiation and the experimental method is described in the following section.

Cells were washed twice with PBS and made into single cell suspensions with TrypLE Express as described previously. Cells were centrifuged at 300 × g for 5 min and the supernatant was discarded without disturbing the cell pellet. Cells were suspended in PBS and centrifuged at 300 × g for 5 min and the supernatant was discarded, again. The supernatant was removed and cells were resuspended in 50 μl of PBS by repeated pipetting several times. 1 ml of ice-cold 70 % ethanol was added to cells drop by drop for fixing cells. The ethanol-fixed cell suspension was frozen at -20℃ for 24 h. The 10^5 ethanol-

fixed cells were centrifuged at 300 × g for 5 min and the supernatant was discarded. The fixed cells were washed with PBS, suspended in 200 μl of Muse cell cycle reagent (Millipore), and then incubated for 30 min in the dark at room temperature. Cell samples were analyzed by using a Muse™ Cell Analyzer.

3.8 X-ray irradiation

Cells were irradiated at room temperature in the hard x-ray beam irradiation facility at Seoul National University. X-ray beam tube (YXLON model 450-D08) was operated at 150 or 450 kVp and 10 mA with a 3 mm-thick aluminum plate fitted over the 5 mm-thick beryllium window. The dose rates were 0.984 and 6 Gy/min for 150 and 450 kVp, respectively.

3.9 MCNP-5 simulation

MCNP-5 (Monte Carlo N-particle) calculations were performed to obtain the depth dose curves and the x-ray energy spectra in depth form the skin surface. Field size of 3.6 and 10 cm diameter and source to surface distance (SSD) of 20 and 50 cm diameter were used for 150 and 450 kVp x-ray beams, respectively. Those values of SSD and field size were generally used for superficial and orthovoltage x-ray therapy, respectively [5]. Energy spectra of the photon beam available from the YXLON model 450-D08 was provided by

Lee et al. (2012) [76].

3.10 Statistical analysis

Student's t-test was performed to determine whether the observed data were significantly different from each other. The significance was indicated by *p*-value less than 0.05.

CHAPTER 4

RESULTS

4.1 AuNPs distribution in cell culture medium

Figure 4.1 shows TEM images of spherical AuNPs with diameters of 1.9 and 50 nm. The dispersion stability of AuNPs can affect significantly on their final performances. These images were taken to observe the self-aggregation behavior of AuNPs in culture medium. No large aggregates were observed in 1.9 and 50 nm AuNPs solution, but small clusters of few nanoparticles were observed.

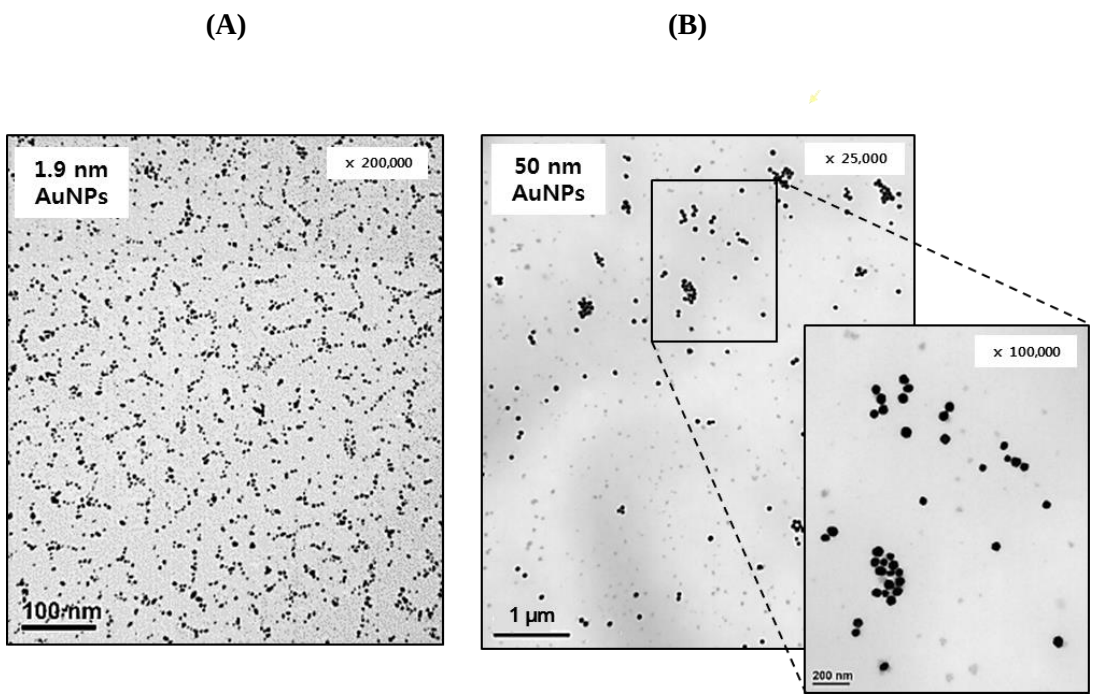

Figure 4.1. Transmission electron microscope (TEM) images of AuNPs with diameters of (A) 1.9 nm and (B) 50 nm in culture medium. TEM images were observed at a voltage of 80 kV.

4.2 Localization of AuNPs within melanoma and gliosarcoma cells

Figure 4.2 - 4.6 show the localization of AuNPs within melanoma and gliosarcoma cells after 48 h incubation with 1.9 and 50 nm AuNPs. AuNPs with diameter 50 nm showed much higher cellular uptake than 1.9 nm in both melanoma and gliosarcoma cells.

Figure 4.7 presents the uptake process of AuNPs and internalization in melanoma cells. It showed that AuNPs were endocyted by the cell in the form of clusters or single particles. Both single and cluster of AuNPs were observed in cytoplasm.

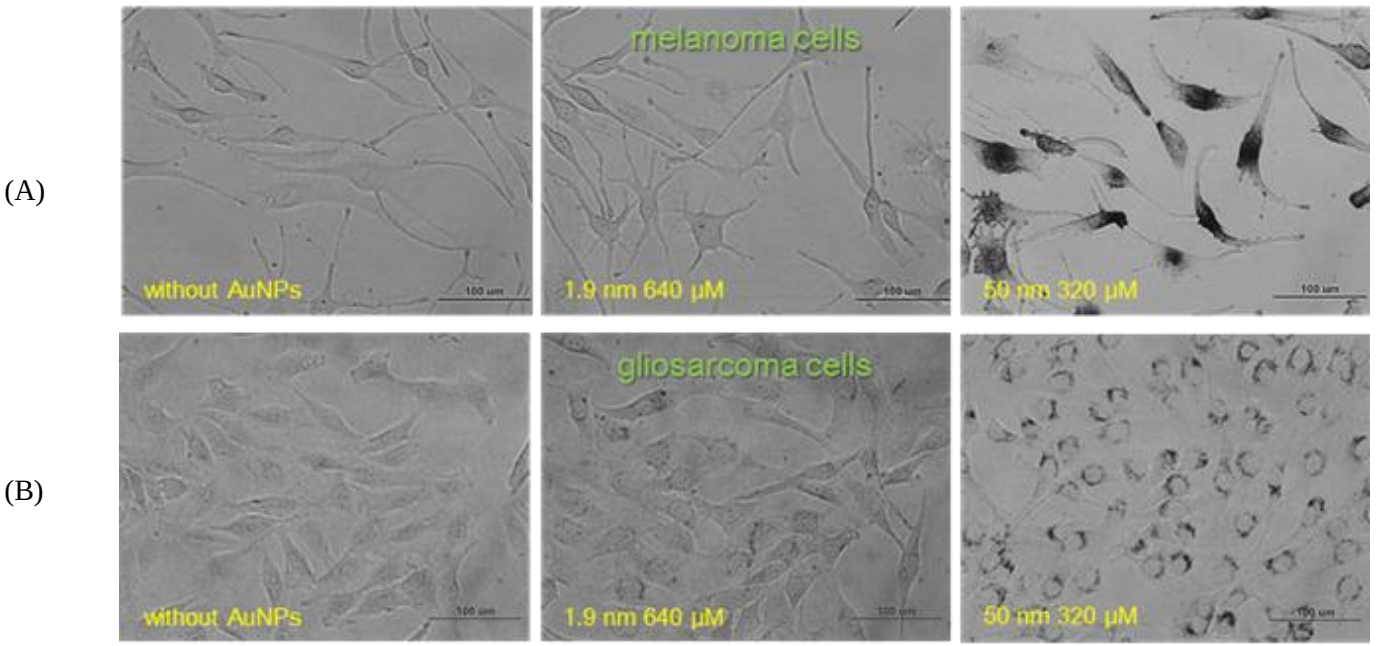

Figure 4.2. Microscopic images of cells after 48 h of incubation in the presence of AuNPs. (A) Melanoma and (B) gliosarcoma cells with no AuNP (left), 1.9 nm (middle), and 50 nm (right) in diameter, respectively. Microscopic images were observed under a light microscope with 40× objective lenses. Bar=100㎛.

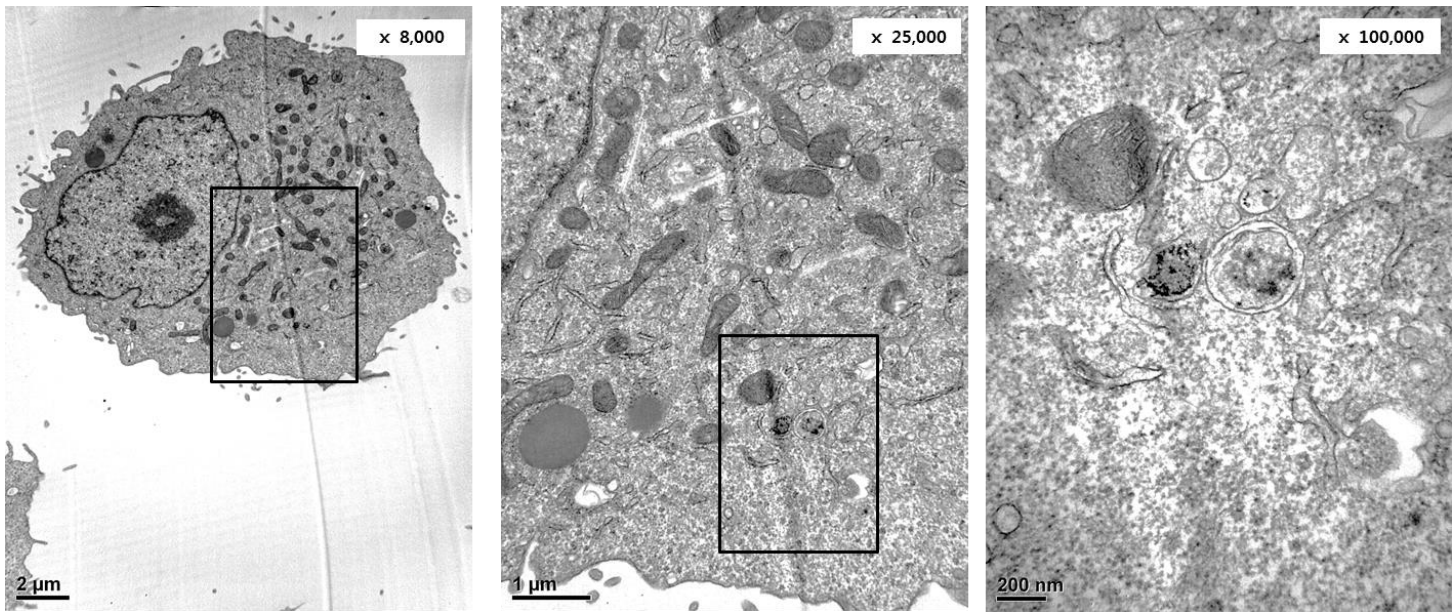

Figure 4.3. TEM images of melanoma cells after 48 h of incubation in the presence of 1.9 nm AuNPs. TEM images were observed at a voltage of 80 kV. Scale bars are 2 μm (left), 1 μm (middle), and 200 nm (right), respectively.

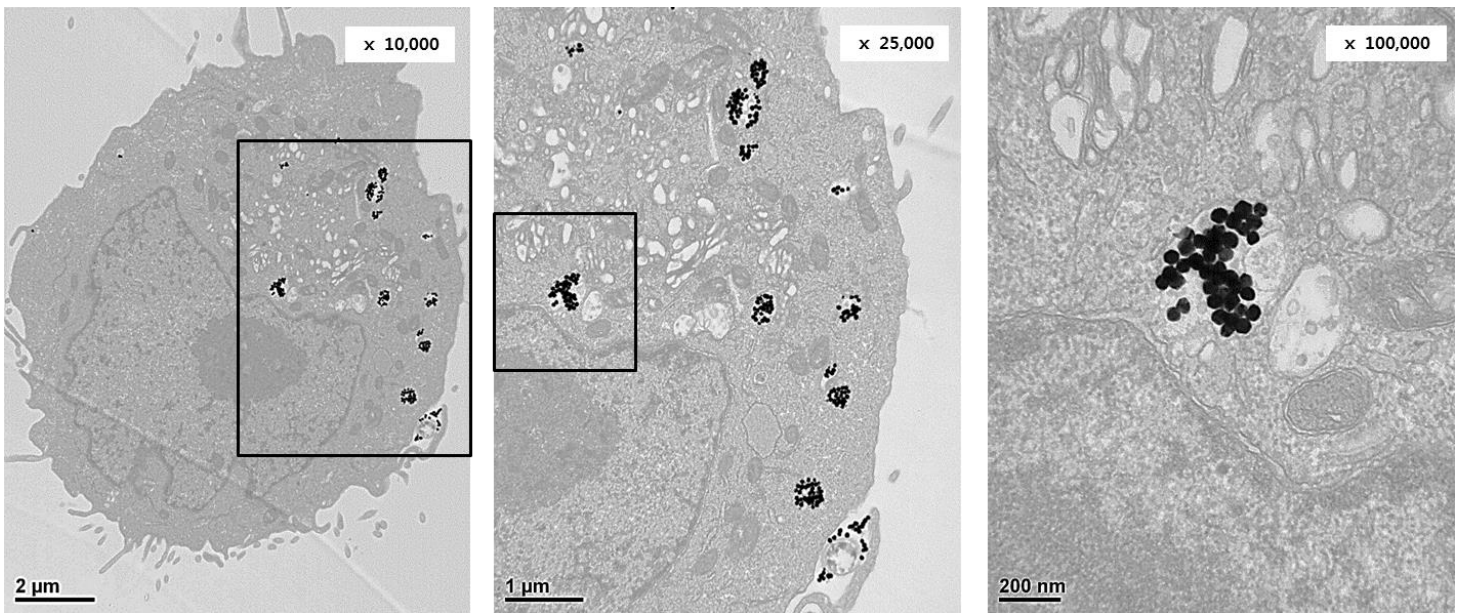

Figure 4.4. TEM images of melanoma cells after 48 h of incubation in the presence of 50 nm AuNPs. TEM images were observed at a voltage of 80 kV. Scale bars are 2 µm (left), 1 µm (middle), and 200 nm (right), respectively.

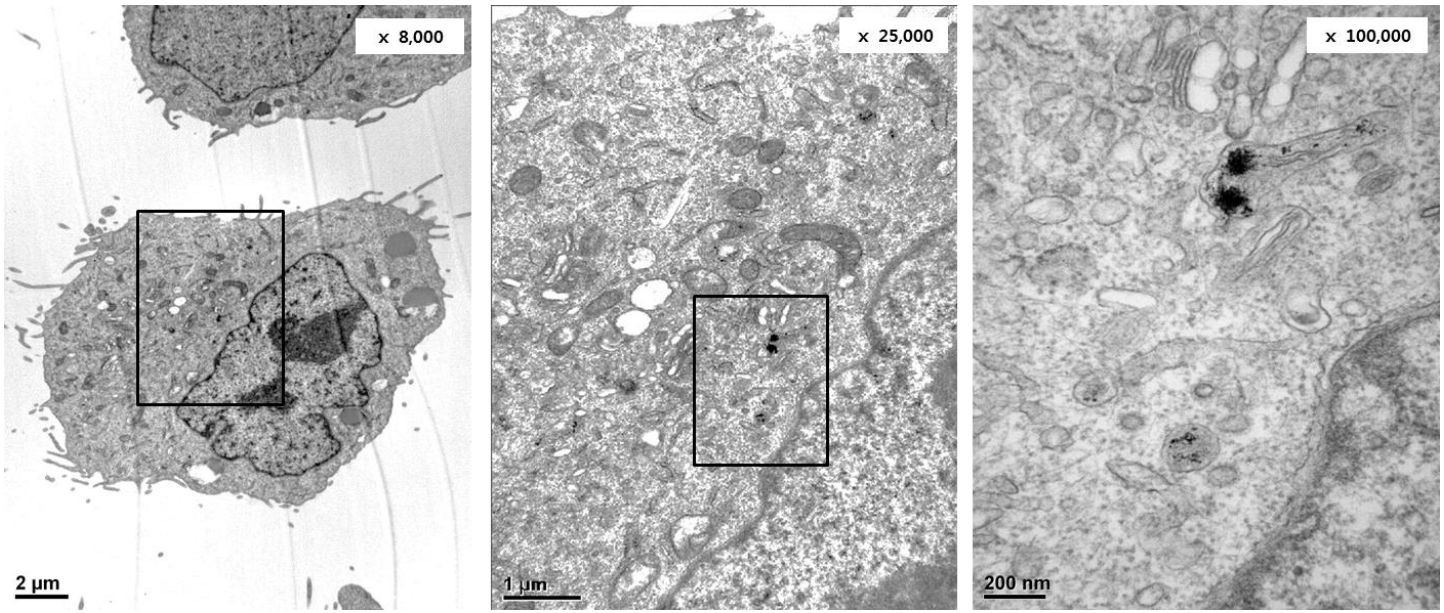

Figure 4.5. TEM images of gliosarcoma cells after 48 h of incubation in the presence of 1.9 nm AuNPs. TEM images were observed at a voltage of 80 kV. Scale bars are 2 μm (left), 1 μm (middle), and 200 nm (right), respectively.

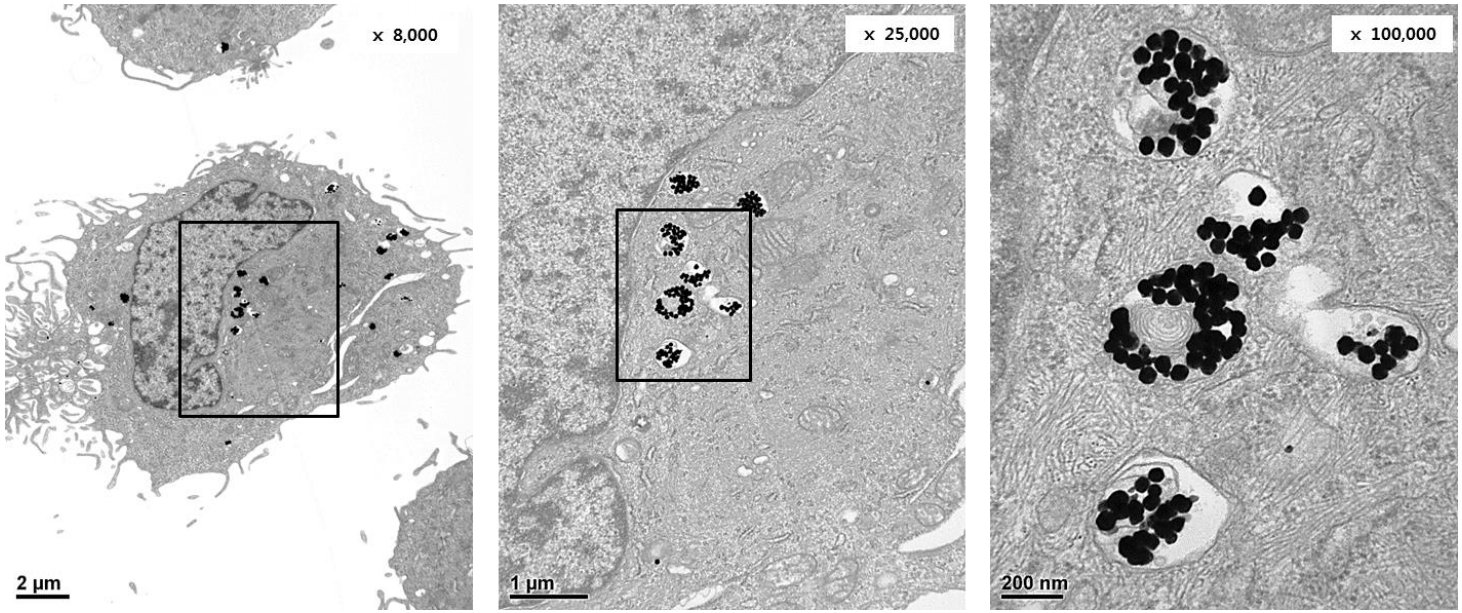

Figure 4.6. TEM images of gliosarcoma cells after 48 h of incubation in the presence of 50 nm AuNPs. TEM images were observed at a voltage of 80 kV. Scale bars are 2 μm (left), 1 μm (middle), and 200 nm (right), respectively.

(A) (B)

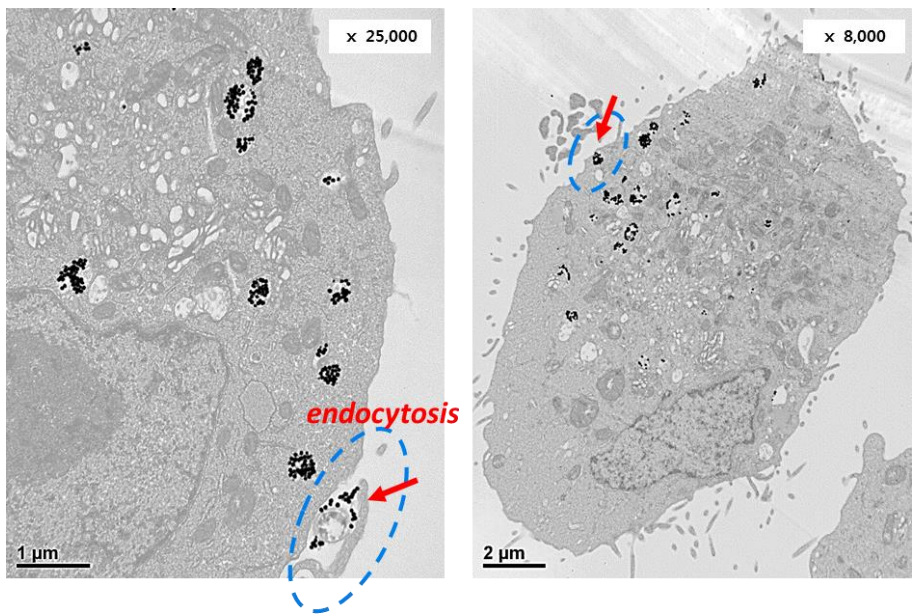

Figure 4.7. TEM images of endocytosis of 50 nm AuNPs in melanoma cells. (A) AuNPs on cell surface (arrow) (B) internalization (arrow). TEM images were observed at a voltage of 80 kV. Scale bars are 1 μm and 2 μm, respectively.

4.3 The cytotoxicity of AuNPs on melanoma and gliosarcoma cells

We measured the cytotoxicity of AuNPs on melanoma and gliosarcoma cells by using the dye exclusion assay. 1.9 and 50 nm AuNPs had no remarkable effect on the viability of gliosarcoma cells ($p>0.05$), while the viability of melanoma cells decreased as shown in Figure 4.8. 50 nm AuNPs slightly lowered viability of melanoma cells, but it was not serve cellular toxicity compared to 1.9 nm. 1.9 nm AuNPs had concentration-dependent toxicity on melanoma cells. The viability of melanoma cells was reduced to 0.77 ($p<0.05$) when cells were treated with 640 μM of 1.9 nm AuNPs for 48 h.

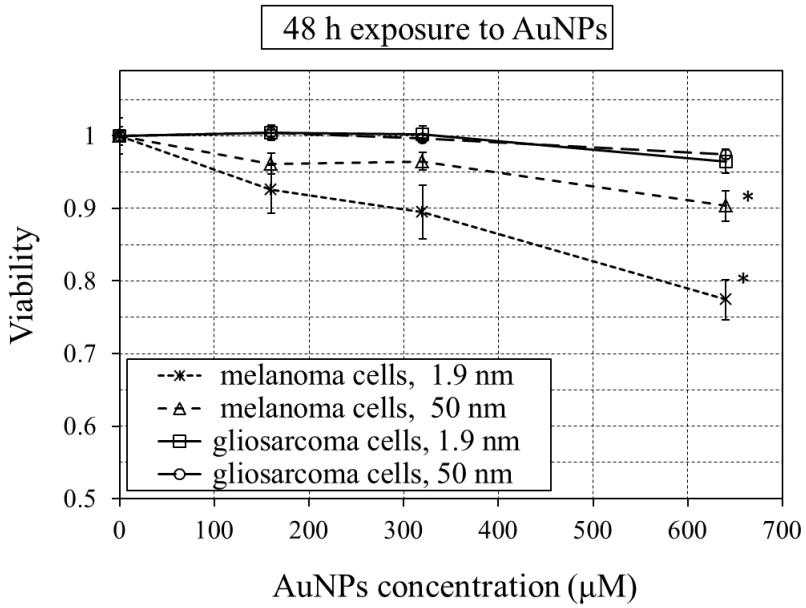

Figure 4.8. The cytotoxicity of AuNPs on melanoma and gliosarcoma cells. Cells were treated with 1.9 and 50 nm AuNPs for 48 h. Error bars indicate one standard error of the mean for four independent experiments. Data sets of significant difference ($p<0.05$) to control are indicated by asterisk.

4.4 The effect of AuNP size and concentration on cellular dose enhancement

Figure 4.9 shows ratio of SF_{4Gy} for melanoma and gliosarcoma cells exposed to 1.9 and 50 nm AuNPs for 48 h and irradiated with 4 Gy of 150 kVp x-rays. Ratio of SF_{4Gy} was defined as:

$$\text{Ratio of } SF_{4Gy} = \frac{SF_{4Gy} \text{ of cells without exposure to AuNPs}}{SF_{4Gy} \text{ of cells with exposure to AuNPs}} \quad (4.1)$$

SF_{4Gy} indicates clonogenic surviving fraction at 4 Gy. According to the definition, ratio more than 1 can be interpreted to increase radiosensitivity.

The concentration of 1.9 nm AuNP solution was treated on cells up to 1000 μM. The result indicated that the dose enhancement effect reached a plateaue at about 640 μM for both melanoma and gliosarcoma cells. The concentration of 50 nm AuNP solution was treated on cells up to 640 μM. The result also showed that the dose enhancement effect reached a plateaue at about 320 μM for both melanoma and gliosarcoma cells.

In melanoma cells, ratio of SF_{4Gy} increased from 1.63, 3.06 to 3.29 as the concentration of 50 nm AuNPs increases from 160, 320 to 640 μM, respectively. The corresponding values were 1.24, 1.62 to 1.72 in gliosarcoma cells. Melanoma cells showed much higher ratio of SF_{4Gy} than gliosarcoma cells when cells were exposed to 50 nm AuNPs. In melanoma cells, ratio of SF_{4Gy} increased from 1.19, 1.41 to 1.39 as the concentration of 1.9 nm AuNPs increases from 320, 640 to 1000 μM, respectively. The corresponding values

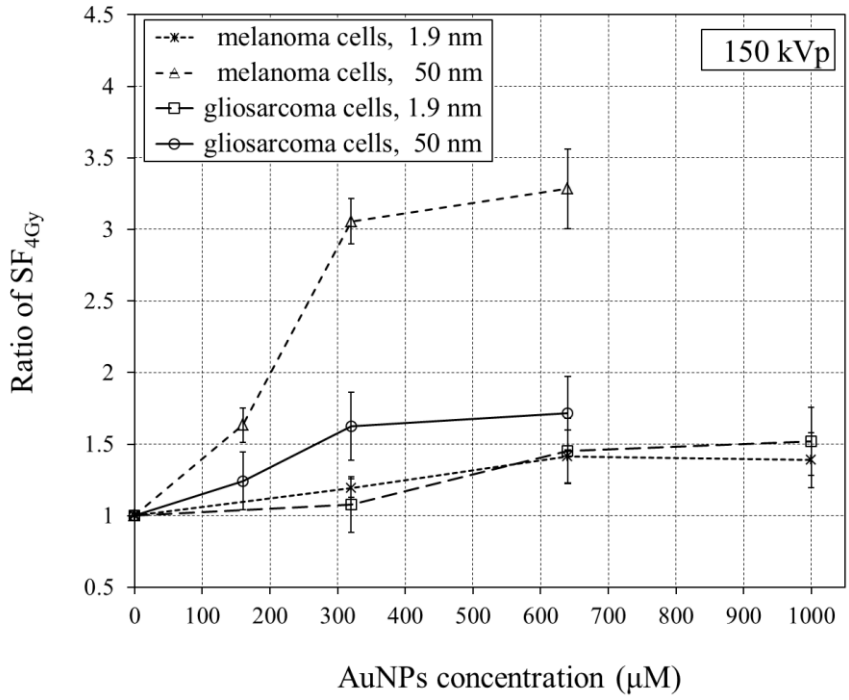

Figure 4.9. Ratio of SF_{4Gy}. Melanoma and gliosarcoma cells were treated with 1.9 and 50 nm AuNPs for 48 h and irradiated with 4 Gy of 150 kVp x-rays. The values of SF_{4Gy} were taken from Figure 4.10 - 4.13. Error bars indicate on standard error of the mean for three to four independent experiments.

were 1.08, 1.45 to 1.52 in gliosarcoma cells. Ratio of SF_{4Gy} was not remarkably different between melanoma and gliosarcoma cells in case of treating with 1.9 nm AuNPs.

Figure 4.10 - 4.13 show the clonogenic surviving fractions of melanoma and gliosarcoma cells, treated with the various concentrations of 1.9 and 50 nm AuNPs for 48 h and irradiated with 0, 2, 4, 6, and 8 Gy of 150 kVp x-rays. By the linear quadratic model, surviving fraction (SF) is expressed as:

$$SF = e^{-\alpha D - \beta D^2} \tag{4.2}$$

for radiation dose D under constant α and β. The initial slope of cell survival curve relates to α and the quadratic component of cell killing, the curve to bend at higher doses, relates to β parameter [12]. The values of α, β, α/β ratio, and dose enhancement factor (DEF) from the linear quadratic fitting curves in Figure 4.10 - 4.13 are listed in Table 4.1 and 4.2. DEF was defined as the ratio of 4 Gy to dose required to produce the same surviving fraction with a dose enhancement agent (AuNP) as that of 4 Gy.

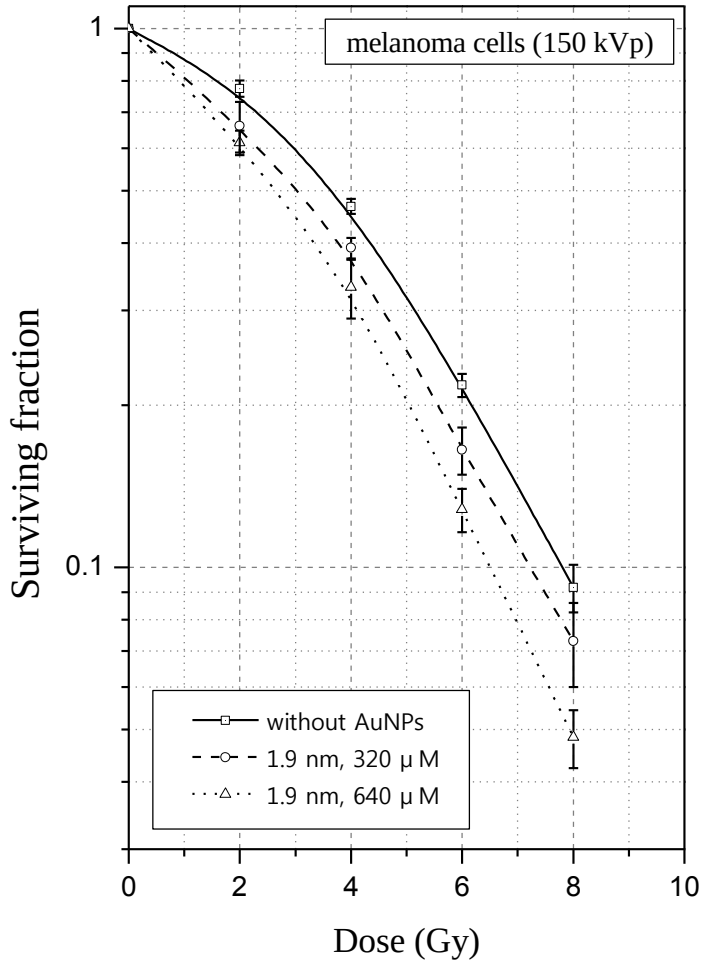

Figure 4.10. Clonogenic surviving fractions of melanoma cells treated with the various concentrations of 1.9 nm AuNPs for 48 h and irradiated with 0, 2, 4, 6, and 8 Gy of 150 kVp x-rays. Error bars indicate on standard error of the mean for three to four independent experiments.

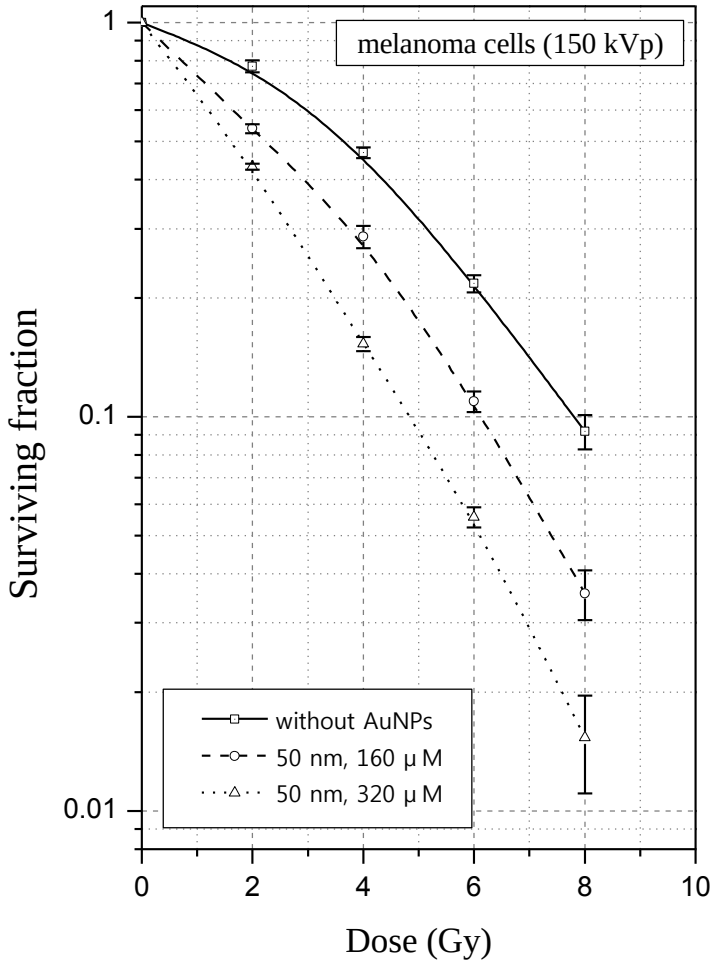

Figure 4.11. Clonogenic surviving fractions of melanoma cells treated with the various concentrations of 50 nm AuNPs for 48 h and irradiated with 0, 2, 4, 6, and 8 Gy of 150 kVp x-rays. Error bars indicate on standard error of the mean for three to four independent experiments.

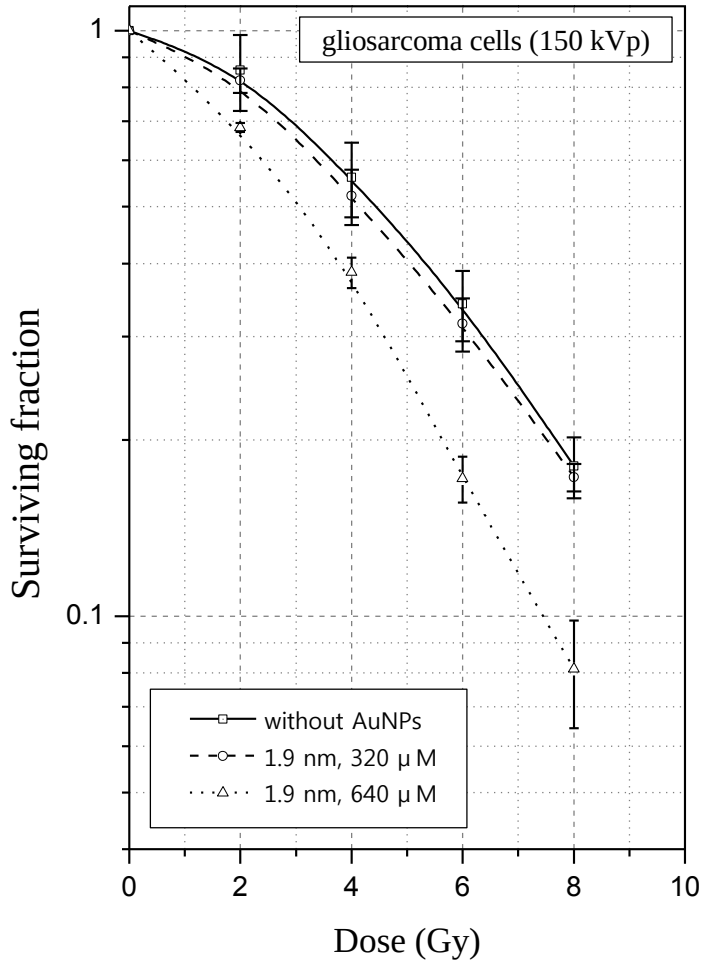

Figure 4.12. Clonogenic surviving fractions of gliosarcoma cells treated with the various concentrations of 1.9 nm AuNPs for 48 h and irradiated with 0, 2, 4, 6, and 8 Gy of 150 kVp x-rays. Error bars indicate on standard error of the mean for three to four independent experiments.

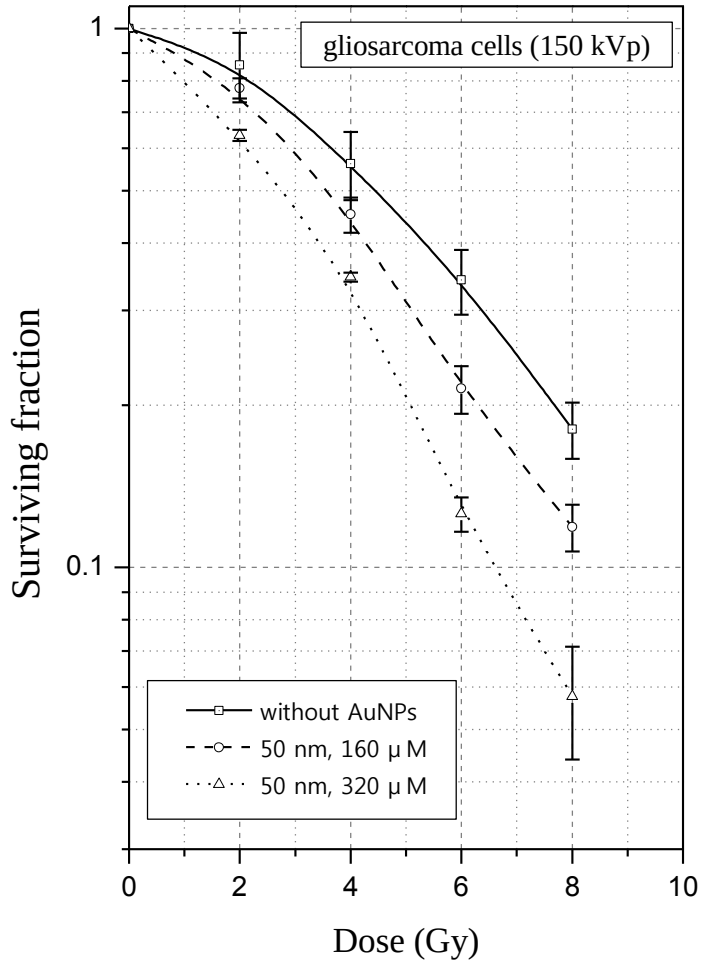

Figure 4.13. Clonogenic surviving fractions of gliosarcoma cells treated with the various concentrations of 50 nm AuNPs for 48 h and irradiated with 0, 2, 4, 6, and 8 Gy of 150 kVp x-rays. Error bars indicate on standard error of the mean for three to four independent experiments.

4.5 The effect of intracellular localization of AuNPs on cellular dose enhancement

To measure the dose enhancement effect of cellular localized AuNPs, culture medium containing AuNPs was renewed to fresh medium just before irradiation as illustrated in Figure 4.20. As shown in Figure 4.14 and 4.15, DEF for melanoma and gliosarcoma cells decreased from 1.41 to 1.06, and 1.49 to 1.02, respectively, as removing 1.9 nm AuNPs contained in culture medium. It meant that the dose enhancement effect of 1.9 nm AuNPs was mostly caused by photoelectric products escaping from AuNPs localized in culture medium, due to the low efficiency of cellular uptake, as presented in Figure 4.2 and 4.3, 4.5. As shown in Figure 4.14 and 4.15, in case of 50 nm AuNPs, DEF for melanoma and gliosarcoma cells decreased from 2.29 to 1.38, and 1.70 to 1.27, respectively, as removing 50 nm AuNPs contained in culture. It indicated that the dose enhancement effect of 50 nm AuNPs was caused by both extra- and intracellular localized AuNPs.

Figure 4.16 - 4.19 show the clonogenic surviving fractions of melanoma and gliosarcoma cells, treated with 1.9 nm (640 μM) and 50 nm (320 μM) AuNPs for 48 h and irradiated with 0, 2, 4, 6, and 8 Gy of 150 kVp x-rays. The experiments were performed by two different schemes as depicted in Figure 4.20. The values of α, β, α/β ratio and DEF from the linear quadratic fitting curves in Figure 4.16 - 4.19 are listed in Table 4.1 and 4.2.

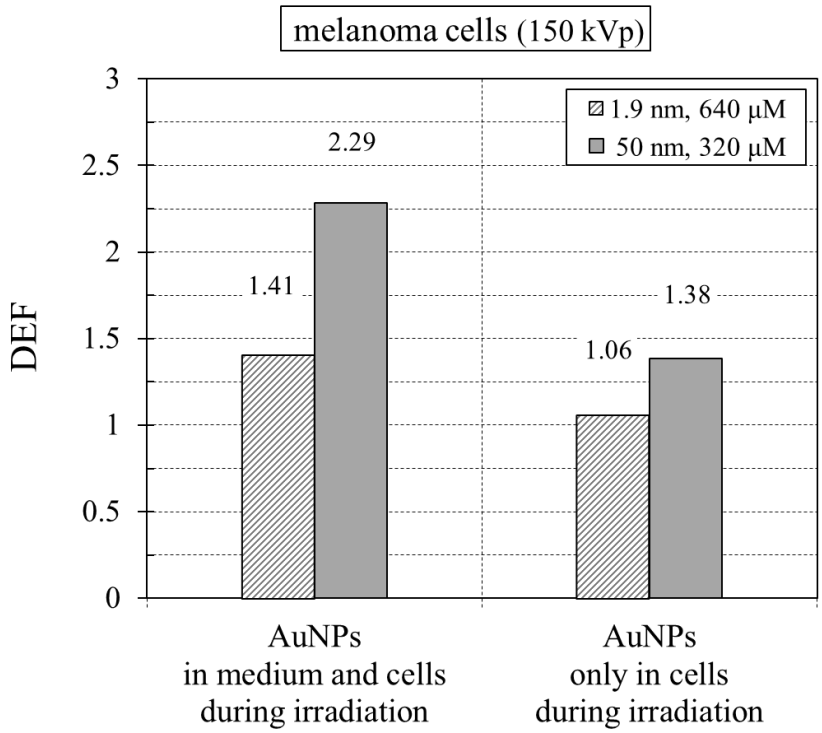

Figure 4.14. DEF for melanoma cells treated with 1.9 nm (640 μM) and 50 nm (320 μM) AuNPs for 48 h and irradiated with 4 Gy of 150 kVp x-rays. To measure the dose enhancement effect of cellular localized AuNPs, culture medium containing AuNPs was renewed to fresh medium just before irradiation. The experiment was performed by two different schemes as depicted in Figure 4.20. The values of DEF were taken from Figure 4.16 and 4.17. Error bars indicate one standard error of the mean for three to four independent experiments.

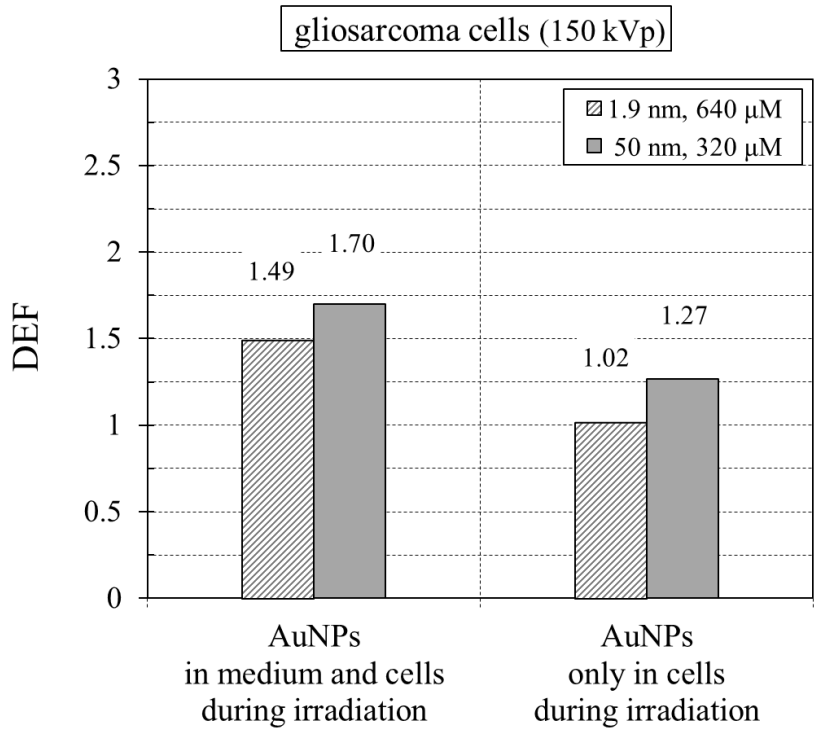

Figure 4.15. DEF for gliosarcoma cells treated with 1.9 nm (640 μM) and 50 nm (320 μM) AuNPs for 48 h and irradiated with 4 Gy of 150 kVp x-rays. To measure the dose enhancement effect of cellular localized AuNPs, culture medium containing AuNPs was renewed to fresh medium just before irradiation. The experiment was performed by two different schemes as depicted in Figure 4.20. The values of DEF were taken from Figure 4.18 and 4.19. Error bars indicate one standard error of the mean for three to four independent experiments.

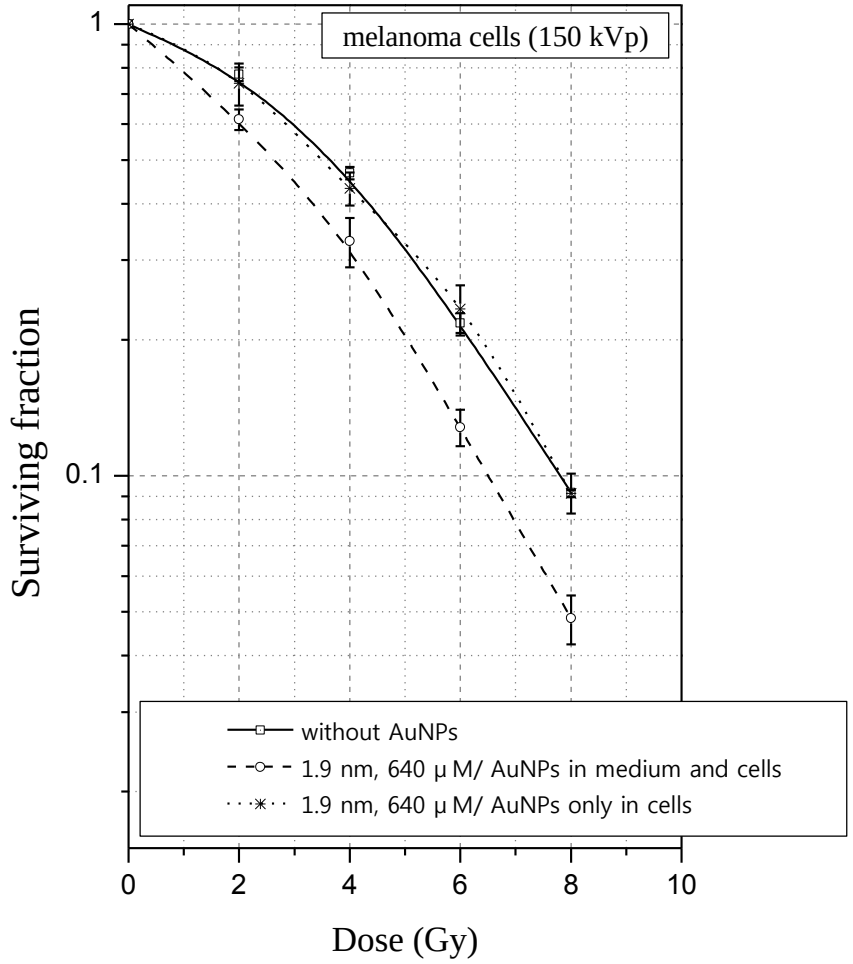

Figure 4.16. Clonogenic surviving fractions of melanoma cells treated with 1.9 nm (640 μM) AuNPs for 48 h and irradiated with 0, 2, 4, 6, and 8 Gy of 150 kVp x-rays. To measure the dose enhancement effect of cellular localized AuNPs, culture medium containing AuNPs was renewed to fresh medium just before irradiation. The experiment was performed by two different schemes as depicted in Figure 4.20. Error bars indicate on standard error of the mean for three to four independent experiments.

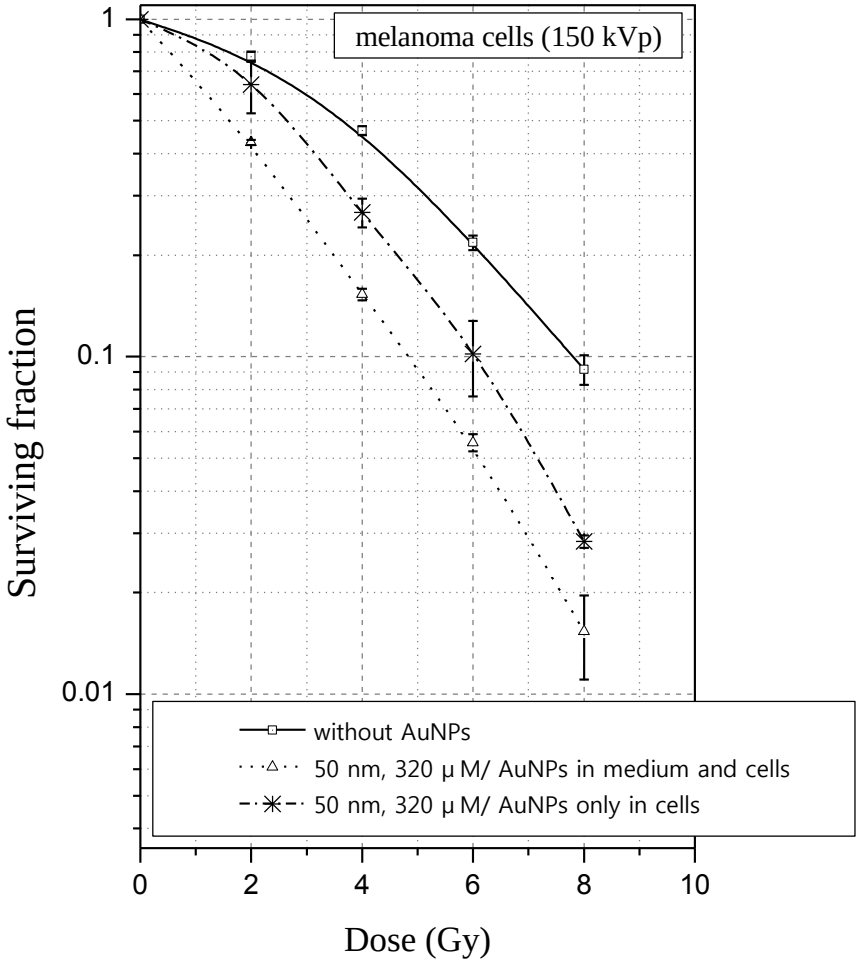

Figure 4.17. Clonogenic surviving fractions of melanoma cells treated with 50 nm (320 μM) AuNPs for 48 h and irradiated with 0, 2, 4, 6, and 8 Gy of 150 kVp x-rays. To measure the dose enhancement effect of cellular localized AuNPs, culture medium containing AuNPs was renewed to fresh medium just before irradiation. The experiment was performed by two different schemes as depicted in Figure 4.20. Error bars indicate on standard error of the mean for three to four independent experiments.

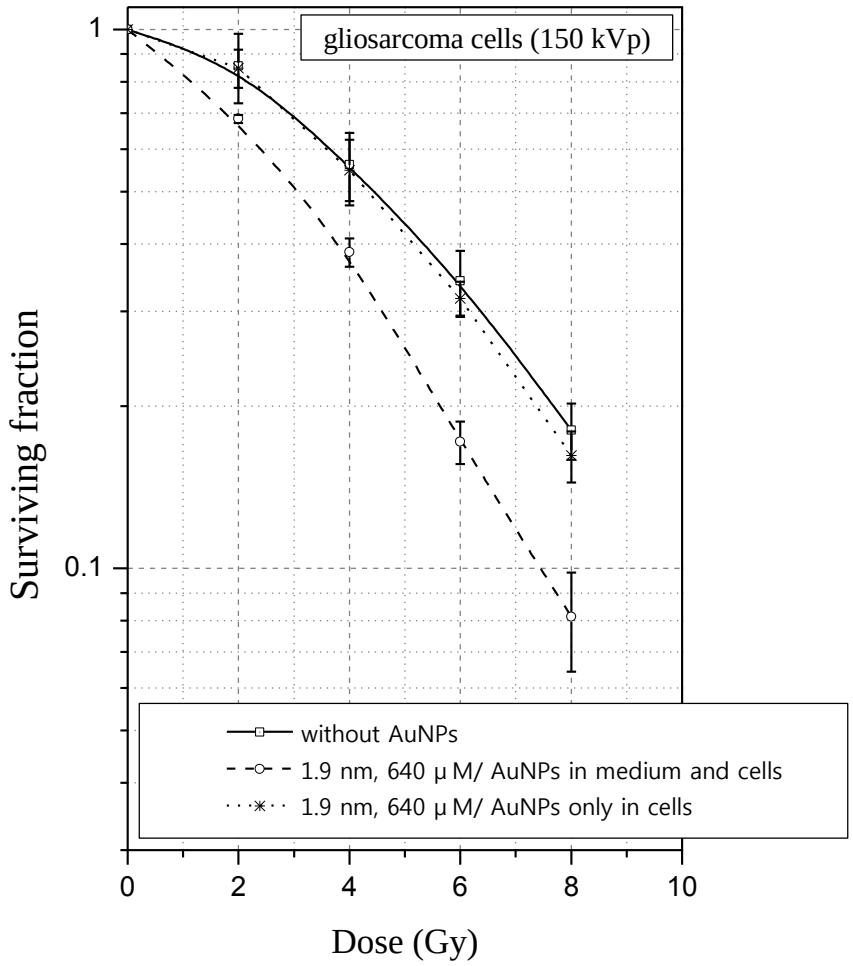

Figure 4.18. Clonogenic surviving fractions of gliosarcoma cells treated with 1.9 nm (640 μM) AuNPs for 48 h and irradiated with 0, 2, 4, 6, and 8 Gy of 150 kVp x-rays. To measure the dose enhancement effect of cellular localized AuNPs, culture medium containing AuNPs was renewed to fresh medium just before irradiation. The experiment was performed by two different schemes as depicted in Figure 4.20. Error bars indicate on standard error of the mean for three to four independent experiments.

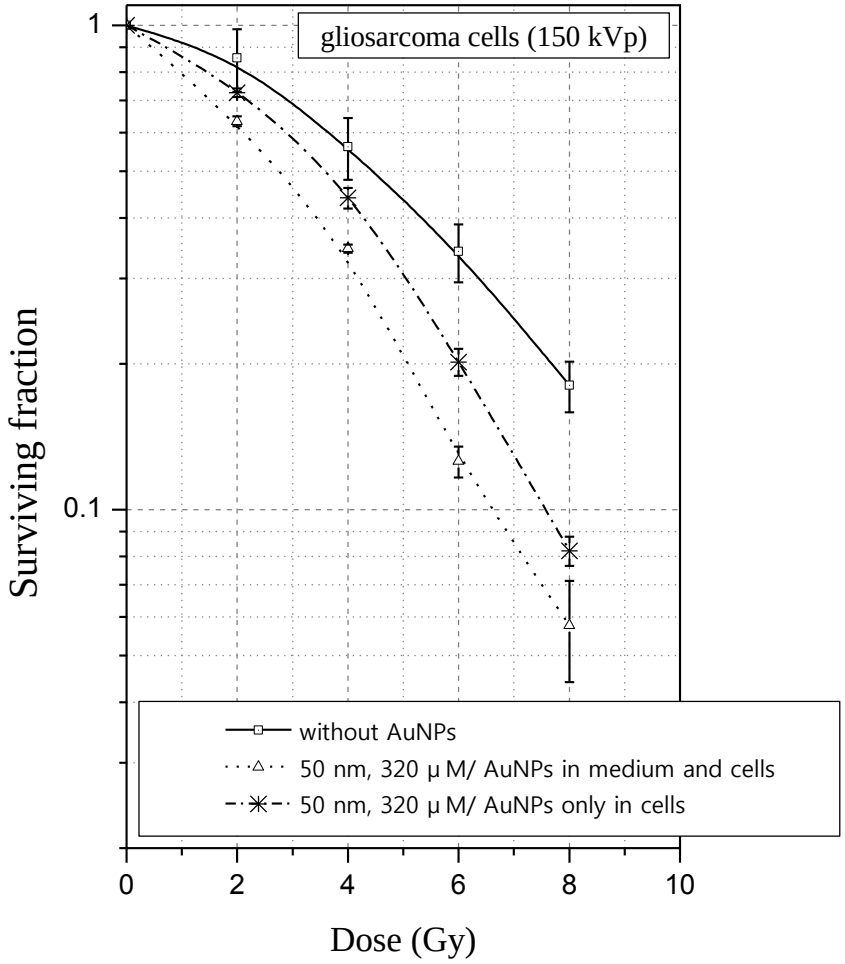

Figure 4.19. Clonogenic surviving fractions of gliosarcoma cells treated with 50 nm (320 μM) AuNPs for 48 h and irradiated with 0, 2, 4, 6, and 8 Gy of 150 kVp x-rays. To measure the dose enhancement effect of cellular localized AuNPs, culture medium containing AuNPs was renewed to fresh medium just before irradiation. The experiment was performed by two different schemes as depicted in Figure 4.20. Error bars indicate on standard error of the mean for three to four independent experiments.

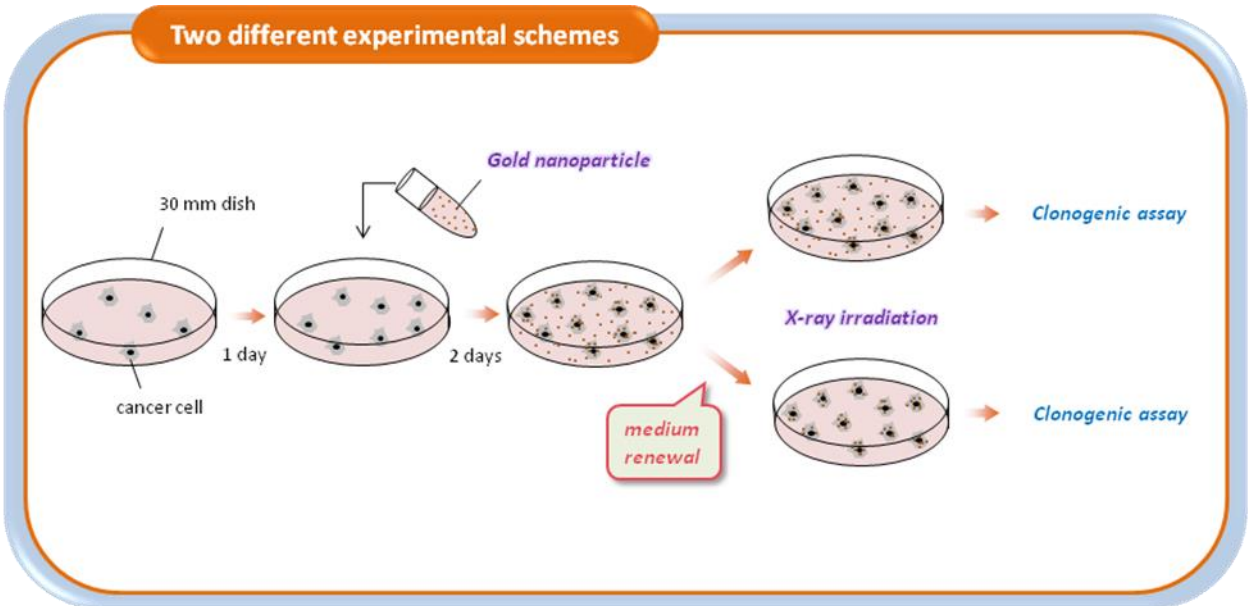

Figure 4.20. Two different experimental schemes for comparing the dose enhancement effect by both extra- and intracellular localized AuNPs or only intracellular localized AuNPs on melanoma and gliosarcoma cells.

4.6 The effect of x-ray energies on cellular dose enh ancement

As shown in Figure 4.21 and 4.22, DEF for melanoma and gliosarcoma cells irradiated with 150 kVp x-rays were higher than those of 450 kVp x-rays. DEF for melanoma cells exposed to 1.9 nm (640 μM) and 50 nm (320 μM) decreased from 1.41 to 1.14, and 2.29 to 1.91 as the x-ray operating energy increased from 150 to 450 kVp, respectively. The corresponding values were 1.49 to 0.98, and 1.70 to 1.36 in gliosarcoma cells.

Figure 4.23 (A) illustrates the ratio of gold mass energy absorption coefficient to soft tissue [14, 49] and (B) represents the calculated energy spectra of the photon beam available from the YXLON model 450-D08, operated at 150 and 450 kVp with a 3 mm-thick aluminum plate fitted over the 5 mm-thick beryllium window [76]. Figure 4.24 and 4.25 show the clonogenic surviving fractions of melanoma and gliosarcoma cells, treated with 1.9 and 50 nm AuNPs for 48 h and irradiated with 0, 2, 4, 6, and 8 Gy of 450 kVp x-rays. The values of α, β, α/β ratio, and DEF from the linear quadratic fitting curves in Figure 4.24 and 4.25 are listed in Table 4.1 and 4.2.

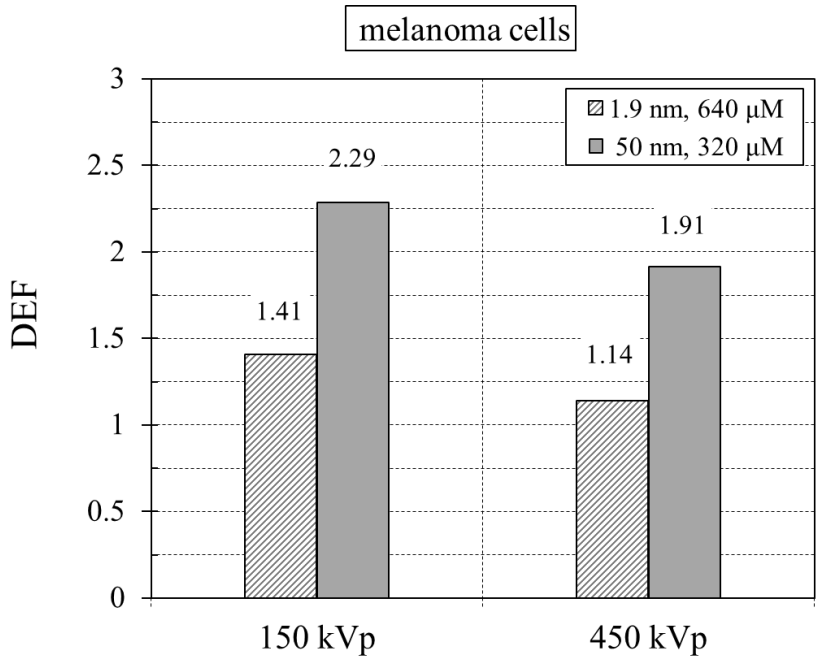

Figure 4.21. DEF for melanoma cells treated with 1.9 and 50 nm AuNPs for 48 h and irradiated with 4 Gy of 150 and 450 kVp x-rays. DEF was determined based on the ratio of the dose required to produce the same surviving fractions as that of the radiation only control cells at a dose of 4 Gy for 150 and 450 kVp, respectively. The values of DEF were taken from Figure 4.10, 4.11, and 4.24. Error bars indicate one standard error of the mean for three to four independent experiments.

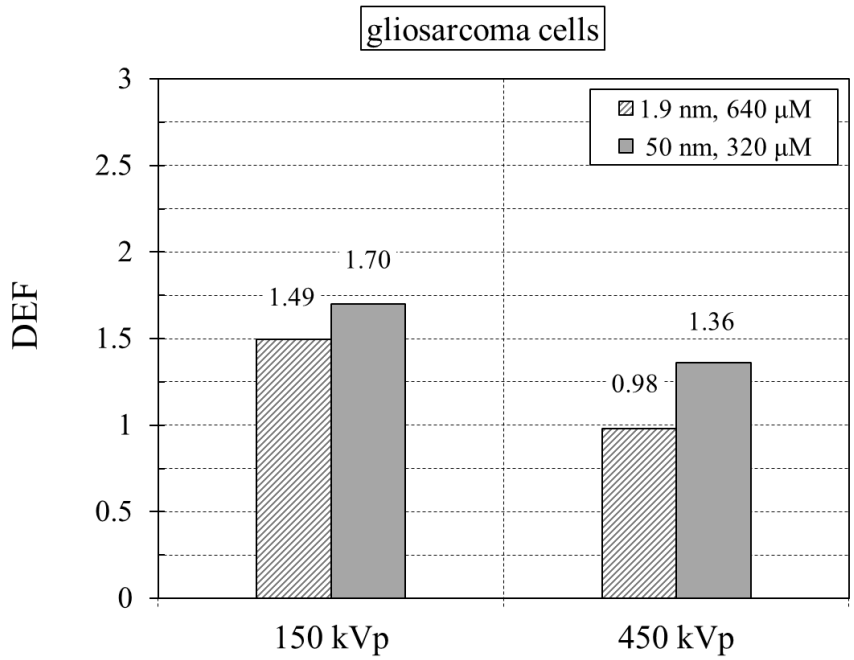

Figure 4.22. DEF for gliosarcoma cells treated with 1.9 and 50 nm AuNPs for 48 h and irradiated with 4 Gy of 150 and 450 kVp x-rays. DEF was determined based on the ratio of the dose required to produce the same surviving fractions as that of the radiation only control cells at a dose of 4 Gy for 150 and 450 kVp, respectively. The values of DEF were taken from Figure 4.12, 4.13, and 4.25. Error bars indicate one standard error of the mean for three to four independent experiments.

(A)

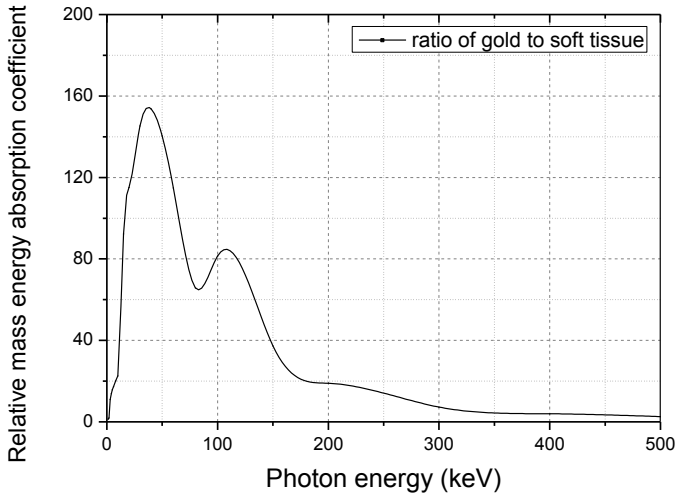

(B)

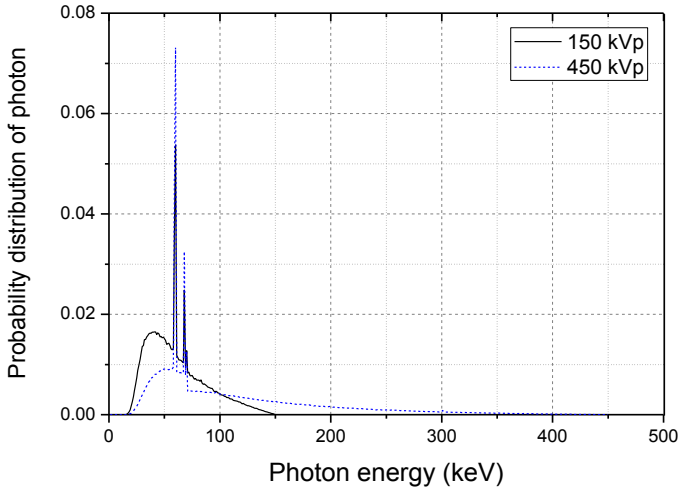

Figure 4.23. (A) Ratio of gold mass energy absorption coefficient to soft tissue [14, 49]. (B) The calculated energy spectra of the photon beam available from the YXLON model 450-D08, operated at 150 and 450 kVp with a 3 mm-thick aluminum plate fitted over the 5 mm-thick beryllium window [76].

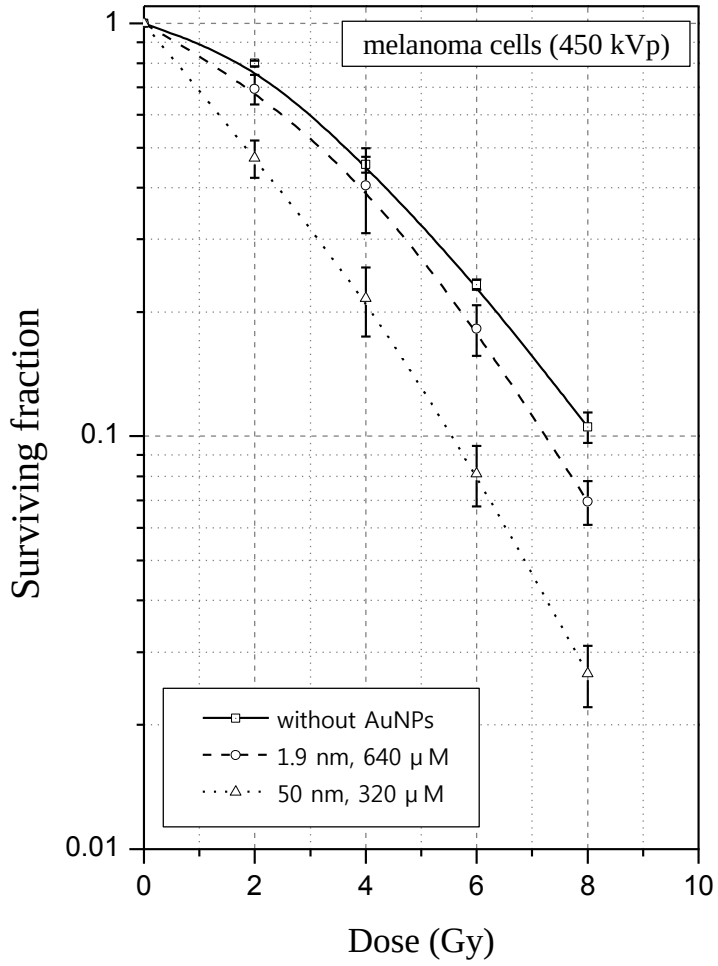

Figure 4.24. Clonogenic surviving fractions of melanoma cells treated with 1.9 nm (640 μM) and 50 nm (320 μM) AuNPs for 48 h and irradiated with 0, 2, 4, 6, and 8 Gy of 450 kVp x-rays. Error bars indicate on standard error of the mean for three to four independent experiments.

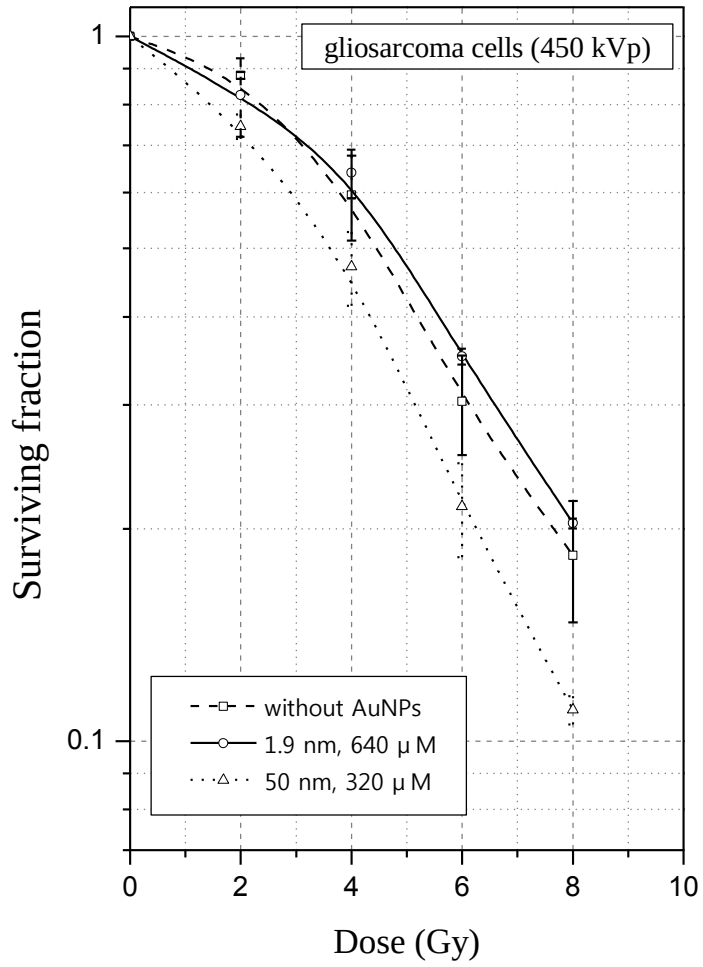

Figure 4.25. Clonogenic surviving fractions of gliosarcoma cells treated with with 1.9 nm (640 μM) and 50 nm (320 μM) AuNPs for 48 h and irradiated with 0, 2, 4, 6, and 8 Gy of 450 kVp x-rays. Error bars indicate on standard error of the mean for three to four independent experiments.

Table 4.1. α, β, α/β, and dose enhancement factor (DEF) of melanoma cells from the linear quadratic fitting curves in Figure 4.10, 4.11, 4.16, 4.17, and 4.24. DEF was determined based on the ratio of the dose required to produce the same surviving fractions as that of the radiation only control cells at a dose of 4 Gy.

x-ray operating voltage	**AuNPs size/concentration**		**Melanoma cells**				
			α (Gy^{-1})	**β (Gy^{-2})**	**R^2**	**α/β**	**DEF**
150 kVp	without AuNPs		0.086 ± 0.012	0.027 ± 0.002	0.999	3.19± 0.47	-
	1.9 nm	320 μM	0.165 ± 0.019	0.021 ± 0.003	0.998	7.86 ± 1.40	1.22
		640 μM	0.193 ± 0.015	0.023 ± 0.002	0.999	8.39 ± 1.03	1.39
	50 nm	160 μM	0.232 ± 0.017	0.023 ± 0.002	0.999	10.09 ± 1.33	1.62
		320 μM	0.396 ± 0.015	0.015 ± 0.002	0.999	26.40 ± 3.82	2.29

(Continued)

x-ray operating voltage	AuNPs size/concentration		Melanoma cells				
			α (Gy^{-1})	**β (Gy^{-2})**	**R^2**	**α/β**	**DEF**
450 kVp	without AuNPs		0.098 ± 0.017	0.023 ± 0.003	0.998	4.26 ± 0.88	-
	1.9 nm	640 μM	0.126 ± 0.005	0.026 ± 0.001	0.999	4.85 ± 0.22	1.14
	50 nm	320 μM	0.325 ± 0.010	0.016 ± 0.001	0.999	20.31 ± 2.00	1.91
150 kVp (only by intracellular localized AuNPs)	1.9 nm	640 μM	0.105 ± 0.012	0.024 ± 0.002	0.999	4.38 ± 0.61	1.06
	50 nm	320 μM	0.188 ± 0.017	0.032 ± 0.002	0.999	5.88 ± 0.70	1.38

Table 4.2. α, β, α/β, and DEF of gliosarcoma cells from the linear quadratic fitting curves in Figure 4.12, 4.13, 4.18, 4.19, and 4.25.

x-ray operating voltage	AuNPs size/concentration		Gliosarcoma cells				
			α (Gy^{-1})	β (Gy^{-2})	R^2	α/β	DEF
150 kVp	without AuNPs		0.062 ± 0.011	0.019 ± 0.002	0.998	3.26 ± 0.67	-
	1.9 nm	320 μM	0.092 ± 0.013	0.016 ± 0.002	0.998	5.75 ± 1.11	1.09
		640 μM	0.172 ± 0.020	0.018 ± 0.003	0.998	9.56 ± 1.95	1.49
	50 nm	160 μM	0.135 ± 0.032	0.017 ± 0.005	0.995	7.94 ± 2.91	1.27
		320 μM	0.205 ± 0.036	0.020 ± 0.005	0.996	10.25 ± 3.21	1.70

(Continued)

x-ray operating voltage	AuNPs size/concentration		Gliosarcoma cells				
			α (Gy^{-1})	**β (Gy^{-2})**	**R^2**	**α/β**	**DEF**
450 kVp	without AuNPs		0.059 ± 0.033	0.020 ± 0.005	0.991	2.95 ± 1.82	-
	1.9 nm	640 μM	0.051 ± 0.020	0.019 ± 0.003	0.996	2.68 ± 1.11	0.98
	50 nm	320 μM	0.121 ± 0.026	0.020 ± 0.004	0.996	6.05 ± 1.70	1.36
150 kVp (only by intracellular localized AuNPs)	1.9 nm	640 μM	0.063 ± 0.012	0.021 ± 0.002	0.998	3.00 ± 0.62	1.02
	50 nm	320 μM	0.108 ± 0.008	0.026 ± 0.001	0.999	4.15 ± 0.37	1.27

4.7 Induction of DNA double strand break in melanoma cells

Figure 4.26 and 4.27 show the percentage of gamma-H2AX positive melanoma cells. The percentage of gamma-H2AX positive cells, treated with 320 μM of 50 nm AuNPs and irradiated with 2 Gy of 150 kVp x-rays, was close to that of cells with no AuNPs and irradiated with 4 Gy. The values were 32 and 34 %, respectively. In Figure 4.11, the clonogenic surviving fraction of melanoma cells, treated with 320 μM of 50 nm AuNPs and irradiated with 2 Gy of 150 kVp x-rays, was also close to that of cells with no AuNPs and irradiated with 4 Gy, 0.43 and 0.47, respectively.

When cells were irradiated with 450 kVp, the percentage of DNA double strand break (DSB) decreased compared to 150 kVp, even cells were exposed to the same concentration and size of AuNPs. DNA DSB induction also decreased when culture medium containing AuNPs was renewed to fresh medium just before irradiation. The result of DNA DSB analysis had the same tendency to the clonogenic surviving fraction. Figure 4.28 and 4.29 show DNA DSB enhancement factor and ratio of SF_{2Gy}, respectively. DNA DSB enhancement factor was determined by comparing gamma-H2AX positive cells (%) at 2 Gy with and without AuNPs for 150 and 450 kVp, respectively. Ratio of SF_{2Gy} was calculated by comparing the clonogenic surviving fraction at 2 Gy (SF_{2Gy}) without and with AuNPs for 150 and 450 kVp, respectively. Ratio of SF_{2Gy} had lower values than DNA DSB enhancement factors, and this difference was supposed to be caused by the repair of a portion of DNA

damages.

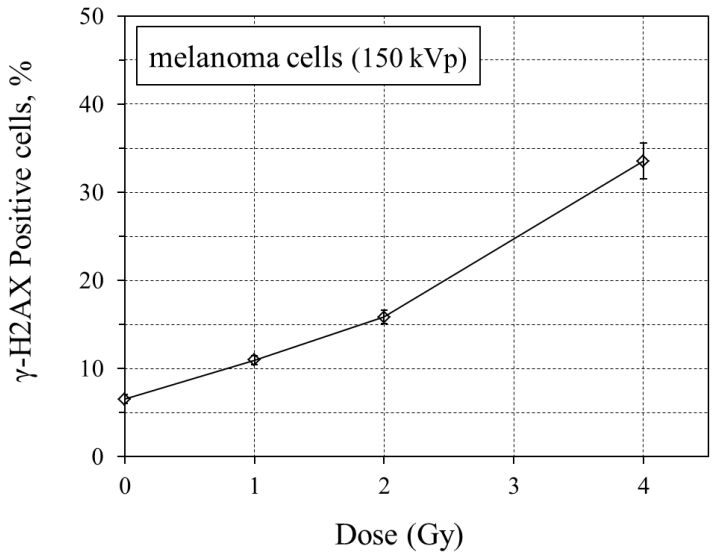

Figure 4.26. DNA DSB analysis by immunostaining for gamma-H2AX. Cells were irradiated with 0, 1, 2, and 4 Gy of 150 kVp x-rays without exposure to AuNPs. Error bars indicate on standard error of the mean for four to six independent experiments.

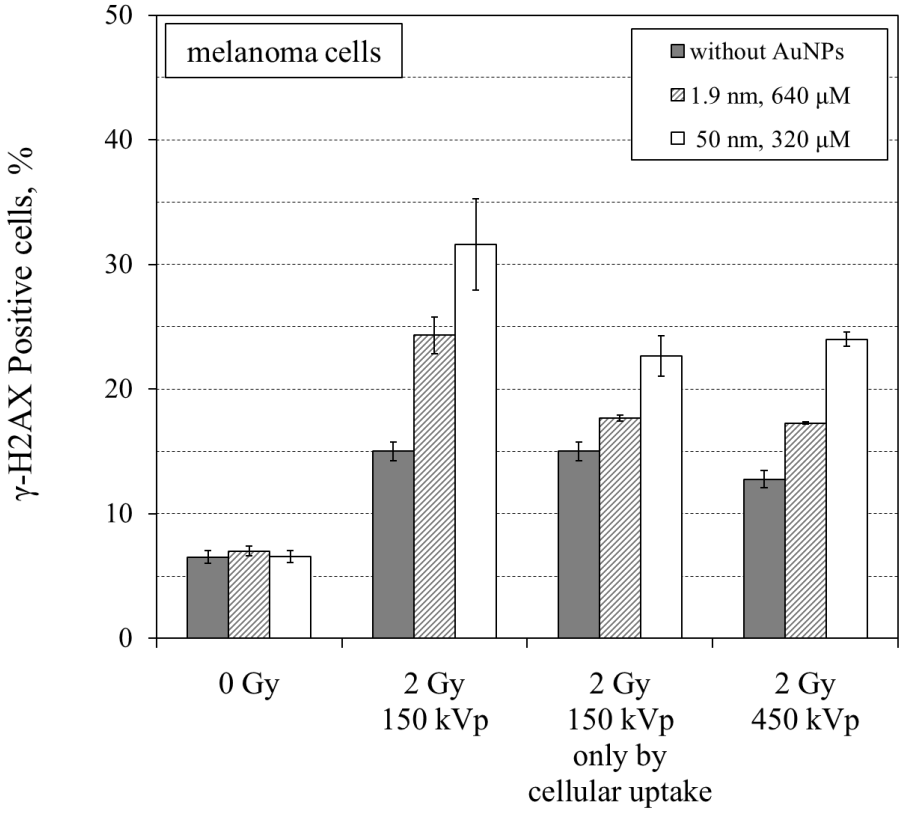

Figure 4.27. DNA DSB analysis by immunostaining for gamma-H2AX. Cells were treated with 1.9 nm (640 μM) and 50 nm (320 μM) AuNPs for 48 h and irradiated with 2 Gy of 150 and 450 kVp x-rays. Error bars indicate on standard error of the mean for four to six independent experiments.

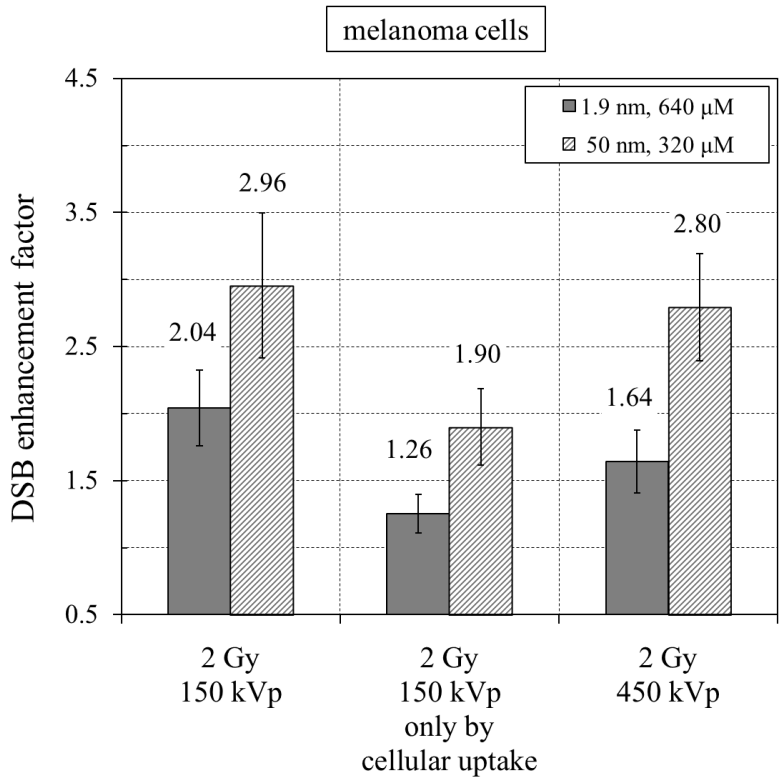

Figure 4.28. DNA DSB enhancement factor, which was determined by comparing gamma-H2AX positive cells (%) at 2 Gy with and without AuNPs for 150 and 450 kVp, respectively. Melanoma cells were treated with 1.9 nm (640 μM) and 50 nm (320 μM) AuNPs for 48 h and irradiated with 2 Gy of 150 and 450 kVp x-rays. Error bars indicate on standard error of the mean for three to six independent experiments.

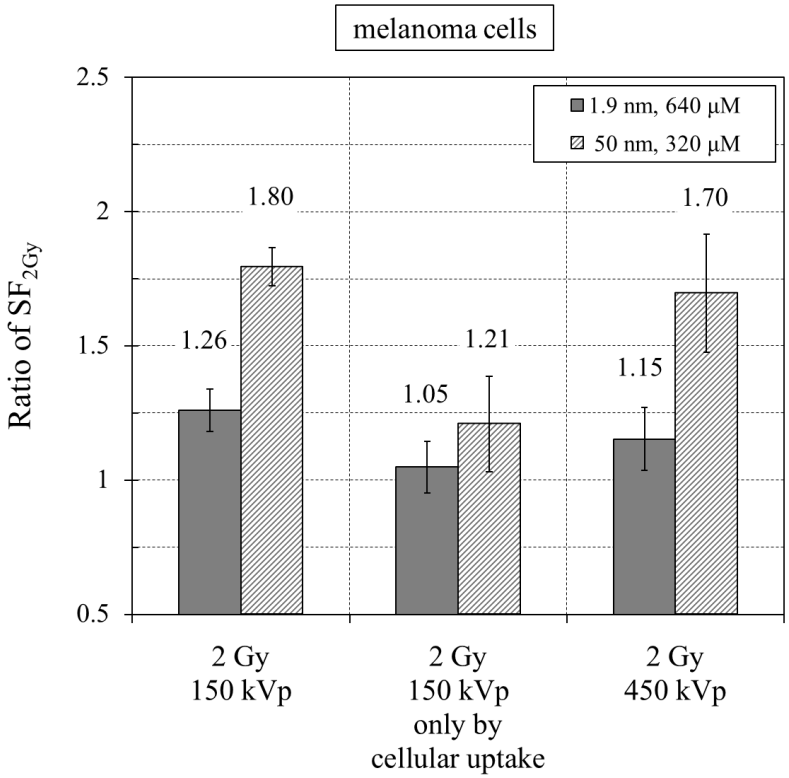

Figure 4.29. Ratio of SF_{2Gy}, which was calculated by comparing the clonogenic surviving fraction at 2 Gy (SF_{2Gy}) without and with AuNPs for 150 and 450 kVp, respectively. Melanoma cells were treated with 1.9 nm (640 μM) and 50 nm (320 μM) AuNPs for 48 h and irradiated with 2 Gy of 150 and 450 kVp x-rays. Error bars indicate on standard error of the mean for three to six independent experiments.

4.8 The effect of AuNPs on cell cycle distribution

As shown in Figure 4.30 and 4.31, G_2/M phase in melanoma and gliosarcoma cells decreased from 11 to 7 % and 20 to 16 % after 48 h exposure to 50 nm AuNPs, respectively ($p<0.05$). On the other hand, cells exposed to 1.9 nm AuNPs for 48 h had no difference in cell cycle distribution as compared with cells grown without AuNPs.

Figure 4.32 and 4.33 show changes of the cell cycle distribution over a 72-h period in melanoma cells after 4 Gy irradiation without and with 320 μM of 50 nm AuNPs. When melanoma cells were irradiated with 4 Gy, 25 % of cells accumulated in G_2/M phase by 12 h, afterward, cells were released from G_2/M arrest and about 17 % by 72 h. Meanwhile, after exposure to both 4 Gy x-ray and 320 μM of 50 nm AuNPs, the percentage of G_2/M phase in melanoma cells increased up to 31 % by 24 h and then decreased to 22 % by 72 h.

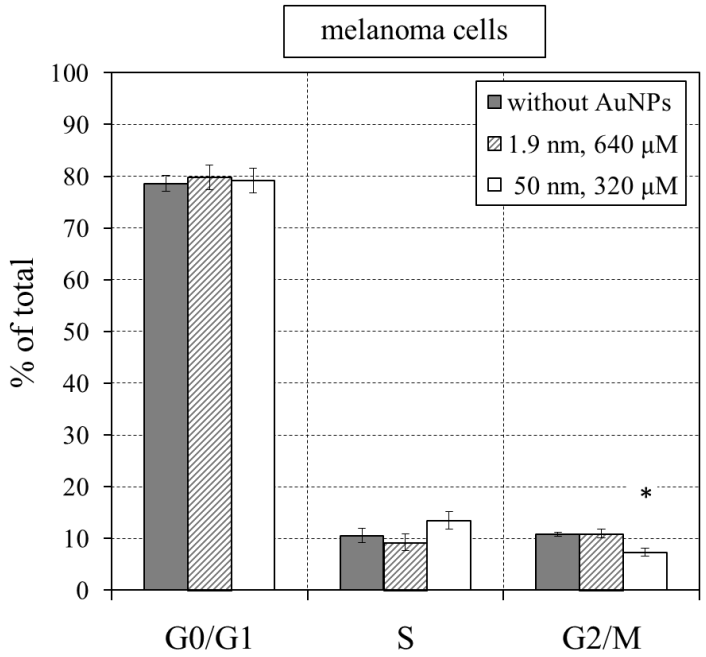

Figure 4.30. Cell cycle analysis of melanoma cells treated with 1.9 nrn (640 μM) and 50 nm (320 μM) AuNPs for 48 h. Error bars indicate on standard error of the mean for four independent experiments. Data sets of significant difference ($p<0.05$) to control are indicated by asterisk.

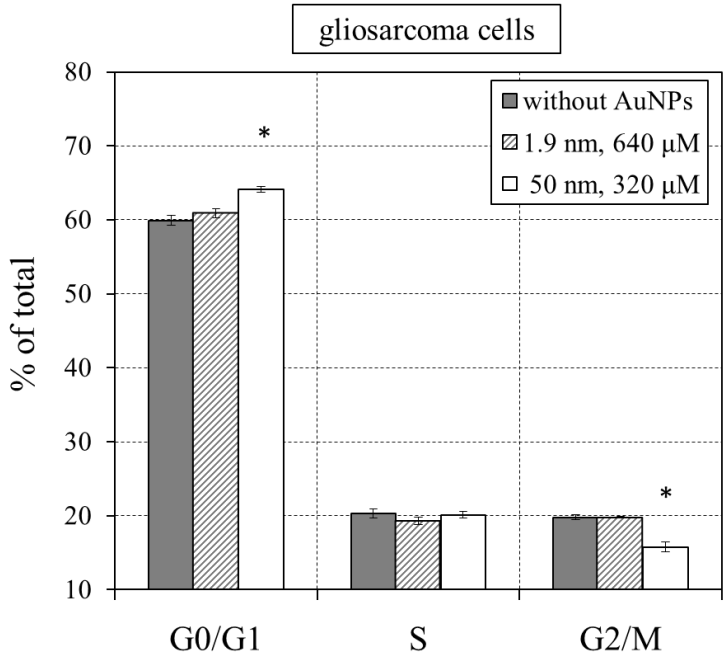

Figure 4.31. Cell cycle analysis of gliosarcoma cells treated with 1.9 nm (640 μM) and 50 nm (320 μM) AuNPs for 48 h. Error bars indicate on standard error of the mean for four independent experiments. Data sets of significant difference ($p<0.05$) to control are indicated by asterisk.

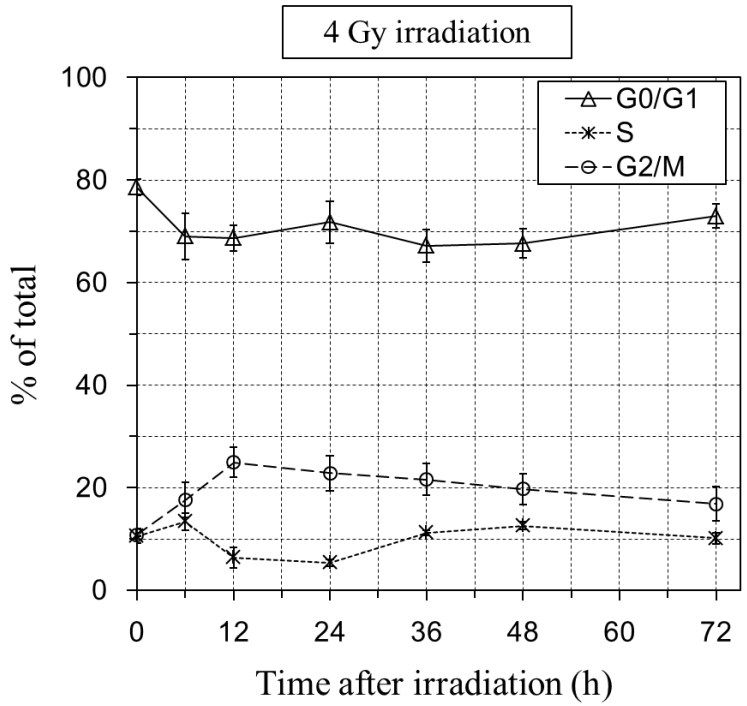

Figure 4.32. Changes of cell cycle distribution in melanoma cells as a function of time after 4 Gy irradiation. Error bars indicate on standard error of the mean for three independent experiments.

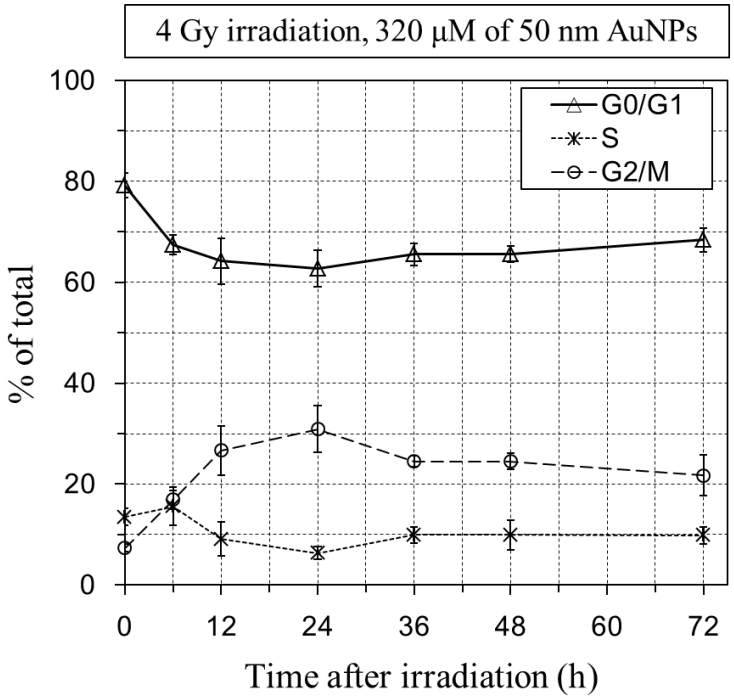

Figure 4.33. Changes of cell cycle distribution in melanoma cells as a function of time after exposure to both 4 Gy x-ray and 320 μM of 50 nm AuNPs. Error bars indicate on standard error of the mean for three independent experiments.

4.9 The effect of 50 nm AuNPs on fibroblast cells

Figure 4.34 and 4.35 show microscopic images of the localization of AuNPs within fibroblast cells after 48 h incubation with 50 nm AuNPs.

Figure 4.36 shows the cytotoxicity of 50 nm AuNPs on fibroblast cells. The result indicated that 50 nm AuNPs had no remarkable effect on the viability of fibroblast cells ($p>0.05$).

Figure 4.37 represents the percentage of gamma-H2AX positive fibroblast cells. When cells were exposed to both 2 Gy of 150 kVp x-rays and 320 μM of 50 nm AuNPs, DNA DSB enhancement factors of fibroblast and melanoma cells were 2.06 and 2.96, respectively.

(A) (B)

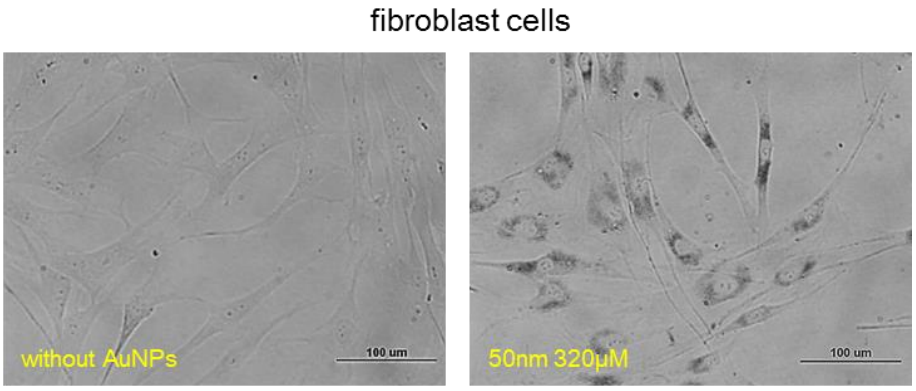

Figure 4.34. Microscopic images of fibroblast cells (A) without AuNPs and (B) with internalized AuNPs after 48 h exposure to 50 nm AuNPs. Microscopic images were observed under a microscope with 40× objective lenses. Bar=100㎛.

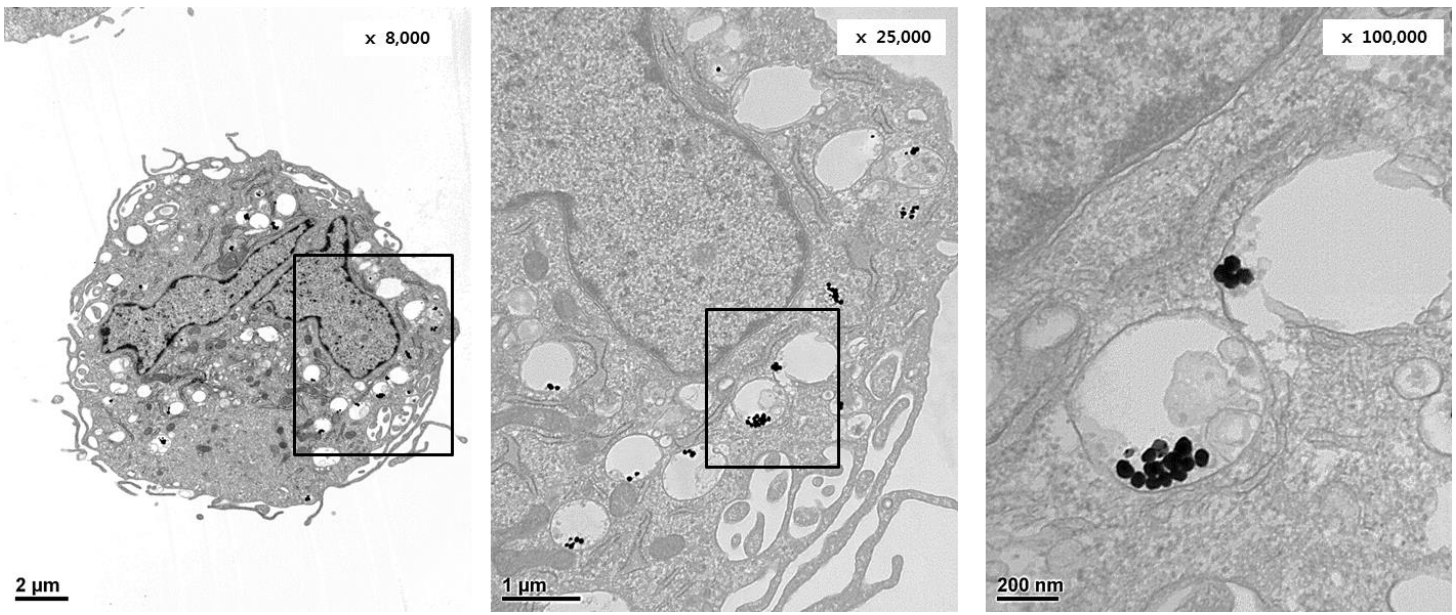

Figure 4.35. TEM images of fibroblast cells after 48 h of incubation in the presence of 50 nm AuNPs. TEM images were observed at a voltage of 80 kV. Scale bars are 2 μm (left), 1 μm (middle), and 200 nm (right), respectively.

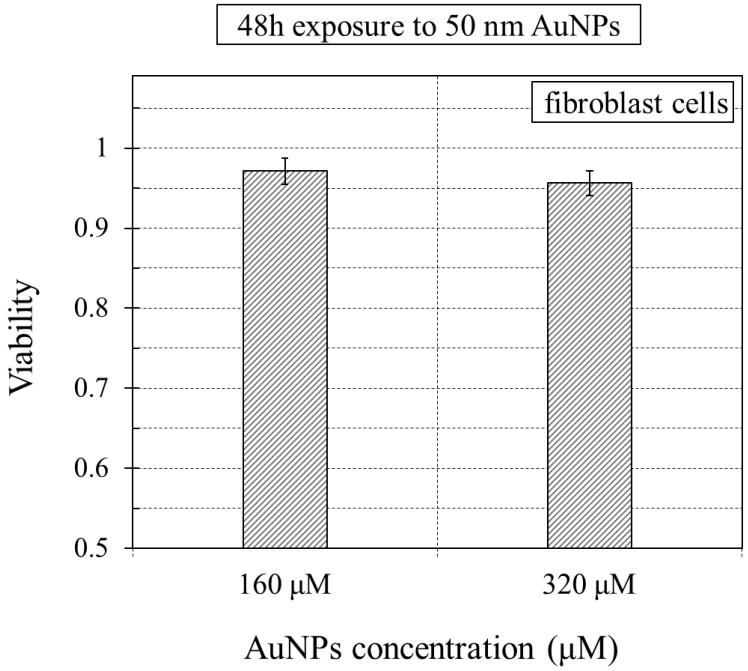

Figure 4.36. The cytotoxicity of 50 nm AuNPs on fibroblast cells. Cells were treated with 50 nm AuNPs for 48 h. Error bars indicate one standard error of the mean for four independent experiments.

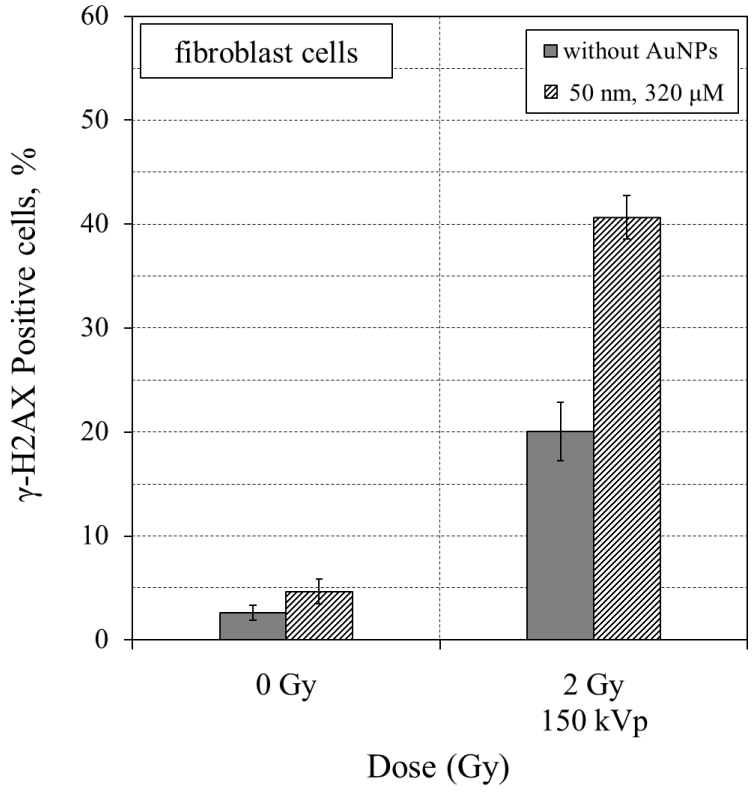

Figure 4.37. DNA DSB analysis by immunostaining for gamma-H2AX. Fibroblast cells were treated with 320 μM of 50 nm AuNPs for 48 h and irradiated with 2 Gy of 150 kVp x-rays. Error bars indicate on standard error of the mean for three independent experiments.

4.10 Depth dose curves and energy spectra of x-ray beams in depth from the skin surface

Figure 4.38 shows depth dose of 150 and 450 kVp x-ray beams in soft tissue. The depth dose decreased to 90 % at about 0.5 and 2.2 cm from the skin surface for 150 and 450 kVp x-ray beams, respectively. 150 and 450 kVp x-ray beams had the maximum dose (D_{max}) at the surface and 3 mm from the surface, respectively.

Figure 4.39 and 4.40 show energy spectra of 150 and 450 kVp x-ray beams in depth from the skin surface, respectively.

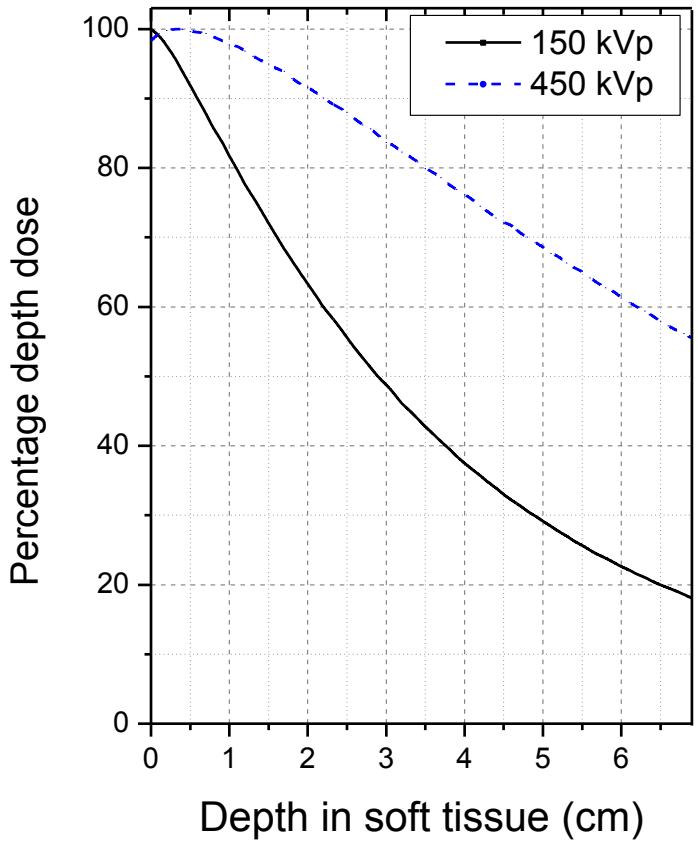

Figure 4.38. Depth dose curves in soft tissue for 150 and 450 kVp x-ray beams. Field size of 3.6 and 10 cm diameter and source to surface distance (SSD) of 20 and 50 cm were used for 150 and 450 kVp x-ray beams, respectively. Energy spectra of the photon beam available from the YXLON model 450-D08 was provided by Lee et al. (2012) [76].

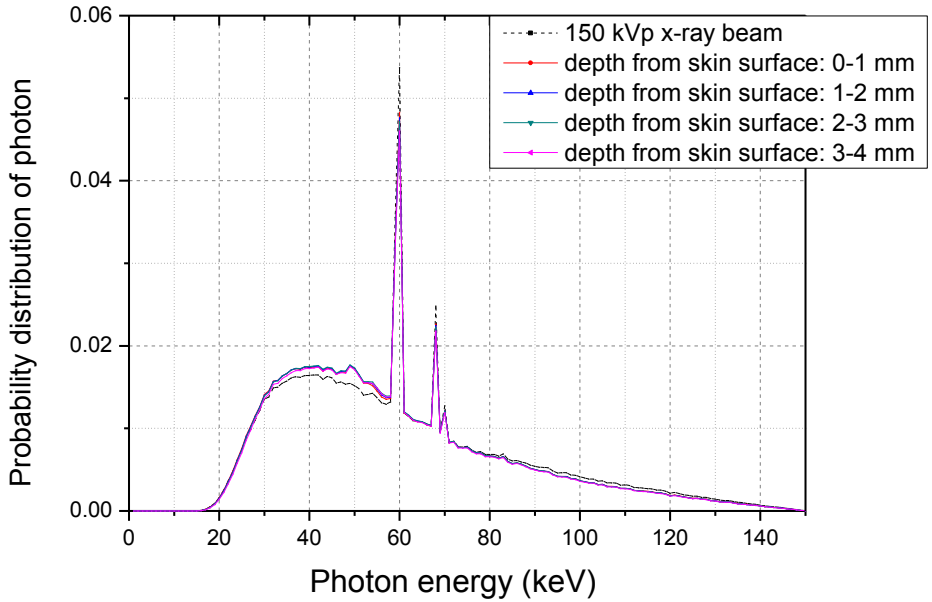

Figure 4.39. Energy spectra of 150 kVp x-ray beams in depth from the skin surface. Field size of 3.6 cm diameter and SSD of 20 cm were used for 150 kVp x-ray beams. Energy spectra of the 150 kVp photon beam available from the YXLON model 450-D08 was provided by Lee et al. (2012) [76].

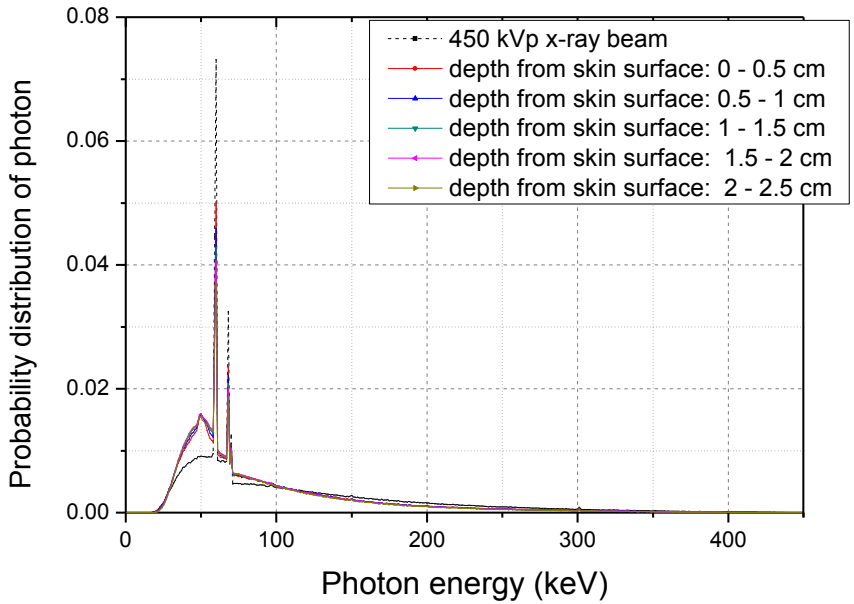

Figure 4.40. Energy spectra of 450 kVp x-ray beams in depth from the skin surface. Field size of 10 cm diameter and SSD of 50 cm were used for 450 kVp x-ray beams. Energy spectra of 450 kVp x-ray beams available from the YXLON model 450-D08 was provided by Lee et al. (2012) [76].

CHAPTER 5

DISCUSSION

We have been conducted the *in vitro* experiments. The clonogenic survival assay was conducted to investigate the dose enhancement effect as functions of AuNP size and concentration, photon energy, and cell-type. Also, the cytotoxiciy assay, the observation of cellular localized AuNPs, DNA DSB analysis, and the cell cycle analysis were performed to support and interpret the main results.

5.1 The considerations for selecting the investigation objects

Skin melanoma and gliosarcoma cells were used in this study. There are three types of skin cancers: basal cell skin cancer, squamous cell skin cancer, and melanoma. Basal and squamous skin cancers (known as non-melanoma) are relatively sensitive to radiation, thereby being commonly treated with radiation therapy [73]. However, melanoma is known as the most difficult to cure and the most radioresistant in all types of skin cancers [63, 64, 77, 78]. Melanoma is rarely treated with radiation therapy due to its high radioresistance [73]. It is known that melanoma causes the majority of skin cancer deaths [69]. Therefore, the increase of melanoma radiosensitivity

should be considered as an important issue for improving the therapeutic efficiency. For that reason, skin melanoma cells were chosen for the main experimental cell line. To apply AuNPs as a dose enhancement agent in skin cancer therapy, it is important to confirm the effect of AuNPs on normal skin cells. Therefore, dermal fibroblast cells were chosen to examine the response of normal skin cells.

Gliosarcoma cell line was also used to compare cell type dependency of the dose enhancement effect, but it was not the only reason of selecting this cell line for the experiment. Microbeam radiation therapy (MRT), a novel preclinical radiosurgery regimen, has been shown to be potentially effective for treatment of brain tumors as well as other types of tumor [79-84]. In conventional external radiation therapy, megavoltage x-rays are generally used for tumors located in the body (except the superficial cancers). However, hundreds of kilovoltage x-rays are utilized in MRT for treating tumors located in the body [79-83], thus we considered that high atomic number nanoparticles can be also applicable as a dose enhancement agent in MRT. Other researchers have been investigated about the application of high atomic number nanoparticles in MRT [85-88]. MRT has been mainly investigated for the treatment of brain tumors, and gliosarcoma has been known as the higly-radioresistant brain tumor [89]. For those reasons, gliosarcoma cell line was additionally selected in this experiment.

1.9 and 50 nm AuNPs were used in this study and the reason for choosing these sizes of AuNPs are as follows. According to the Monte Carlo studies [3, 11, 32, 51], smaller AuNPs deposit more doses to surrounding materials than

larger ones due to their greater surface to volume ratio. The 1.9 nm in diameter was the smallest commercial AuNPs which can be used to the *in vitro* experiments. The 50 nm in diameter of spherical AuNPs has been reported as having the highest efficiency of cellular uptake [90, 91], and the lowest cytotoxicity [7]. Therefore, we considered that it was necessary to compare the dose enhancement effect of 1.9 and 50 nm AuNPs.

The spherical AuNPs have advantages in both experimental and theoretical aspects, as follows. Firstly, cellular uptake depends on the shape of nanoparticles. According to Pan et al. (2007) [7] and Arnida et al. (2010) [91], the spherical shaped nanoparticles with the same aspect ratio (1:1) are taken up to a higher extent compared to rod-shaped nanoparticles with the different aspect ratios (1:3 and 1:5). Secondly, the shape of nanoparticles affects the energy distribution around AuNPs. As the surface to volume ratio is greater, more photoelectric products can escape from AuNPs, leading to the deposition of much more energy to surrounding materials [3]. The sphere has higher surface to volume ratio than other shapes. For these reasons, the spherical AuNPs was selected in this experiment.

5.2 AuNP toxicity and intracellular localization on melan oma and gliosarcoma cells

The dispersion stability of AuNPs can affect significantly on their final performances. As represented in Figure 4.1, no large aggregates were observed in 1.9 and 50 nm AuNPs solution, but small clusters of few nanoparticles were observed. AuNPs were endocyted by the melanoma cells in the form of clusters or single particles. Both single and cluster of AuNPs were observed in cytoplasm (Figure 4.7). According to previous researches [112], aggregation of AuNPs did not indicate unique cytotoxicity and intracellular uptake efficiency.

We investigated the cytotoxicity and cellular uptake efficiency of AuNPs on melanoma and gliosarcoma cells. As shown in Figure 4.8, the cytotoxicity depended on AuNP size and concentration, and cell-type. The viability of gliosarcoma cells was nearly not affected by AuNPs. When gliosarcoma cells were exposed to 640 μM of 1.9 and 50 nm AuNPs for 48 h, the viability reduced to 0.97 and 0.97, respectively, but it was not significant decrease ($p>0.05$). By contrast, the viability of melanoma cells was affected by exposure to both 1.9 and 50 nm AuNPs. The viability of melanoma cells decreased to 0.77 and 0.90 after treating with 640 μM of 1.9 and 50 nm AuNPs ($p<0.05$), respectively. This result represented that 1.9 nm AuNPs had a higher cytotoxicity than 50 nm in melanoma cells. The viability of melanoma cells significantly reduced as the concentration of 1.9 nm AuNPs increased to 640 μM.

As represented in Figure 4.2 - 4.6, AuNPs with diameter 50 nm showed much higher cellular uptake than 1.9 nm in both melanoma and gliosarcoma cells. This result indicated that the smaller AuNPs did not always have advantages in cellular uptake, in agreement with the findings by other researchers [90, 91].

These results indicated that the cytotoxicity of AuNPs would not be directly related to the level of cellular uptake, but it would correlate with AuNPs size and cell-type, which is in agreement with the findings of previous studies [55, 90, 114].

5.3 Dependence of the dose enhancement effect on intracellular localization of AuNPs

Figure 4.9 represents the dose enhancement effect caused by both extra- and intracellular localized AuNPs. Therefore, the additional experiments have been performed to confirm the dose enhancement effect induced only by intracellular localized AuNPs and the result is shown in Figure 4.14 and 4.15. According to these results, the dose enhancement effect of 1.9 nm AuNPs was mostly induced by photoelectric products escaping from extracellular localized AuNPs, due to the low efficiency of cellular uptake, while the dose enhancement effect of 50 nm AuNPs was caused by photoelectric products escaping from both extra- and intracellular localized AuNPs.

According to Monte Carlo studies [3, 11, 32, 51], smaller AuNPs deposit more doses to surrounding materials than larger ones due to their greater surface to volume ratio. But 50 nm AuNPs showed much higher dose enhancement effect than 1.9 nm in the *in vitro* experiments, as shown in Figure 4.14 and 4.15. It indicated that the efficiency of cellular uptake (Figure 4.2 - 4.6) caused a difference of the dose enhancement effect in both melanoma and gliosarcoma cells.

Taken together these findings, it is necessary to consider not only prediction by physical simulation but also the observation of experimentally induced biological outcome, prior to applying AuNPs as a dose enhancement agent.

5.4 Dependence of the dose enhancement effect on incident photon energy

The surviving fractions of cells irradiated with 150 and 450 kVp x-rays were measured to investigate the dependency of the incident photon energy on the dose enhancement effect. Figure 4.23 (A) and (B) show the ratio of gold mass energy absorption coefficient to soft tissue as a function of the incident photon energy [14, 49] and the calculated energy spectra of the photon beam available from the YXLON model 450-D08, operated at 150 and 450 kVp [76]. The application of AuNPs as a dose enhancement agent is premised on the high photoelectric mass absorption coefficient of gold relative to soft tissue [3, 11, 13, 49]. It is important to select photon source energy to maximize the dose enhancement effect. The energy spectra of 150 kVp x-rays is predominantly distributed in the region where the ratio of gold mass energy absorption coefficient to soft tissue has high values, as illustrated in Figure 4.23. Therefore, 150 kVp x-rays were expected to be more effective to enhance radiation dose than 450 kVp and it has been verified by the *in vitro* experiments (Figure 4.21, 4.22, 4.24, and 4.25).

The range of x-ray energy is selected by considering the depth of tumor in radiation treatment. Most useful treatment depth or therapeutic range of radiation is given by the depth of the 90 % depth dose in skin cancer therapy [5]. As represented in Figure 4.38, 90 % depth dose of 150 kVp x-ray beams was exhibited at 5 mm from the skin surface. Thus, AuNPs would be more efficient for T1 ~ T3 stages of melanoma, which are located within about 5

mm depth from the skin surface (classification standard of melanoma stage is represented in Table 2.6) [5, 75, 111]. There is important point to confirm before reaching the conclusion as above. Photon energy spectrum would be changed as photons pass through the soft tissue. Therefore, the change of 150 kVp x-ray energy spectra by passing through the tissue was calculated as a function of depth from the skin surface. As represented in Figure 4.39, energy spectra of 150 kVp x-ray beams at 1 ~ 4 mm depth (depth ranges of T1 ~ T3 stage melanoma) was not remarkably different with that of 150 kVp x-ray beams. According to these results, it is expected that 150 kVp x-ray beams could provide high dose enhancement effect on T1 ~ T3 stages of melanoma by applying 50 nm AuNPs.

5.5 The analysis of α/β ratios from the linear-quadratic cell surviving curves

The experimental cell surviving data were fitted to the linear-quadratic model (Eq 4.2). α and β values relate to the formation of DNA DSB by a single ionizing event and the complementary interaction between two separate ionizing events, respectively. In generally, α and β values are rarely considered individually, but the generic value of α/β ratio is often used for evaluating the efficiency of different kinds of radiation therapy [92-94]. The dual radiation action model of Kellerer and Rossi [92] predicts that, for the linear quadratic model, α value would have much smaller value for low LET radiation, while β value would not have a great difference.

As shown in Table 4.1 and 4.2, α/β ratio significantly increased by adding AuNPs to cells. It means that α parameter considerably increased compared to β parameter. It seems that AuNPs led to cells having high-LET-like exponential decreases in survival. Especially, 320 μM of 50 nm AuNPs resulted in melanoma cells having high-LET-like survival curve with no shoulder as shown in Figure 4.11.

5.6 The effective dose-response in fractionation

It has been well known that fractionated radiation therapy increases tumor cell death by reoxygenation and reassortment of cells into radiosensitive phases and spares normal tissues by repair of sublethal damage and repopulation of normal cells between dose fractions [12]. However, tumor cells proliferate between dose fractions, so that the repopulation of tumor cells lowers the efficacy of treatment by prolonged overall treatment time [95, 96]. Also shorter fractionation may raise concern about the tolerance of normal tissue.

The commonly used fractionation schedule for skin cancer radiation therapy is as follows: 2-4 Gy per fraction per day, 3-4 days per week, and total dose up to 60 Gy [75]. Based on the common fractionation schedule, the assumption was made to compare the dose fraction effect of radiation therapy (RT) alone with the combination of RT and AuNPs in skin cancer treatment: 4 Gy/ fraction (F), 3 days/ week, and total dose 60 Gy.

Figure 5.1 illustrates the effective dose-response curve as a function of dose varies with the number of fractions in which the radiation is delivered. The effective dose-response curve was depicted by using data (taken from Figure 4.11) of melanoma cells irradiated at 150 kVp x-rays without or with 320 μM of 50 nm AuNPs, which was the condition resulting in maximum DEF value (Table 4.1). The effective dose-response relationship is often used for assessing different fractionation regimen. The survival curve for RT is characterized by an initial shoulder, while the survival curve for the

combination of RT and AuNPs has little or no shoulder.

Based on the treatment schedule and the effective dose-response curve, the conventional RT takes about 5 weeks to complete the overall treatment (4 Gy × 15 F), but the overall treatment time is significantly shortened to about 2 weeks by using AuNPs (4 Gy × 6 F). At the equal dose and time fractions, the combination of RT and AuNPs produces the same level of biological effect only after 6 F, while 15 F was required for RT alone.

Although relatively high doses were delivered to tumor by AuNPs, the normal tissue damage would not be more severe because the radiation dose delivered from the equipment does not increase. Also by shortening the overall treatment time, AuNPs can contribute to resolving concern of tumor cell repopulation, which is a main cause of lowering the efficacy of treatment in conventional fractionated radiation therapy. Especially, the overall treatment time is a very important factor for melanoma because it belongs to fast-growing tumors.

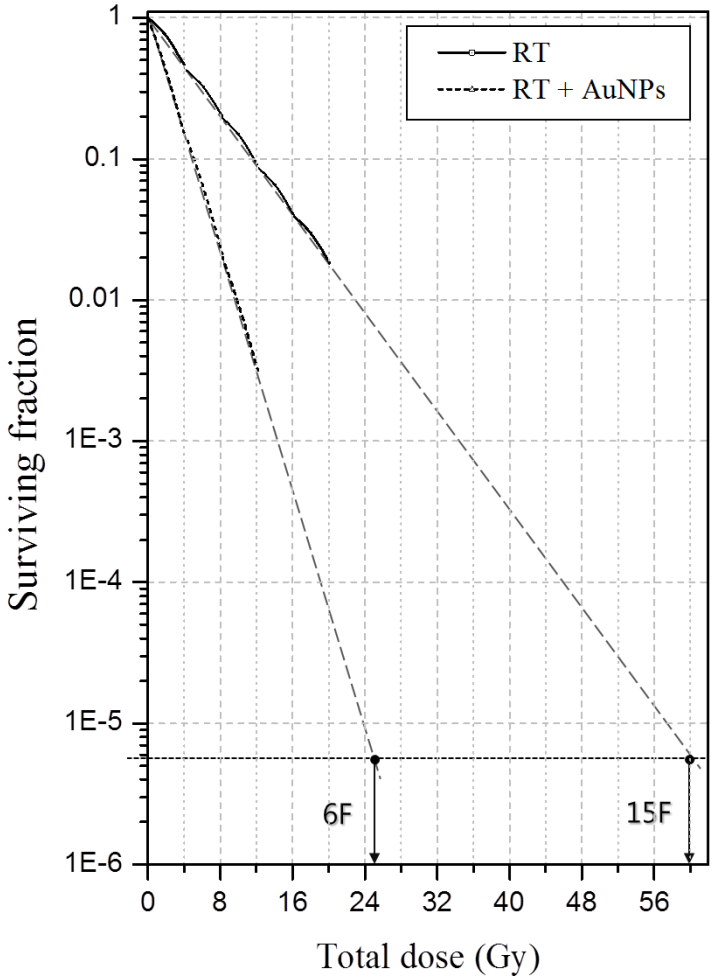

Figure 5.1. Effective dose-response curve of melanoma cells for a fractionation regimen approaches an exponential functions of dose for many doses. The effective dose-response relationship is a straight line from the origin through the point on the single dose survival curve (taken from Figure 4.11), corresponding to the dose fraction (typically 4 Gy). "RT" and "RT + AuNPs" represent the survival curve of cells irradiated with 150 kVp X-rays without or with exposure to 320 μM of 50 nm AuNPs, respectively.

5.7 The mechanism of biological radiation sensitization

The dose enhancement effect calculated by the clonogenic surviving fraction was represented in Figure 4.9, 4.14, 4.15, 4.21, and 4.22. The biological radiation sensitization is mainly caused by the increase of DNA DSB or inhibition of DNA repair [34]. But the decline of the clonogenic surviving fraction cannot be considered as a direct evidence for the increase of radiation induced DNA DSBs, because there also exists other cell death mechanisms such as that which caused by mitochondria or cytoplasm damages [34, 97]. From the comparison of the clonogenic surviving fraction and the level of DNA DSBs (Figure 4.14, 4.15 and 4.27), it can be confirmed that the decrease of clonogenic surviving fraction by AuNPs was directly related to the increase of DNA DSBs. Other *in vitro* studies [33, 98] also have shown a direct correlation between the clonogenic surviving fractions and DNA DSBs.

It has been well known that cells are the most radiosensitive at or close to mitosis (M phase), and G_2 phase is generally as radiosensitive as M phase [92]. When some drugs, such as radiosensitizer, are added to cells, cells accumulate in G_2/M phase of the cell cycle [12, 34]. Thus, the analysis of the cell cycle distribution was needed to confirm whether cells were arrested in G_2/M phase or not after treating with AuNPs. As shown in Figure 4.30 and 4.31, AuNPs did not induce melanoma and gliosarcoma cells to accumulate in G_2/M phase. This result indicated that the change of the cell cycle distribution by AuNPs at

the time of irradiation was not the reason for increasing the dose enhancement effect on cells.

It has been known that the cell cycle arrest is an important response to DNA damage [12]. When DNA is damaged, cells stop progressing and are arrested at checkpoints, such as G_1/S checkpoint, S phase checkpoint and G_2/M checkpoint. G_2/M is the most important checkpoint following radiation damages. Cells are accumulated at G_2/M phase to repair radiation-induced DNA damage before undergoing mitosis.

Therefore, we also investigated the effect of AuNPs on radiation-induced G_2/M arrest. Figure 4.32 and 4.33 show changes of the cell cycle distribution over a 72-h period in melanoma cells after 4 Gy irradiation without and with 320 μM of 50 nm AuNPs. When melanoma cells were irradiated with 4 Gy, 25 % of cells accumulated in G_2/M phase by 12 h, while after exposure to both 4 Gy x-ray and 320 μM of 50 nm AuNPs, the percentage of G_2/M phase in melanoma cells increased up to 31 % by 24 h. Melanoma cells without exposure to AuNPs were released from G_2/M arrest faster than cells with AuNPs. The result indicated that AuNPs led more and longer radiation-induced G_2/M arrest in melanoma cells due to elevated radiation-induced DNA damage.

The analysis of DNA DSB formation and cell cycle distribution gives an obvious evidence for a basic fundamental of this study. In simple terms, it can be suggested that the dose enhancement effect was mainly caused by the increase of DNA DSBs due to the highly localized energy deposition around AuNPs by the release of Auger electrons and photoelectrons.

5.8 The effect of AuNPs on normal fibroblast cells

Based on the results of this experimental study, it has been confirmed that 50 nm AuNPs had more advantages than 1.9 nm as a dose enhancement agent in many aspects. To apply AuNPs as a dose enhancement agent in skin cancer therapy, it is important to confirm the effect of 50 nm AuNPs on normal skin cells. We investigated the cellular uptake and cytotoxicity of AuNPs with human dermal fibroblast cells. As shown in Figure 4.36, 50 nm AuNPs had no remarkable toxicity on fibroblast cells, although AuNPs were localized in the cytoplasm (Figure 4.34 and 4.35). These results also indicated that AuNPs were taken up by fibroblast cells but did not cause severe toxicity.

Dose enhancement effect of 50 nm AuNPs on fibroblast cells has been also investigated in this study as shown in Figure 4.37. The percentage of DNA DSB was significantly increased by exposing cells to 50 nm AuNPs. When cells were exposed to both 2 Gy of 150 kVp x-rays and 320 μM of 50 nm AuNPs, DNA DSB enhancement factors of fibroblast and melanoma cells were 2.06 and 2.96 (Figure 4.37 and 4.27), respectively. Although fibroblast cells show high dose enhancement effect, the magnitude of effect was lower than that of melanoma cells.

5.9 Further *in vivo* investigations

Based on the *in vitro* investigation of this study, it has been confirmed that 50 nm AuNPs had more advantages than 1.9 nm in many aspects, especially the dose enhancement effect. However, it is useless if the size of 50 nm were not suitable for applying *in vivo* skin cancer treatment. Biocompatibility of gold has been already investigated [53-55, 57, 58], and the dose enhancement effect of 50 nm AuNPs on melanoma cells has been also demonstrated in this study. After all, there is an important point to consider for the *in vivo* application of AuNPs. The key point is how AuNPs can be efficiently loaded into tumor volume.

Before reaching the target tissues, nanoparticles undergo a biodistribution step possibly after escaping from the blood circulation through the fenestrations of the endothelial barriers. Biodistribution is dependent on the physicochemical properties of particles, especially size and surface property [99]. According to Ghosh et al. (2008) [100] and Anderson (2009) [101], two approaches have been developed for delivering particles to the target tumors (Figure 5.2): “passive targeting” and “active targeting”. In “passive targeting”, untargeted nanoparticles accumulate in tumors via extravasation through leaky tumor blood vessel. Tumor growth leads the development of tumor vasculature characterized by discontinuous endothelium with large fenestrations between endothelial cells [99, 102]. It allows nanoparticles to accumulate preferentially in tumors. In “active targeting”, nanoparticles are packaged with ligands, such as small molecules, peptides or proteins, which

can bind to the specific receptors of cells. The combination of these two methods would result in an ideal carrier for *in vivo* delivery [100].

These delivery methods can be also applied to load AuNPs within skin cancer [101, 103]. The fenestration sizes of blood vessels in normal tissues and tumors are very important parameters for applying AuNPs in skin cancer [99, 104]. The upper limit of the capillary fenestration size in normal skin is about 6 nm and tumor vasculatures typically have fenestrations between 200 and 780 nm [99, 105]. Based on these data, 1.9 nm AuNPs can accumulate into both skin normal tissues and skin tumor volume, but 50 nm AuNPs can preferentially accumulate into skin tumor volume. And targeted NPs show faster intracellular transport than non-targeted NPs [115], through modifying NPs with specific ligands targeting specific receptors which were over-expressed on the tumor cells [116]. Receptor mediated endocytosis of NPs occurs through interactions between ligands on the surface of NPs and cell membrane receptors [115]. Therefore, the efficiency of melanoma targeting can be maximized by modifying the surface of 50 nm AuNPs with melanoma specific ligands, such as melanocortin type-1 receptor-specific peptide [108, 109].

In case of brain, there are no fenestrations due to the existence of blood-brain barrier (BBB), a barrier between brain tissues and circulating blood. BBB is formed by capillary endothelial cells and serves to protect the central nervous system. However, brain tumor vasculatures typically have fenestrations between 100 to 380 nm [99]. Therefore, both 1.9 and 50 nm AuNPs can be used for loading into brain tumors.

Consequently, it is expected that 50 nm AuNPs would take more advantages than 1.9 nm for the *in vivo* application. The information about targeting methods was based on the data of the previous studies [99-101, 103-105], therefore the *in vivo* experiment should be investigated prior to applying AuNPs in skin cancer radiation treatment.

Although AuNPs have a significant potential for clinical treatment, the biodistribution behavior [118, 119] and toxicological effects should be more investigated before clinical use. There are many reports on *in vitro* toxicity of AuNPs [7, 53-55, 90, 91], however, the published data on *in vivo* experiments are rare and controversial. At present, one can only assume that remarkable toxicity is not revealed during short period exposure to AuNPs. Therefore, long-term *in vivo* studies are needed to confirm the toxicity and mutagenic potential of AuNPs, because AuNPs would remain in the body for many months [118-120].

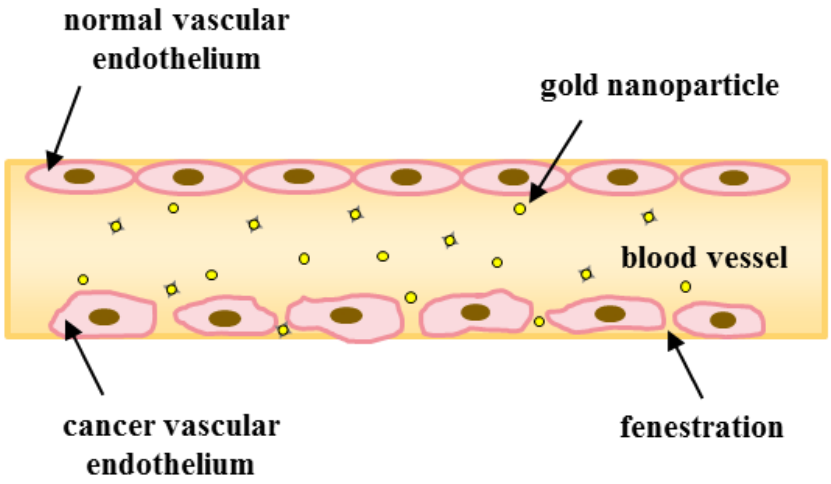

Figure 5.2. Schematic illustration of two approaches for delivering AuNPs via 'active' and 'passive' targeting methods [100, 101].

CHAPTER 6

CONCLUSION

Superficial and orthovoltage x-rays are utilized for skin cancer x-ray therapy because skin cancers are occurred at or within a few centimeters from the surface of skin. But, the 6 to 20 MeV electron beams have been commonly used for skin cancer radiation therapy to exploit the rapid dose-fall off or because kilovoltage x-ray equipment is no longer widely used [70]. The kilovoltage x-ray beams have more advantages than the electron beams for skin cancer therapy in many aspects, such as the easiness to shield eye, the simplicity of dose specification, the ability to minimize field size, etc [70]. Radiation therapy has been generally used to treat basal or squamous skin cancers (non-melanoma), but melanoma has been rarely treated with radiation therapy due to its high radioresistance. Melanoma causes the majority of skin cancer deaths [66, 67, 73]. At this point, the combinational therapy of x-rays and AuNPs can contribute to improving the therapeutic efficiency of melanoma. The ultimate goal of the present *in vitro* study was to confirm the potential of AuNPs as a dose enhancement agent in skin cancer x-ray therapy, especially melanoma treatment.

The principal conclusions of this study are:

1. Cytotoxicity and cellular uptake of AuNPs highly depend on AuNP size, concentration, and cell-type.
2. 50 nm (in diameter) of the spherical AuNP is more efficient for enhancing cell radiosensitivity than 1.9 nm.
3. AuNPs are much more efficient for superficial (150 kVp) than orthovoltage (450 kVp) x-rays as a dose enhancement agent.
4. The optimal combinations of AuNPs and x-rays lead to cells having high-LET-like survival curve with no or little shoulder.
5. The biological radiosensitization is mainly caused by the increase of DNA DSBs due to the highly localized energy deposition around AuNPs by the release of Auger electrons and photoelectrons, not changes in cell cycle distribution.
6. 50 nm AuNPs have no remarkable toxicity on human dermal fibroblast cells and provide lower dose enhancement effect to human dermal fibroblast cells than human skin melanoma cells.

From this study, it has been confirmed that the optimal combinations of AuNP size and concentration, and the range of x-ray energy can significantly enhance the cell radiosensitivity, especially skin melanoma cells. The maximum dose enhancement factor was 2.29 for skin melanoma cells at 320 μM of 50 nm AuNPs with 150 kVp x-ray beams. Therefore, it is expected that T1 to T3 stages of melanoma would be the most efficient target in the combinational therapy of superficial x-rays and 50 nm AuNPs. 50 nm AuNPs are preferably accumulated in melanoma by passive action. And the efficiency

of melanoma targeting should be maximized by modifying the surface of 50 nm AuNPs with melanoma specific ligands, because fibroblast cells also show high dose enhancement effect.

By applying AuNPs to conventional fractionated radiation therapy of melanoma, the major concerns of fractionation regimens are expected to be overcome. Although relatively high doses are deposited to tumor by applying AuNPs, the normal tissue damage would not be more significantly severe because radiation doses delivered from the equipment do not increase. Also by shortening the overall treatment time, AuNPs can contribute to resolving concern about tumor cell repopulation, which is a main cause of lowering the efficacy of the fractionated radiation therapy. In conclusion, the application of 50 nm AuNPs as a dose enhancement agent in superficial x-ray therapy could be a promising melanoma treatment method by delivering a high radiation dose to the tumor volume while sparing normal tissue.

REFERENCES

[1] Intensity Modulated Radiation Therapy Collaborative Working Group. 2001. Intensity-Modulated Radiotherapy: Current status and issues of interest. Int J Radiat Oncol Biol Phys 51(4): 880–914.

[2] Radiologyinfo.org. 2013. Intensity-Modulated Radiation Therapy (IMRT). Accesed at http://www.radiologyinfo.org/en/info.cfm?pg=imrt#part1 on December 16, 2013.

[3] McMahon SJ, Hyland WB, Muir MF, Coulter JA, Jain S, Butterworth KT, Schettino G, Dickson GR, Hounsell AR, O'Sullivan JM, Prise KM, Hirst DG, and Currell FJ. 2011. Biological consequences of nanoscale energy deposition near irradiated heavy atom nanoparticles. Sci Rep 1(18).

[4] Hainfeld JF, Dilmanian FA, Slatkin DN, and Smilowitz HM. 2008. Radiotherapy enhancement with gold nanoparticles. J Pharm Pharmacol 60(8): 977-985.

[5] Khan FM. 2010. The physics of radiation therapy. 4th ed. Philadelphia: Lippincott Williams & Wilkins.

[6] Jain S, Hirst DG, and O'Sullivan JM. 2012. Gold nanoparticles as novel agents for cancer therapy. Br J Radiol 85(1010): 101–113.

[7] Pan Y, Neuss S, Leifert A, Fischler M, Wen F, Simon U, Schmid G, Brandau W, and Jahnen-Dechent W. 2007. Size-dependent cytotoxicity of gold nanoparticles. Small 3(11): 1941–1949.

[8] Knoll GF. 2000. Radiation detection and measurement. 3rd ed. New York: John Wiley & Sons.

[9] Turner JE. 2007. Atoms, Radiation, and Radiation Protection. 3rd, completely revised and enlarged ed. New York: Wiley-VCH.

[10] Evans RD. 1982. The Atomic nucleus. New York: McGraw-Hill.

[11] Lechtman E, Chattopadhyay N, Cai Z, Mashouf S, Reilly R, and Pignol JP. 2011. Implications on clinical scenario of gold nanoparticle radiosensitization in regards to photon energy, nanoparticle size, concentration and location. Phys Med Biol 56(15): 4631–4647.

[12] Hall EJ and Giaccia AJ. 2012. Radiobiology for the Radiologist, 7th ed. Philadelphia: Lippincott Williams & Wilkins.

[13] Rahman WN, Bishara N, Ackerly T, He CF, Jackson P, Wong C, Davidson R, and Geso M. 2009. Enhancement of radiation effects by gold nanoparticles for superficial radiation therapy. Nanomedicine 5(2): 136–142.

[14] Hubbell JH and Seltzer SM. 2004. Tables of X-Ray Mass Attenuation

Coefficients and Mass Energy-Absorption Coefficients. National Institute of Standards and Technology, Gaithersburg, MD. Accessed at http://physics.nist.gov/PhysRefData/XrayMassCoef on January 13, 2014.

[15] Sprawls P. 1993. Interaction of radiation with matter In: Sprawls P. Physical Principles of Medical Imaging. 2nd ed. Gaithersburg. Md: Aspen Publishers.

[16] Kassis AI. 2004. The Amazing World of Auger Electrons. Int J Radiat Biol 80(11-12): 789-803.

[17] Bushberg JT, Seibert JA, Leidholdt EM, and Boone JM. 2002. The essential physics of medical imaging, 2nd ed. Philadelphia: Lippincott Williams & Wilkins.

[18] Kassis AI. 2011. Molecular and cellular radiobiological effects of Auger emitting radionuclides. Radiat Prot Dosimetry 143(2-4): 241-247.

[19] Hainfeld JF, Slatkin DN, Focella TM, and Smilowitz HM. 2006. Gold nanoparticles: a new X-ray contrast agent. Br J Radiol 79(939): 248–253.

[20] Conde J, Doria G, and Baptista P. 2012. Noble metal nanoparticles applications in cancer. Journal of Drug Delivery 751075: 1-12.

[21] Huang X1, Jain PK, El-Sayed IH, and El-Sayed MA. 2007. Gold nanoparticles: Interesting optical properties and recent applications in cancer diagnostics and therapy. Nanomedinicine 2(5): 681-693.

[22] Krishnan S, Diagaradjane P, and Cho SH. 2010. Nanoparticle-mediated thermal therapy: evolving strategies for prostate cancer therapy. Int J Hyperthermia 26(8): 775-789.

[23] Shenoi MM, Shah NB, Griffin RJ, Vercellotti GM, and Bischof JC. 2011. Nanoparticle preconditioning for enhanced thermal therapies in cancer. Nanomedicine 6(3): 545-563.

[24] Chatterjee DK, Fong LS, and Zhang Y. 2008. Nanoparticles in photodynamic therapy: an emerging paradigm. Adv Drug Deliv Rev 60(15): 1627-1637.

[25] Chen W and Zhang J. 2006. Using nanoparticles to enable simultaneous radiation and photodynamic therapies for cancer treatment. J Nanosci Nanotechnol. 6(4): 1159-1166.

[26] Smith L, Kuncic Z, Ostrikov K, and Kumar S. 2012. Nanoparticles in Cancer Imaging and Therapy. Journal of Nanomaterials 891318: 1-7.

[27] Cuenca AG, Jiang H, Hochwald SN, Delano M, Cance WG, and Grobmyer SR. 2006. Emerging implications of nanotechnology on cancer

diagnostics and therapeutics. Cancer 107(3): 459-466.

[28] Rao J. 2008. Shedding light on tumors using nanoparticles. ACS Nano. 2(10): 1984-1986.

[29] Vigderman L and Zubarev ER. 2013. Therapeutic platforms based on gold nanoparticles and their covalent conjugates with drug molecules. Adv Drug Deliv Rev. 65(5): 663-676.

[30] Kim EY, Schulz R, Swantek P, Kunstman K, Malim MH, and Wolinsky SM. 2012. Gold nanoparticle-mediated gene delivery induces widespread changes in the expression of innate immunity genes. Gene Ther. 19(3): 347-353.

[31] Jin S and Ye K. 2007. Nanoparticle-Mediated Drug Delivery and Gene Therapy. Biotechnol Prog. 23(1): 32-41.

[32] Jelveh S and Chithrani DB. 2011. Gold nanostructures as a platform for combinational therapy in future cancer therapeutics. Cancers 3(1): 1081-1110.

[33] Chithrani DB, Jelveh S, Jalali F, van Prooijen M, Allen C, Bristow RG, Hill RP, and Jaffray DA. 2010. Gold Nanoparticles as Radiation Sensitizers in Cancer Therapy. Radiat Res 173(6): 719-728.

[34] Jain S, Coulter JA, Hounsell AR, Butterworth KT, McMahon SJ, Hyland WB, Muir MF, Dickson GR, Prise KM, Currell FJ, O'Sullivan JM, and Hirst DG. 2011. Cell-specific radiosensitization by gold nanoparticles at megavoltage radiation energies. Int J Radiat Oncol Biol Phys 79(2): 531–539.

[35] Butterworth KT, Coulter JA, Jain S, Forker J, McMahon SJ, Schettino G, Prise KM, Currell FJ, and Hirst DG. 2010. Evaluation of cytotoxicity and radiation enhancement using 1.9 nm gold particles: potential application for cancer therapy. Nanotechnology 21(29): 295101.

[36] Liu CJ, Wang CH, Chen ST, Chen HH, Leng WH, Chien CC, Wang CL, Kempson IM, Hwu Y, Lai TC, Hsiao M, Yang CS, Chen YJ, and Margaritondo G. 2010. Enhancement of cell radiation sensitivity by pegylated gold nanoparticles. Phys Med Biol 55(4): 931–945.

[37] Butterworth KT, Wyer JA, Brennan-Fournet M, Latimer CJ, Shah MB, Currell FJ, and Hirst DG. 2008. Variation of strand break yield for plasmid DNA irradiated with high-Z metal nanoparticles. Radiat Res 170(3): 381-387.

[38] Geng F, Song K, Xing JZ, Yuan C, Yan S, Yang Q, Chen J, and Kong B. 2011. Thio-glucose bound gold nanoparticles enhance radio-cytotoxic targeting of ovarian cancer. Nanotechnology 22(28): 285101.

[39] Roa W, Zhang X, Guo L, Shaw A, Hu X, Xiong Y, Gulavita S, Patel S, Sun X, Chen J, Moore R, and Xing JZ. 2009. Gold nanoparticle sensitize radiotherapy of prostate cancer cells by regulation of the cell cycle. Nanotechnology 20(37): 375101.

[40] Kong T, Zeng J, Wang X, Yang X, Yang J, McQuarrie S, McEwan A, Roa W, Chen J, and Xing JZ. 2008. Enhancement of radiation cytotoxicity in breast-cancer cells by localized attachment of gold nanoparticles. Small 4(9): 1537-1543.

[41] Herold DM, Das IJ, Stobbe CC, Iyer RV, and Chapman JD. 2000. Gold microspheres: a selective technique for producing biologically effective dose enhancement. Int J Radiat Biol 76(10): 1357–1364.

[42] Hainfeld JF, Slatkin DN, and Smilowitz HM. 2004. The use of gold nanoparticles to enhance radiotherapy in mice. Phys Med Biol 49(18): N309-315.

[43] Hainfeld JF, Dilmanian FA, Zhong Z, Slatkin DN, Kalef-Ezra JA, and Smilowitz HM. 2010. Gold nanoparticles enhance the radiation therapy of a murine squamous cell carcinoma. Phys Med Biol 55(11): 3045-3059.

[44] Cho SH. 2005. Estimation of tumour dose enhancement due to gold nanoparticles during typical radiation treatments: a preliminary Monte Carlo study. Phys Med Biol 50(15): N13-173.

[45] Jones BL, Krishnan S, and Cho SH. 2010. Estimation of microscopic dose enhancement factor around gold nanoparticles by Monte Carlo calculations. Med Phys 37(7): 3809-3816.

[46] Zhang SX, Gao J, Buchholz TA, Wang Z, Salehpour MR, Drezek RA, and Yu TK. 2009. Quantifying tumor-selective radiation dose enhancements using gold nanoparticles: a monte carlo simulation study. Biomed Microdevices 11(4): 925-933.

[47] Cho SH, Jones BL, and Krishnan S. 2009. The dosimetric feasibility of gold nanoparticle-aided radiation therapy (GNRT) via brachytherapy using low-energy gamma-/x-ray sources. Phys Med Biol 54(16): 4889-4905.

[48] Berbeco RI, Ngwa W, and Makrigiorgos GM. 2011. Localized dose enhancement to tumor blood vessel endothelial cells via megavoltage x-rays and targeted gold nanoparticles: new potential for external beam radiotherapy. Int J Radiat Oncol Biol Phys 81(1): 270-276.

[49] Butterworth KT, McMahon SJ, Currell FJ, and Prise KM. 2012. Physical basis and biological mechanisms of gold nanoparticle radiosensitization. Nanoscale 4(16): 4830-4838.

[50] Seibert JA. 2004. X-Ray Imaging Physics for Nuclear Medicine Technologists. Part 1: Basic Principles of X-Ray Production. J Nucl Med

Technol 32:139–147.

[51] Carter JD, Cheng NN, Qu Y, Suarez GD and Guo T. 2007. Nanoscale energy deposition by x-ray absorbing nanostructures. J Phys Chem B 111(40): 11622-11625.

[52] Hosta-Rigau L, Olmedo I, Arbiol J, Cruz LJ, Kogan MJ, and Albericio F. 2010. Multifunctionalized gold nanoparticles with peptides targeted to gastrin-releasing peptide receptor of a tumor cell line. Bioconjug Chem 21(6): 1070–1078.

[53] Shukla R, Bansal V, Chaudhary M, Basu A, Bhonde RR, and Sastry M. 2005. Biocompatibility of gold nanoparticles and their endocytotic fate inside the cellular compartment: A microscopic overview. Langmuir 21(23): 10644–10654.

[54] Lasagna-Reeves C, Gonzalez-Romero D, Barria MA, Olmedo I, Clos A, Sadagopa Ramanujam VM, Urayama A, Vergara L, Kogan MJ, and Soto C. 2010. Bioaccumulation and toxicity of gold nanoparticles after repeated administration in mice. Biochem Biophys Res Commun 393(4): 649–655.

[55] Connor EE, Mwamuka J, Gole A, Murphy CJ, and Wyatt MD. 2005. Gold nanoparticles are taken up by human cells but do not cause acute cytotoxicity. Small 1(3): 325–327.

[56] Tkachenko AG, Xie H, Liu Y, Coleman D, Ryan J, Glomm WR, Shipton MK, Franzen S, and Feldheim DL. 2004. Cellular trajectories of peptide-modified gold particle complexes: Comparison of nuclear localization signals and peptide transduction domain. Bioconjug Chem 15(3): 482–490.

[57] Elghanian R, Storhoff JJ, Mucic RC, Letsinger RL, and Mirkin CA. 1997. Selective colorimetric detection of polynucleotides based on the distance-dependent optical properties of gold nanoparticles. Science. 277(5329): 1078-1081.

[58] Sokolov K, Follen M, Aaron J, Pavlova I, Malpica A, Lotan R, and Richards-Kortum R. 2003. Real-time vital optical imaging of precancer using anti-epidermal growth factor receptor antibodies conjugated to gold nanoparticles. Cancer Res. 63(9): 1999-2004.

[59] Thurn KT, Brown E, Wu A, Vogt S, Lai B, Maser J, Paunesku T, and Woloschak GE. 2007. Nanoparticles for applications in cellular imaging. Nanoscale Res Lett 2(9): 430-441.

[60] Kogan MJ, Olmedo I, Hosta L, Guerrero AR, Cruz LJ, and Albericio F. 2007. Peptides and metallic nanoparticles for biomedical applications. Nanomedicine (Lond) 2(3): 287-306.

[61] Chang MY, Shiau AL, Chen YH, Chang CJ, Chen HH, and Wu CL. 2008. Increased apoptotic potential and dose-enhancing effect of gold nanoparticles in combination with single-dose clinical electron beams on tumor-bearing mice. Cancer Sci 99(7): 1479-1484.

[62] Ludgate M. 2012. Radiotherapy for malignant skin diseases. Accessed at http://dermnetnz.org/procedures/radiotherapy.html on December 10, 2013.

[63] Quan WDY. 2003. Melanoma and other skin malignancies. In: Skeel RT, ed. Handbook of Cancer Chemotherapy, 6th ed. Philadelphia: Lippincott Williams and Wilkins: 360-377.

[64] Chen KG and Gottesman MM. 2005. How melanoma cells evade chemotherapy: role of transporter-dependent and -independent resistance mechanisms. In: Hearing VJ, Leong SPL, eds. From Melanocytes to Melanoma: The Progression to Malignancy. Totowa, NJ: Humana Press Inc: 93-606.

[65] National Cancer Institute. 2013. SEER Stat Fact Sheets: Melanoma of the Skin. Accessed at http://seer.cancer.gov/statfacts/html/melan.html on February 27, 2014.

[66] National Cancer Institute. 2010. Melanoma and other skin cancers.

Accessed at http://www.cancer.gov/cancertopics/wyntk/skin.pdf on February 27, 2014.

[67] American Cancer Society. 2013. Melanoma skin cancer. Accessed at http://www.cancer.org/acs/groups/cid/documents/webcontent/003120-pdf on February 27, 2014.

[68] Jerant AF, Johnson JT, Sheridan CD, and Caffrey TJ. 2000. Early Detection and Treatment of Skin Cancer. Am Fam Physician. 62(2): 357-368.

[69] American Cancer Society. 2013. *Cancer Facts & Figures 2013*. Atlanta Ga: American Cancer Society.

[70] Amdur RJ, Kalbaugh KJ, Ewald LM, Parsons JT, Mendenhall WM, Bova FJ, and Million RR. 1992. Radiation therapy for skin cancer near the eye: Kilovoltage x-rays versus electrons. Int J Radiat Oncol Biol Phys 23(4): 769-779.

[71] Sinesi C, McNeese MD, Peters LJ, Goepfert H, Kong J, and Mills MD. 1987. Electron beam therapy for eyelid carcinomas. Head Neck Surg 10(1): 31-37.

[72] Locke J, Karimpour S, Young G, Lockett MA, and Perez CA. 2001. Radiotherapy for epithelial skin cancer. Int J Radiat Oncol Biol Phys 51(3):

748-55.

[73] DermNet New Zealand Trust. 2005. Radiotherapy for malignant skin diseases. Accessed at http://dermnetnz.org/procedures/ radiotherapy. html on February 27, 2014.

[74] Cancer research UK. 2013. Radiotherapy for skin cancer. Accessed at http://www.cancerresearchuk.org/cancer-help/type/skin-cancer/treatment/ radiotherapy-for-skin-cancer#page on February 28, 2014.

[75] Wolstenholme V. and Glees J. P. 2006. The role of kilovoltage x-rays in the treatment of skin cancers. European oncological disease. 32-35.

[76] Lee KM, Kim SR, and Kim EH. 2012. Characterization of dose delivery in a hard x-ray irradiation facility. Journal of Nuclear Science and Technology 49(6): 655-661.

[77] Tsao H, Atkins MB, and Sober AJ. 2004. Management of cutaneous melanoma. N Engl J Med 351(10): 998-1012.

[78] Chen KG, Leapman RD, Zhang G, Lai B, Valencia JC, Cardarelli CO, Vieira WD, Hearing VJ, and Gottesman MM. 2009. Influence of melanosome dynamics on melanoma drug sensitivity. J Natl Cancer Inst 101(18): 1259-1271.

[79] Slatkin DN, Spanne P, Dilmanian FA, Gebbers JO, and Laissue JA. 1995. Subacute neuropathological effects on rats of microplanar beams of x-rays from a synchrotron wiggler. Proc Natl Acad Sci USA 92: 8783-8787.

[80] Serduc R, Verant P, Vial JC, Farion R, Rocas L, Remy C, Fadlallah T, Brauer E, Bravin A , Laissue J, Blattmann H, and van der Sanden B. 2006. *In vivo* two-photon microscopy study of short-term effects of microbeam irradiation on normal mouse brain microvasculature. Int J Radiat Oncol Biol Phys 64: 1519-1527.

[81] Serduc R, Christen T, Laissue J, Farion R, Bouchet A, Sanden Bv, Segebarth C, Brauer-Krisch E, Le Duc G, Bravin A, Ramy C, and Barbier EL. 2008. Brain tumor vessel response to synchrotron microbeam radiation therapy: A short term *in vivo* study. Phys Med Biol 53: 3609- 3622.

[82] Dilmanian FA, Qu Y, Liu S, Cool CD, Gilbert J, Hainfeld JF, Kruse CA, Laterra J, Lenihan D, Nawrocky MM, Pappas G, Sze CI, Yuasa T, Zhong N, Zhong Z, et al. 2005. X-ray microbeams: Tumor therapy and central nervous system research. Nuc Instrum Meth Phys Res A 548: 30-37.

[83] Laissue JA, Geiser G, Spanne PO, Dilmanian FA, Gebbers JO, Geiser M, Wu XY, Makar MS, Micca PL, Nawrocky MM, Joel DD, and Slatkin DN. 1998. Neuropathology of ablation of rat gliosarcomas and contiguous brain tissues using a microplanar beam of synchrotron-wigglergenerated-x-rays.

Int J Cancer 78: 654-660.

[84] Kim SR and Kim EH. 2014. Effect of Acidic Environment on the Response of Endothelial Cells to Irradiation: Implication for Microbeam Radiation Therapy. Int J Radiat Biol 90(4): 325-333.

[85] Rahman WN, Wong CJ, Yagi N, Davidson R, and Geso M. 2010. Dosimetry and its enhancement using gold nanoparticles in synchrotron based microbeam and stereotactic radiosurgery. AIP Conference Proceedings 1266(1): 107-110.

[86] Prezado Y, Fois G, Le Duc G, and Bravin A. 2009. Gadolinium dose enhancement studies in microbeam radiation therapy. Med Phys 36(8): 3568-3574.

[87] Dilmanian FA, Morris GM, and Hainfeld JF. 2006. Methods for implementing microbeam radiation therapy. US Patent no. 0176997.

[88] Le Duc G, Regnard P, Bräuer E, Serduc R, Troprès I, Dallery D, Laissue J, and Bravin A. 2007. Use of a Gd-chelate as a dose-enhancement agent for synchrotron microbeam radiation therapy applied to rodent brain tumors. Contrast media & molecular imaging 2: 274-304.

[89] Williams JR, Gridley DS and Slater JM. 2011. Radiobiology of

Radioresistant Glioblastoma. In: Chen CC, editor. Advances in the Biology, Imaging and Therapies for Glioblastoma. ISBN: 978-953-307-284-5, InTech, Available from: http://www.intechopen.com/books/advances-in-the-biology-imaging-and-therapies-for-glioblastoma/radiobiology-of-radioresistant-gliob lastoma.

[90] Chithrani BD, Ghazani AA, and Chan WC. 2006. Determining the size and shape dependence of gold nanoparticle uptake into mammalian Cells. Nano Letters 6(4): 662–668.

[91] Arnida, Malugin A, and Ghandehari H. 2010. Cellular uptake and toxicity of gold nanoparticles in prostate cancer cells: a comparative study of rods and spheres. J Appl Toxicol 30(3): 212-217.

[92] Alpen EL. 1998. Radiation biophysics. 2nd ed. San Diego, California: Academic Press.

[93] Dale R. 2004. Use of the linear-quadratic radiobiological model for quantifying kidney response in targeted radiotherapy. Cancer Biother Radiopharm 19(3): 363-370.

[94] Withers HR, Mason KA, Taylor JM, Kim DK, and Smathers JB. 1993. Dose-survival curves, alpha/beta ratios, RBE values, and equal effect per fraction for neutron irradiation of jejunal crypt cells. Radiat Res 134(3):

295-300.

[95] Kim JJ and Tannock IF. 2005. Repopulation of cancer cells during therapy: an important cause of treatment failure. Nature Reviews Cancer 5(7): 516-525.

[96] Song CW, Park HJ, Griffin RJ, and Levitt SH. 2012. Radiobiology of Stereotactic Radiosurgery and Stereotactic Body Radiation Therapy. In: Levitt SH, Purdy JA, Perez CA, Poortmans P, editors. Technical Basis of Radiation Therapy: Practical Clinical Applications, 5th ed. Berlin Heidelberg: Springer. pp 51-62.

[97] Prise KM, Schettino G, Folkard M, and Held KD. 2005. New insights on cell death from radiation exposure. Lancet Oncol 6(7): 520-528.

[98] Banath JP and Olive PL. 2003. Expression of Phosphorylated Histone H2AX as a Surrogate of Cell Killing by Drugs That Create DNA Double-Strand Breaks. Cancer Res 63: 4347-4350.

[99] Gaumet M, Vargas A, Gurny R, and Delie F. 2008. Nanoparticles for drug delivery: The need for precision in reporting particle size parameters. Eur J Pharm Biopharm 69(1): 1–9.

[100] Ghosh P, Han G, De M, Kim CK, and Rotello VM. 2008. Gold

nanoparticles in delivery applications. Advanced Drug Delivery Reviews 60: 1307–1315.

[101] Anderson MD. 2009. Targeted Nanospheres Find, Penetrate, then Fuel Burning of Melanoma. Accessed at http://www.mdanderson.org/newsroom/news-releases/2009/targeted-nanospheres-find-penetrate-then-fuel-burning-of-melanoma.html on March 12, 2014.

[102] McDonald DM and Baluk P. 2002. Significance of Blood Vessel Leakiness in Cancer. Cancer Res 62(18): 5381-5385.

[103] Lu W, Xiong C, Zhang G, Huang Q, Zhang R, Zhang JZ, and Li C. 2009. Targeted photothermal ablation of murine melanomas with melanocyte-stimulating hormone analog-conjugated hollow gold nanospheres. Clin Cancer Res 15(3): 876-86.

[104] Seymour LW. 1992. Passive tumor targeting of soluble macromolecules and drug conjugates. Crit Rev Ther Drug Carrier Syst 9(2): 135-87.

[105] Sarin H. 2010. Physiologic upper limits of pore size of different blood capillary types and another perspective on the dual pore theory of microvascular permeability. J Angiogenes Res 2: 14.

[106] Zheng Y and Sanche L. 2009. Gold nanoparticles enhance DNA damage induced by anti-cancer drugs and radiation. Radiat Res 172(1): 114-119.

[107] Mesbahi A. 2010. A review on gold nanoparticles radiosensitization effect in radiation therapy of cancer. Reports of Practical Oncology & Radiotherapy 15(6): 176–180.

[108] Rosenkranz AA, Slastnikova TA, Durymanov MO, Sobolev AS. 2013. Malignant Melanoma and Melanocortin 1 Receptor. Biochemistry 78(11): 1228-1237.

[109] Barkey NM, Tafreshi NK, Josan JS, De Silva CR, Sill KN, Hruby VJ, Gillies RJ, Morse DL, Vagner J. 2011. Development of melanoma-targeted polymer micelles by conjugation of a melanocortin 1 receptor (MC1R) specific ligand. J Med Chem 54(23): 8078-8084.

[110] Lee E, Kim do Y, Chung E, Lee EA, Park KS, Son Y. 2014. Transplantation of cyclic stretched fibroblasts accelerates the wound-healing process in streptozotocin-induced diabetic mice. Cell Transplant 23(3): 285-301.

[111] Cancer research UK. 2014. Stages of melanoma. Accessed at http://www.cancerresearchuk.org/cancer-help/type/melanoma/treatment/stag

es - of-melanoma on May 21, 2014.

[112] Albanese A, Chan WC. 2011. Effect of gold nanoparticle aggregation on cell uptake and toxicity. ACS Nano 5(7): 5478-5489.

[113] Cui W, Li J, Zhang Y, Rong H, Lu W, Jiang L. 2012. Effects of aggregation and the surface properties of gold nanoparticles on cytotoxicity and cell growth. Nanomedicine 8(1): 46-53.

[114] Vetten MA, Tlotleng N, Tanner Rascher D, Skepu A, Keter FK, Boodhia K, Koekemoer LA, Andraos C, Tshikhudo R, Gulumian M. 2013. Label-free *in vitro* toxicity and uptake assessment of citrate stabilised gold nanoparticles in three cell lines. Part Fibre Toxicol 10(50).

[115] Chithrani DB. 2010. Intracellular uptake, transport, and processing of gold nanostructures. Mol Membr Biol 27(7): 299-311.

[116] Gao H, Yang Z, Zhang S, Cao S, Shen S, Pang Z, Jiang X. 2013. Ligand modified nanoparticles increases cell uptake, alters endocytosis and elevates glioma distribution and internalization. Sci Rep 3(2534).

[117] Nion S, Briand O, Lestavel S, Torpier G, Nazih F, Delbart C, Fruchart JC, Clavey V. 1997. High-density-lipoprotein subfraction 3 interaction with glycosylphosphatidylinositol-anchored proteins. Biochem J.

328: 415-423.

[118] Khlebtsov N, Dykman L. 2011. Biodistribution and toxicity of engineered gold nanoparticles: a review of *in vitro* and *in vivo* studies. Chem Soc Rev 40(3): 1647-1671.

[119] Li SD, Huang L. 2008. Pharmacokinetics and biodistribution of nanoparticles. Mol Pharm 5(4): 496-504.

[120] Fadeel B, Garcia-Bennett AE. 2010. Better safe than sorry: Understanding the toxicological properties of inorganic nanoparticles manufactured for biomedical applications. Adv Drug Deliv Rev 62(3): 362-374.

국 문 초 록

방사선 치료의 목표는 방사선을 이용하여 효율적으로 암세포를 제거함과 동시에 정상 조직의 손상을 최소화 하는 것이다. 방사선 치료 기술은 끊임없이 발전되어, 현재는 종양의 불규칙한 모양에 맞추어 조사 가능한 세기조절 방사선 치료기가 개발됨에 이르렀다. 하지만, 정상 조직과 암 조직의 엑스선 흡수 특성이 거의 동일하게 나타나기 때문에, 엑스선을 이용한 방사선 치료 시 방사선 치료 장비에 기반하여 암 조직에만 선택적으로 고선량을 전달하는 데에는 한계가 존재한다. 높은 원자번호를 가진 나노 입자를 암 조직에 선택적으로 축적시킴으로써, 피부암과 같이 낮은 에너지 영역의 엑스선을 이용하는 방사선 치료에서 정상 조직을 보호함과 동시에 암 조직에 고선량을 전달하는 방법이 제시 되었다. 고원자번호 나노 입자인 금 나노입자를 방사선 선량 증가제로 사용할 수 있는데, 이는 킬로 볼트의 엑스선 에너지 영역에서 생체 조직에 비해 금이 훨씬 높은 광자 질량 흡수 계수를 가지기 때문이다.

현재 피부암 환자의 발생률이 해마다 증가하고 있는 추세이므로, 금 나노입자가 방사선 선량 증가제로서 피부암 치료 효율 증대에 큰 기여를 할 수 있을 것으로 기대된다. 금 나노입자를 치료 목적으로 적용하기 이전에, 물리적 이론을 기반으로 예측한 선량 증가 효과를 뒷받침할 수 있는 생물학적 실험에 기반한 근거와 금 나노입자에 의한 세포의 방사선 생물학적 반응 특성에 대한 충분한

실험 및 연구가 수행되어야 한다. 본 연구의 궁극적인 목표는 엑스선을 이용한 피부암, 특히 흑색종의 방사선 치료에 방사선 선량 증가제로서 금 나노입자의 활용 가능성을 *in vitro* 실험을 통해 확인하는 것이다.

이번 연구에서는, 피부암 세포의 일종인 흑색종 세포와 뇌종양 세포의 일종인 신경교육종 세포, 그리고 진피 섬유아 세포가 사용되었고, 1.9 nm와 50 nm의 지름을 가지는 구 형태의 금 나노입자가 사용되었다. 방사선 조사는 서울대학교 방사선생명공학 연구실 소재의 YXLON 모델 450-D08 장비를 이용하여 인가전압이 150 kV (표재 영역)와 450 kV (관용전압 영역)인 엑스선을 이용하였다. 금 나노입자의 크기와 농도, 광자의 에너지, 그리고 세포 타입에 따른 방사선 선량 증가 효과를 세포 집락 형성능 분석법을 이용하여 연구하였다. 또한, 세포 독성 실험, 세포 내 금 나노입자 유입 정도 관찰, 디옥시리보핵산의 양 가닥 절단 분석, 그리고 세포 주기 분포 분석을 수행하였으며, MCNP-5 code를 이용하여 150와 450 kVp 엑스선이 조직에 나타내는 심부 선량과 피부 표면으로부터의 깊이에 따른 에너지 스펙트럼의 변화를 확인함으로써 주요 연구 결과를 뒷받침하고 해석하는 기반을 마련하였다.

금 나노입자의 크기와 농도, 엑스선 에너지의 적절한 선택 및 조합을 통해 방사선 민감도를 크게 증가시킬 수 있다는 것이 실험을 통해 확인되었다. 또한, 방사선 선량 증가 효과와 그 정도는 세포 종류에 의해 크게 좌우되며, 이러한 차이는 세포 종류에 따른 세포 내 금 나노입자의 유입 정도에 일정 부분 영향을 받는 것으로 판단된다. 모든 종류의 피부암 중 가장 방사선 저항성이 높다고

알려진 흑색종의 경우 금 나노입자에 의해 방사선 민감도가 크게 증가하는 것으로 확인되었다. 이번 연구에서 나타난 최대 방사선 선량 증가비는 약 2.29로 흑색종 세포가 320 μM 농도의 50 nm 금 나노입자와 150 kV의 엑스선에 노출되었을 때의 결과이다. 흑색종에서 방사선 선량 증가가 최대로 나타나는 조건이 주변 정상 피부 세포에 미치는 영향을 확인하기 위해 진피 섬유아 세포를 대상으로 실험한 결과, 50 nm 금 나노입자는 진피 섬유아 세포에 독성을 거의 나타내지 않으며, 흑생종 세포에 비해 섬유아 세포에 낮은 방사선 선량 증가 효과를 나타냈다. 하지만, 주변 정상 피부 세포에 나타난 방사선 선량 증가 효과는 간과해서는 안되며, 이 결과는 암조직으로의 금 나노입자의 정확한 타겟팅이 매우 중요하다는 것을 보여준다.

금 나노입자를 일반적으로 시행되는 피부암의 방사선 분할 치료에 적용함으로써, 분할 요법에서 나타나는 주요 문제점을 극복하는데 큰 기여를 할 수 있을 것으로 기대된다. 금 나노입자에 의해 비교적 고선량이 암 조직에 흡수되지만, 치료 장비로부터 전달되는 방사선량은 증가되지 않기 때문에 주변 정상 조직의 손상은 크게 증가하지 않는다. 또한, 각 분할 조사 시 암 조직에 흡수되는 선량을 증가시킴으로써 총 치료 기간이 단축되어 결과적으로 방사선 분할 치료의 효율을 낮추는 주요 원인인 치료 기간 중의 암세포 수 증가 문제를 해결하는데 금 나노입자가 큰 기여를 할 수 있다. 결과적으로, 50 nm의 금 나노입자를 표재 엑스선을 이용하는 T1 ~ T3 기 흑색종의 방사선 치료에 방사선 선량 증가제로 사용함으로써 이에 따른 치료 효율 증대를 기대할 수

있다.

주요어: 금 나노입자, 고원자번호 나노입자. 방사선 선량 증가제, 표재 엑스선 치료, 피부암, 흑색종.

학 번: 2010-30253